The HILITE setup for high-intensity-laser experiments with highly charged ions: design and commissioning

Dissertation zur Erlangung des Grades
Dr. rerum naturalium

FRIEDRICH-SCHILLER-UNIVERSITÄT JENA
PHYSIKALISCH-ASTRONOMISCHE FAKULTÄT

eingereicht von Stefan Ringleb,
geboren am 12.10.1983 in Magdeburg

1. Gutachter:
Prof. Dr. rer. nat. habil. Thomas Stöhlker, Friedrich-Schiller-Universität Jena

2. Gutachter:
Prof. Dr. rer. nat. Wilfried Nörtershäuser, Technische Universität Darmstadt

3. Gutachter:
Prof. Richard Thompson MA DPhil., Imperial College London

Datum der Verteidigung: 17. Juni 2020

Zusammenfassung

Die quantitative Untersuchung der Wechselwirkung zwischen atomaren und molekularen Ionen mit Laserstrahlen bei hohen Laserintensitäten und / oder hohen Photonenenergien ist ein bisher weitgehend unbeschrittenes Feld auf dem Gebiet der Laser-Materie-Wechselwirkung. Für die präzise Untersuchung der Effekte werden wohldefinierte Ionenwolken benötigt. Vor allem ihre Zusammensetzung, Lage, Dichte und Form sind von großer Bedeutung, sowie die genaue Kenntnis der Teilchenzahl. In Ionenfallen können gut lokalisierte Ionenwolken erzeugt und charakterisiert werden. Die Ionenfallen sind vielseitige Instrumente, in denen Lage, Form und Dichte durch die Fallenparameter gesteuert und die Teilchenzahlen vor und nach der Laserwechselwirkung bestimmt werden können.

Die vorliegende Arbeit enthält die detaillierte Beschreibung des Aufbaus und der Inbetriebnahme der HILITE (**H**igh-**I**ntensity **L**aser **I**on-**T**rap **E**xperiment) Penningfalle, die dafür entwickelt und konstruiert wurde, wohldefinierte Wolken hochgeladener Ionen für zahlreiche Laserexperimente bereitzustellen. Für die Erzeugung der beschriebenen Ionenwolken sind diverse experimentelle Verfahren nötig. In der Ionenfalle sind Verfahren implementiert für die Produktion hochgeladener Ionen, deren Transport, Auswahl, Einfang, Speicherung, Kühlung, Kompression und Detektion. In der vorliegenden Arbeit wird der Versuchsaufbau detailliert beschrieben. Die für die Präparation der Ionenwolke, ihre Charakterisierung und die zerstörungsfreie Ionenedetektion im Inneren der Falle erforderlichen Komponenten werden charakterisiert. Besonderes Augenmerk wird auf die Zählgrenzen der Detektionselektronik gelegt, da die Kenntnis der genauen Anzahl der gespeicherten Ionen für die geplanten Experimente unerlässlich ist.

Die hochgeladene Ionen werden in einer Elektronenstrahl-Ionenquelle erzeugt, hinsichtlich ihres Masse-zu-Ladungsverhältnisses ausgewählt, abgebremst und in die Falle injiziert, wo sie dynamisch eingefangen und gespeichert werden. Für die Darstellung einer gut definierten Ionenwolke müssen die zunächst hochenergetischen Ionen verlangsamt und auf eine Energie von weniger als 1 meV abgekühlt werden. Diese Arbeit beschreibt die angewandten Methoden der aktiven Rückkopplungskühlung und der Widerstandskühlung und untersucht deren potenzielle Kühleffizienzen.

Abstract

Quantitative studies of the interaction of atomic and molecular ions with laser radiation at high laser intensities and / or high photon energies are a novel area in the field of laser-matter-interaction. They are facilitated by precise knowledge of the properties of the ions as a target for the laser. This refers to the location, composition, density and shape of the ion cloud as a target, as well as to the capability of characterising the ion target before and after the laser interaction. Ion traps are versatile instruments when it comes to localising ions with a defined particle composition, density and state within a specific and small volume in space. They allow in particular the combination of ions in well-defined quantum states with intense photon fields. The present thesis contains the detailed description of the setup and commissioning of the HILITE (**H**igh-**I**ntensity **L**aser **I**on-**T**rap **E**xperiment) Penning trap, which is dedicated to providing a well-defined cloud of highly charged ions for a number of different experiments with intense lasers. Various experimental procedures are necessary to create such an ion cloud, starting with the production of highly charged ions, their transport, selection, capture, storage, cooling, compression and detection. In the present thesis, the experimental setup is described in detail and the components required for ion target preparation, characterisation and non-destructive ion detection inside the trap are characterised. Special attention is paid to the counting limits of the detection electronics, because knowledge of the exact number of stored ions is essential for the planned experiments. Highly charged ions are produced in an electron-beam ion trap (EBIT), selected with respect to their mass-to-charge ratio, decelerated, and injected into the trap, where they are dynamically captured and stored. For the preparation of a well-defined ion cloud, the initially high energetic ions must be slowed and cooled to an energy of less than 1 meV. This thesis describes the applied methods of active-feedback cooling and resistive cooling and examines their potential cooling efficiencies.

Contents

1. Introduction

Experimental studies which investigate the interaction of light with matter have a long history that reaches back to the 19th century. The most important parameters concerning light as used in such early experiments are colour and intensity, with light being regarded as a wave phenomenon. Later experiments largely regarded light as a particle phenomenon, with photons being the quanta of light. This quantised nature of light was first suggested by Max Planck in 1900 as a means of explaining the observed properties of black-body radiation [1]. Based on this concept of light quanta, Albert Einstein provided an explanation of the observed photo-electric effect in which there is a minimum photon energy required to free an electron from matter, irrespective of the light's intensity [2]. The simultaneous absorption of two photons by matter when exposed to strong photon fields was first proposed by Maria Göppert-Mayer in 1931 [3] and was experimentally observed the first time in 1961, following the invention of the 'ruby optical maser' [4], which delivered enough light intensity to drive non-linear optical processes in the visible domain [5]. The invention of free-electron lasers [6] with much higher photon energies on the one hand, and the development of chirped-pulse amplification [7] to achieve high peak intensities on the other hand, have opened up the possibility to ionise even inner-shell electrons in atoms and ions, with ionisation energies reaching many hundreds of eV. The Combination of ions (atomic sytems) in well-defined quantum states as targets for intense photon pulses provides novel research opportunities for the study of light-matter interaction to challenge theory.

At high intensities, the potential of the atomic or ionic nucleus is deformed by the laser field such that the bound electron can overcome the corresponding potential barrier, leading

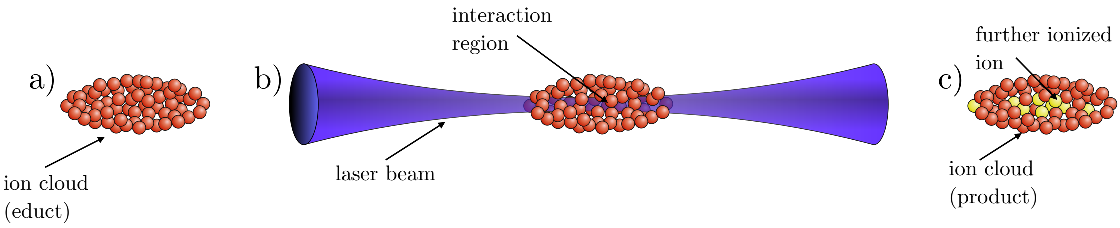

Figure 1.1.: a) First an ion cloud with well-defined density and shape is created inside the Penning trap. b) Then the ions are irradiated by a laser pulse. c) A certain number of higher-charged ions is produced.

to so-called over-the-barrier ionisation [8]. For intensities below this threshold, quantum-mechanical tunnelling is the leading ionisation process. In 2004, Yamakawa et al. [9] have published experimental data on the interaction of ultra-strong laser fields in the relativistic regime, achieving charge states of up to Xe^{20+}. The ionisation probability is highly intensity-dependent and can be determined by ADK-theory [10]. This theory was originally developed for moderate laser intensities and atomic systems, but was found to be applicable in the relativistic regime as well [11]. In the regime of moderate laser intensities, effects like above-threshold ionisation [12], non-sequential double ionisation [13–15], and high-harmonic generation [16] are well-known. In the relativistic intensity regime, the electron is affected significantly by the laser magnetic field, which was assumed to reduce these effects significantly [17]. Nevertheless, the effect of non-sequential double ionisation has been observed for intensities of $1 \times 10^{17}\,\mathrm{W\,cm^{-2}}$ with heavy ions such as xenon ions [18]. During the last decade, and also recently, several theories of ionisation by high-intensity lasers have been published, while on the experimental side, no further experiments with atomic or ionic targets and laser intensities beyond $1 \times 10^{17}\,\mathrm{W\,cm^{-2}}$ have been published. In this thesis, I will introduce the HILITE (**H**igh-**I**ntensity **L**aser **I**on-**T**rap **E**xperiment) Penning trap setup, which opens up new experimental possibilities for the study of laser-ion interaction at extreme laser parameters. The HILITE Penning trap is an ion trap designed in particular to provide a well-defined ion target for laser experiments [19]. Although the ion target is very dilute when compared to bulk matter or some ion beams, and though the comparably long ion-preparation process allows only a limited number of interaction events, the provided ion target consists of selected ion species only, with a well-known ion number density, and at a well-localised position in space. The ion species in particular can be chosen to feature a single active electron, where only the weakest-bound electron is addressed by the laser, while the ionisation probability of the others is in the ppm-regime or below. This facilitates the measurement of ionisation cross sections under very pure conditions. In the regime of high photon energies, Doumy et al. have performed the first K-shell ionisation of neon with an X-ray laser, which was realised by two-photon ionisation. In their work, the relative cross section of $\mathrm{Ne}^{8+}/\mathrm{Ne}^{9+}$ is presented [20]. By use of a well-defined ion target of pure Ne^{8+} in its electronic ground state, the possibility to even measure the absolute cross section of the production of Ne^{9+} from Ne^{8+} arises.

The applied models describing the ionisation dynamics depend on the laser parameters in use at the different laser facilities. On the one hand, there are facilities with high-photon-energy lasers in the XUV [21] or X-ray regime [22], and on the other hand there are high-intensity lasers in the low-photon-energy domain that deliver peak intensities of the order of $1 \times 10^{21}\,\mathrm{W\,cm^{-2}}$ [23–25]. To support studies at such various laser facilities, the HILITE setup is realised in a compact and movable fashion to be set up at different user facilities, and is optimised concerning reliability as well as an easy assembly and movement. A generic ionisation experiment is depicted in figure 1.1. Initially, the ions are produced, stored in the trap, prepared and characterised. Then, the ion target is irradiated by the laser and the reaction products are evaluated. In this thesis I will describe in detail the experimental apparatus and procedures to produce, capture, store, count and prepare the ions, as well as to detect reaction products both destructively and non-destructively. After a brief review of laser-matter interaction in **chapter 2**, I will explain the physics of the Penning trap in detail and will describe how the ions are stored. I will give an overview of fundamental ion manipulation and ion-target preparation techniques in **chapter 3**. I will explain how single-species ion clouds are realised and how the shape and ion density of the cloud can be controlled by proper choice of the trapping parameters. A crucial part in later experiments will be to find the perfect overlap between the ion cloud and the laser focus. In **chapter 4**, I will explain the special circumstances when working with an ion target with well-defined boundaries and their influence on the expected number of ionisation events. The whole experimental setup is explained in **chapter 5**, including the trap electrode design and the devices for efficient ion capture. The in-trap ion detection and ion counting is realised with two distinct tuneable resonant circuits. As the exact knowledge of the number of the ionisation educts and products is necessary to measure absolute cross sections, I will describe destructive and non-destructive ion detection devices that allow precise counting of ions. Based on the design and the experimental parameters, I deduce the prospected minimum number of ions the setup is sensitive to. The ion deceleration and dynamic capture are described in detail in **chapter 6**. The captured ions are detected non-destructively while stored inside the trap, and cooling has been observed. Efficient cooling to low temperatures is the most challenging part of the preparation of a rigid ion cloud. I will estimate the cooling efficiency of resistive cooling inside our Penning trap in **chapter 7**. The special circumstances concerning trap design and initial ion energy will be investigated and a novel approach of wideband active-feedback cooling as pre-cool procedure for resistive cooling will be introduced. I will present the developed cooling electronics and the characterising measurements. By the end of this thesis, we have applied for laser beam time at the FLASH free-electron laser at DESY and have been granted beamtime. The proposal can be found in the appendix of this thesis following section A.3.

2. Laser-Ion Interaction

The development of ultra-intense lasers with pulse durations down to even single cycles with a length of about 2.5 fs as well as the development of lasers with photon energies up to several keV give access to strongly bound electrons in atomic or ionic systems. Lasers with an ultra-high peak intensity beyond $1 \times 10^{20}\,\mathrm{W\,cm^{-2}}$ are typically in the wavelength regime between 750 nm and 1050 nm. High peak powers are achieved by chirped-pulse amplification [7] . There, a short pulse out of an oscillator is stretched, amplified by several amplification stages and compressed again before getting focussed in the target. In the regime of high photon energies beyond 100 eV, free-electron lasers are used. Here, an accelerated electron beam oscillates inside a so-called undulator due to an alternating magnetic field. The lateral acceleration experienced by the electrons causes the emission of UV up to X-ray radiation [21, 26].

2.1. High-intensity laser pulses

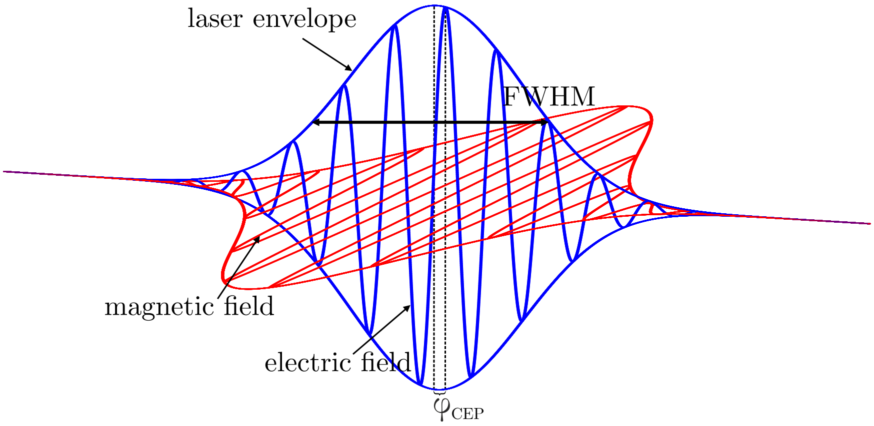

Figure 2.1.: Temporal shape of the electric and magnetic field of a laser pulse. The maximum amplitude is denoted by the pulse envelope.

Lasers with high peak intensities emit pulses with a pulse duration typically between 1 ps down to 20 fs [23–25]. An ultrashort laser pulse is described by its carrier wavelength λ and an envelope with a characteristic FWHM length as depicted in figure 2.1. The characteristics of a pulsed laser and the basic properties are well described in [27] and are summarised below. The laser field is described by its electric field

$$\mathcal{E}(t) = \mathcal{E}_0 \cdot \exp\left(-\left(\frac{t}{\tau}\right)^2\right) \sin\left(\frac{E_\nu}{\hbar} \cdot t + \varphi_{CEP}\right), \tag{2.1}$$

with the amplitude $\mathcal{E}_0$, the pulse duration $\tau = \frac{FWHM}{2\sqrt{\ln 2}}$, the photon energy $E_\nu = \frac{2\pi\hbar c}{\lambda}$, and the carrier envelope phase φ_{CEP}. The peak intensity I is given by

$$I = \frac{c\epsilon_0}{2}\mathcal{E}_0^2, \tag{2.2}$$

with c - vacuum speed of light and ϵ_0 - the vacuum electric field constant. Connected with the laser intensity the *pondermotive potential* U_P is introduced which is a the cycle-averaged kinetic energy of an electron inside an alternating electric field and is given by [28]:

$$U_p = \frac{e^2\hbar^2}{2\epsilon_0 c m_e}\frac{I}{E_\nu^2}. \tag{2.3}$$

From the definition of the ponderomotive energy one can infer that a low photon energy is needed to reach high electron energies.

2.2. Non-linear laser ionisation

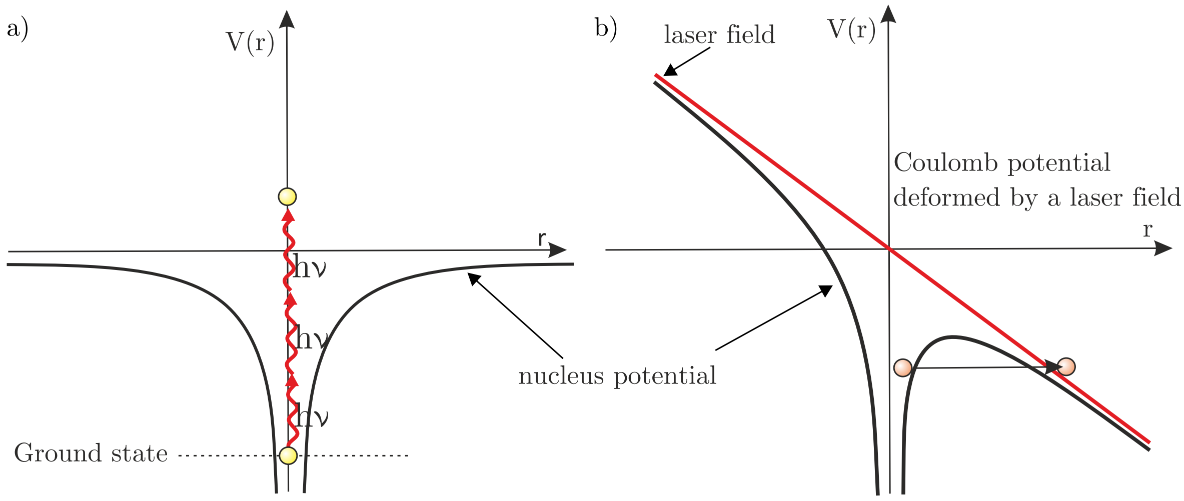

Figure 2.2.: Illustration of the two main laser-ionisation regimes: a) multiphoton ionisation and b) field ionisation.

The electrons in atoms or ions can absorb photons, when they are exposed to photon fields.

Subsequently, the electron is excited or ionised, depending on the binding energy of the electron and the photon energy of the incoming photon. In the first case, the electron absorbs only photons with an energy matching the inner-atomic transition, while in the latter any photon can be absorbed, when its energy is higher than the ionisation energy I_p of the respective electron bound to its parent nucleus. The energy overhead is converted to kinetic energy of the electron - the so-called *kinetic energy release (KER)* [27]. In the case of photon fields with intensities beyond $1 \times 10^{12}\,\mathrm{W\,cm^{-2}}$, there is a certain probability that also electrons are ionised which have a much higher ionisation energy than the energy of the absorbed photons themselves. This effect is called non-linear absorption.

2.2.1. Ionisation regimes

Depending on the laser parameters, non-linear absorption is divided into two different regimes - *multi-photon ionisation* and *field ionisation*. In the case of multi-photon ionisation, the electron gains enough energy to overcome the potential well by the simultaneous absorption of multiple photons which have in sum a higher energy than the ionisation energy (see figure 2.2a). Here, the photon energies are comparable to the magnitude of the ionisation potential and the laser intensities are moderate, while in the case of field ionisation the photon energies are far below the ionisation energy, but the intensities are high (see figure 2.2b). The binding potential of the nucleus is bent by the laser's electric field, so that the electron is able to tunnel through the suppressed barrier to the continuum. To estimate which process is dominant for the present experimental conditions, the so-called Keldysh-parameter γ was introduced [29]:

$$\gamma = \sqrt{\frac{I_p}{2U_p}}. \tag{2.4}$$

For $\gamma \ll 1$ field ionisation is the dominant process while for $\gamma \gg 1$ multi-photon ionisation dominates.

2.2.2. Transition rates

The approach to calculate the transition rate and hence the ionisation probability of a single laser pulse depends on the dominant laser-ionisation process. In both cases, the interaction of a photon field with an electron described by its wavefunction $|\psi(t)\rangle$ bound to a nucleus can be described by the time-dependent Schrödinger equation [27]:

$$i\hbar\frac{\partial}{\partial t}\left|\psi(t)\right\rangle = \left(H_0 + H_{int}(t)\right)\left|\psi(t)\right\rangle . \tag{2.5}$$

The operator describing the undisturbed system of the electron inside the central potential of the nucleus is H_0. The interaction between laser field and the electron is described by the interaction operator H_{int} which can be expressed in the length-gauge [27]:

$$H_{int} = e \cdot \mathcal{E}(t) \cdot r, \tag{2.6}$$

with r the distance between the electron and the nucleus. In the following I will shortly introduce two common approaches to calculate the transition rate, either for the multiphoton and the high-intensity regime.

Pertubative approach

For a laser field with an electric field amplitude which is much lower than the electric field present in the irradiated system ($\gamma \gg 1$), the ground state of the ion can be assumed to be constant during the laser-ion interaction. In this case, pertubative methods can be applied to calculate the transition rate from an initial state $|\psi_i\rangle$ to the final state $|\psi_f\rangle$. In the case of excitation from one discrete eigenstate of H_0 to another, the transition rate for an ionisation process involving n photons is given by [27]

$$W_{fi}^{(n)} = \frac{2\pi}{\hbar}(2\pi\alpha\hbar)^n I^n |M(n)_{fi}|^2 \rho_f(E_f). \tag{2.7}$$

Here, α is the fine-structure constant. The factor $\rho_f(E_f)$ considers the line profile of the final energy level and $M(n)_{fi}$ is the transition matrix element for the n-photon transition. In the case of ionisation, the final state $|\psi_f\rangle$ is continuous. To obtain the ionisation rate W_{ion}, an integration over all possible final states is performed. All prefactors and system properties are combined into the ionisation cross section σ_n for the absorption of n photons:

$$W_{ion} = \sigma_n I^n. \tag{2.8}$$

Barrier suppression regime

In the case of tunnel ionisation, the electric field of the laser is of the order of the magnitude of the electric field of the nucleus at the position of the electron. In this approach, only one active electron is assumed. The electron with its quantum numbers (n*,l,m) is bound by the nucleus with nuclear charge Z. The quantum number n* is the effective principal quantum number following

$$n^* = \sqrt{\frac{Z^2}{2I_p}}, \tag{2.9}$$

taking the shielding of the other electons into account. Assuming now the superposition of the electric field of the laser $\mathcal{E}$ and the electric field of the parent nucleus, for electric field strengths above the critical value of

$$\mathcal{E}_{OBI} = \frac{I_p^2}{4Z} \tag{2.10}$$

the so-called *over-the-barrier ionisation* occurs [8]. Here, the core potential is suppressed so much, that the electron is not bound any more to the nucleus and is emitted to the continuum. For electric fields below $\mathcal{E}_{OBI}$ there is still a certain probability, that the electron tunnels trough the suppressed barrier. In the case of low-frequency lasers (NIR regime) the applied electric field $\mathcal{E}$ can be assumed to be static, as long as the laser period is much longer than the period of the electron surrounding the nucleus (quasi-static approximation). For hydrogen-like ions the ionisation rate is given by [27]:

$$W_{DC} \approx \frac{4Z^5}{\mathcal{E}} \exp\left(-\frac{2}{3}\frac{Z^3}{\mathcal{E}}\right). \tag{2.11}$$

For arbitrary ions with an ionisation energy I_p, the common method to calculate the ionisation rate is the so-called *ADK-method* [10]. Assuming a linearly polarised laser, the ionisation rate is given by

$$\begin{aligned} W_{ADK}(\mathcal{E}_0) =& c_{ADK}^2 A(l,m) \sqrt{\frac{3\mathcal{E}_0\kappa}{2\pi}} \left(\frac{2\kappa^3}{\mathcal{E}_0}\right)^{2Z_c/\kappa-|m|-1} \exp\left(-\frac{2\kappa^3}{3\mathcal{E}_0}\right) \\ \text{with} \quad & \kappa = \sqrt{2I_p} \\ \text{and} \quad & A(l,m) = \frac{2l+1}{2^{|m|}|m|!}\frac{(l+|m|)!}{(l-|m|)!} \end{aligned} \tag{2.12}$$

In the limit of $l \ll n^*$ The parameter c_{ADK} is given by:

$$c_{ADK} = \left(\frac{2e}{n^*}\right)^{n*} \frac{1}{\sqrt{2\pi n^*}}. \tag{2.13}$$

Highly charged ions in the ground state with a single electrons in the 1s or 2s state (l=0) fulfill this relation typically. Assuming now a laser pulse described by equation 2.1, the transition probability in each time interval [t,t+Δt] is $W_{ADK} \cdot \Delta t$. The probability $P(t)$ that the electron is emitted in the very interval [t,t+Δt] is then

$$P(t) = W_{ADK}(\mathcal{E}(t)) \cdot \Delta t \cdot \left(1 - \int_0^t W_{ADK}(\mathcal{E}(t'))\mathrm{d}t'\right). \tag{2.14}$$

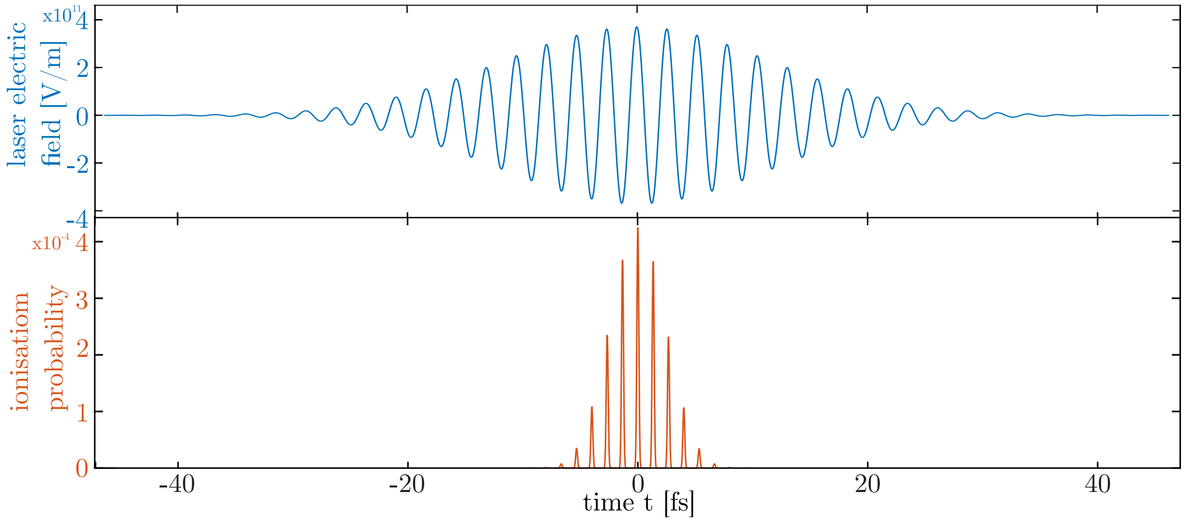

Figure 2.3.: Exemplary electric field strength of a laser pulse with a FWHM of 40 fs. The time resolved ionisation probability is plotted in the lower graph. The ionisation rate is highest close to the maximum electric fields.

Figure 2.3 shows the time-dependent electric field of a laser pulse and the corresponding probability for the electron to be ionised at a certain time. The integral over the whole ionisation density is the probability of the electron to be ionised by a single laser shot. The ionisation probability is highly dependent on the laser's electric-field strength and appears most likely close to the electric-field maxima.

3. Penning traps

3.1. The cylindrical Penning trap

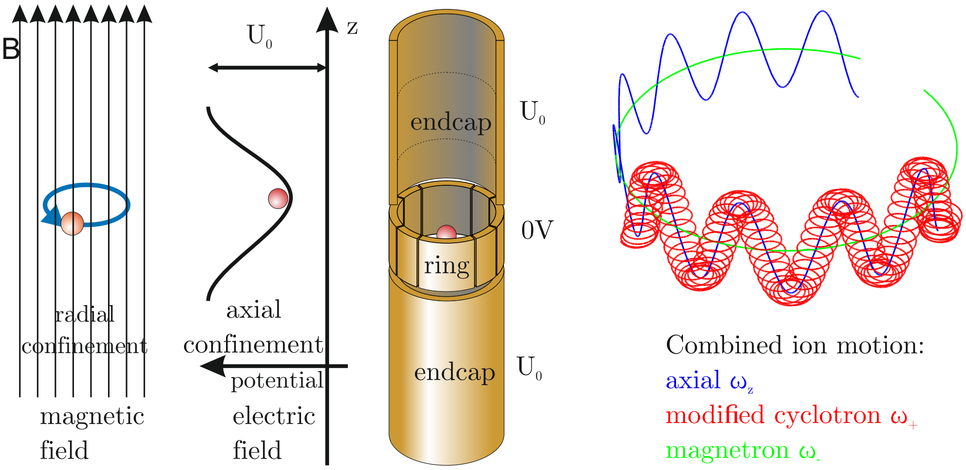

Figure 3.1.: Illustration of the concept of the cylindrical Penning trap. A static magnetic field is superimposed by a static electric field provided by a set of cylindrical electrodes. A single ion performs a superposition of three individual motions.

A Penning trap is used to store charged particles at a defined position. To this end, a static magnetic field is superimposed with a static quadrupolar electric field, where the former ensures radial confinement and the latter axial confinement. Hence, the Penning trap is a device which enables the storage of ions of different charge-to-mass ratios at the same time [30].

The magnetic field is typically of the order of some tesla which is either provided by a superconducting magnet [31] or by a set of permanent magnets in a specific configuration [32]. The electric field is maintained by a set of at least three electrodes, the so-called *ring* and *endcap electrodes*. Figure 3.1 shows a set of electrodes in the *cylindrical open-endcap* design with *mechanical compensation* of trap anharmonicities. Here, the quadrupolar electric field is assured by proper choice of trap diameter ρ_0 and endcap separation distance z_0. Detailed explanations can be found in [33]. The segmented structure of the ring electrode is used to detect and manipulate the stored ions and does not affect the storage conditions.

In this thesis I describe exclusively the cylindrical case with mechanical compensation, as we use this design with the presented ion trap.

3.2. The motion of an ion in a Penning trap

In this section I will point out how experimental parameters influence the ion motions in detail. As the HILITE Penning trap is a cylindrical trap, I express the fields and potentials in cylindrical coordinates (ρ, ϕ, z).

In an ideal Penning trap the ions are confined by a homogeneous magnetic field with the magnetic flux density B_0 and a quadrupolar electric potential. Ideally, the magnetic field has only a z-component, so that:

$$\vec{\mathbf{B}} = (0, 0, B_0). \tag{3.1}$$

Between the ring electrode and the endcap electrodes a voltage U_0 creates the electric potential which is constant along the ϕ-axis. Near the trap centre, the potential can be expanded in terms of the Legendre polynomials P_k as follows [34]:

$$\begin{aligned} U =& \frac{1}{2} U_0 \sum_{k=0,even}^{\infty} c_k \left(\frac{r}{d}\right)^k P_k(\cos\theta) \\ &\text{with} \quad \cos(\theta) = \frac{z}{r} \\ &\text{and} \quad r^2 = \rho^2 + z^2, \end{aligned} \tag{3.2}$$

where r is the distance to the trap center, θ is the angle between the vector pointing from the trap centre to the ion and the z-axis, and d denotes the so-called *characteristic trap dimension* [35]:

$$d^2 = \frac{1}{2} z_0^2 + \frac{1}{4} \rho_0^2. \tag{3.3}$$

The odd coefficients c_k are zero due to the symmetry across the z=0 plane and the c_0 coefficient is only an offset of the potential and can be ignored. For an ideal Penning trap c_2 is the only non-zero coefficient and describes a harmonic electrical potential and hence a harmonic motion of a charged particle with mass m and charge q along the z-axis with the frequency

$$\omega_z = \sqrt{\frac{q}{m}\frac{U_0 c_2}{d^2}} \tag{3.4}$$

which is called the *axial frequency* [30]. The higher-order trap parameters c_4,c_6, and so forth are the so-called *anharmonicity parameters* causing energy-dependent shifts of the axial frequency. Details can be found in [33].

In the radial direction the ions are confined by the magnetic field. A pure magnetic field in absence of the electric field of the Penning trap would force a charged particle to a circular orbit with the *free cyclotron frequency*

$$\omega_c = \frac{q}{m} \cdot B_0 \tag{3.5}$$

which is characteristic for each stored ion species by its charge-to-mass ratio.

Superimposing both the electric field and the magnetic field, the free cyclotron frequency is pertubed, resulting in the two independent frequencies of the radial motion

$$\omega_+ = \frac{\omega_c}{2} + \sqrt{\frac{\omega_c^2}{4} - \frac{\omega_z^2}{2}} \tag{3.6}$$

$$\omega_- = \frac{\omega_c}{2} - \sqrt{\frac{\omega_c^2}{4} - \frac{\omega_z^2}{2}}, \tag{3.7}$$

where the first is the so-called *reduced cyclotron frequency* and the latter the *magnetron frequency* [30]. The cyclotron motion at ω_c is hence split into two separate motions at frequencies ω_+ and ω_- with $\omega_+ + \omega_- = \omega_c$, a visualisation of the combined motion is given in figure 3.1. For hydogen-like carbon ions (C^{5+}) stored with a magnetic field of 6 T and a trapping voltage of U_0=100 V, typical frequencies are: $\omega_+ = 38.1\,\mathrm{MHz}$, $\omega_- = 12.575\,\mathrm{kHz}$ and $\omega_z = 978.9\,\mathrm{kHz}$. The applied trapping parameters B_0, U_0 and d determine the three motional frequencies which hence have a fixed relation for each ion species. In contrast, the amplitudes of the motions can be chosen independently for each motion: ρ_c - cyclotron radius, ρ_m - magnetron radius and z_0 the amplitude of the axial motion.

The ion motion is now the superposition of all three individual motions with their respective amplitudes. In cartesian coordinates the motion can be described by the following six equations:

$$x = \rho_+ \cdot \sin(\omega_+ t) + \rho_- \cdot \sin(\omega_- t) \tag{3.8}$$
$$y = \rho_+ \cdot \cos(\omega_+ t) + \rho_- \cdot \cos(\omega_- t) \tag{3.9}$$
$$z = z_0 \cdot \sin(\omega_z t) \tag{3.10}$$
$$v_x = \rho_+ \cdot \omega_+ \cdot \cos(\omega_+ t) + \rho_- \cdot \omega_- \cdot \cos(\omega_- t) \tag{3.11}$$
$$v_y = -\rho_+ \cdot \omega_+ \cdot \sin(\omega_+ t) - \rho_- \cdot \omega_- \cdot \sin(\omega_- t) \tag{3.12}$$
$$v_z = z_0 \cdot \omega_z \cdot \cos(\omega_z t). \tag{3.13}$$

The energy of each motion is connected to their respective amplitudes by the following equations [36].

$$E_+ = \frac{m\left(\omega_+^2 - \omega_z^2/2\right)\rho_+^2}{2d^2} \quad \text{energy of the reduced cyclotron motion} \tag{3.14}$$
$$E_- = \frac{m\left(\omega_-^2 - \omega_z^2/2\right)\rho_-^2}{2d^2} \quad \text{energy of the magnetron motion} \tag{3.15}$$
$$E_z = \frac{c_2 q U z_0^2}{d^2} \quad \text{energy of the axial motion} \tag{3.16}$$

For the trapping parameters given above, typical energies of C^{5+} for the three motions with an amplitude of 1 mm in the respective motion are: $E_+ = 289\,\text{keV/q}, E_- = -95.5\,\text{eV/q}$ and $E_z = 0.47\,\text{eV/q}$. In the case of the reduced cyclotron motion and the axial motion a reduction of the energy results also in a reduction of the amplitude. The energy in the magnetron motion is always negative since it is a drift motion in the crossed electric and magnetic fields, for a detailed discussion see [36]. Hence, reducing its kinetic energy leads to a widening of the magnetron orbit.

3.3. Ion excitation and selection

Ions captured from an external source or produced inside the trap have an arbitrary combination of all motional amplitudes ρ_+, ρ_- and z_0 and the trap content typically is a mixture of several ion species. Using a proper electric field configuration and excitation frequency, it is possible to excite ions with subsequent ion ejection (see figure 3.2a) or transfer energy from one motion to another (see figure 3.2b).

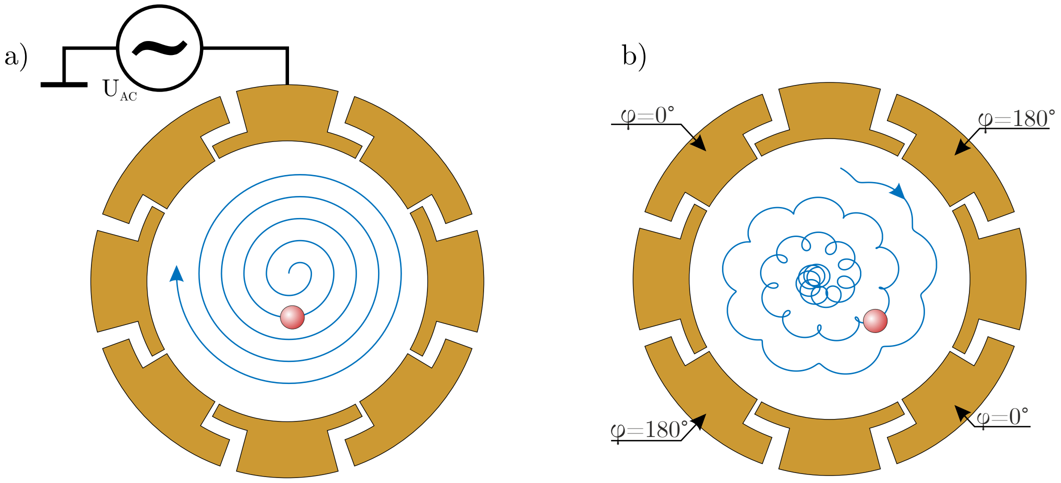

Figure 3.2.: a) Resonant excitation of the radial motion with an applied dipolar AC-signal and b) axialisation of an ion as example for the coupling of the two individual motions.

3.3.1. Single-frequency ion excitation

In case of ion excitation, there are two typical purposes - energy gain for efficient non-destructive detection [37] and ion selection by the ejection of unwanted ions [38]. In both cases, the ions are excited by an electric dipole field at the frequency of the respective motion. Figure 3.2a depicts the ion motion excited radially by a dipole field, where the ion gains energy in the cyclotron motion. The signal amplitude for non-destructive ion detection is hence increased and the ion can be detected easier. If the energy is increased further, the ion hits the trap electrode and is lost. This mechanism is used to clear the trap from unwanted ions.

3.3.2. Broadband excitation

The excitation technique described above will only affect ions with a certain frequency, while others are unaffected. In the experiment it is often useful to excite multiple frequencies or frequency bands simultaneously. Especially the axial frequencies of the stored ions are probably not known exactly and broadened, or multiple ion species are to be excited at once. This broadband excitation is realised by the so-called *SWIFT* (Stored Waveform Inverse Fourier Transform) - technique [38]. The SWIFT technique is visualised in figure 3.3. The frequency bands to be excited marked by the red boxes are merged to a certain intensity distribution in the frequency domain which is converted using an inverse fast Fourier

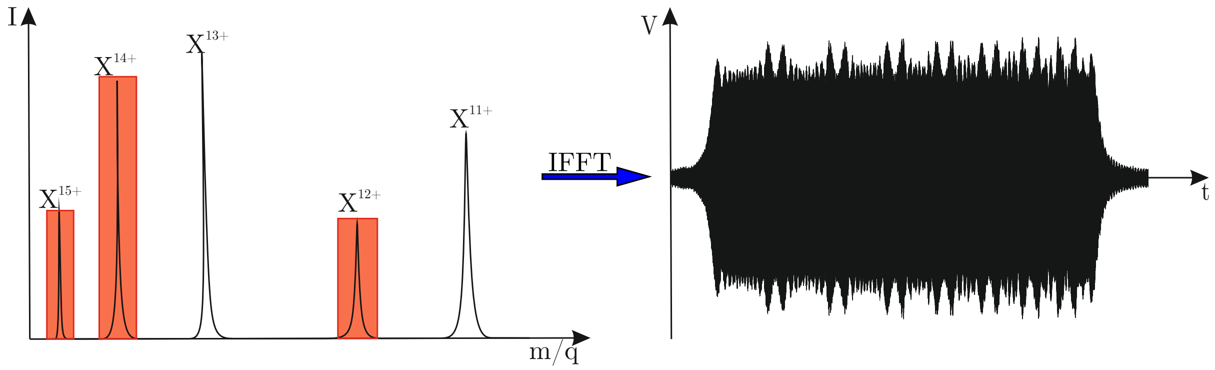

Figure 3.3.: Illustration of the SWIFT technique. The peaks denote ions stored inside the trap represented by their m/q-ratio. The red boxes are the excited frequencies. With an inverse FFT a time signal is calculated from the marked frequency bands.

transformation to a time-domain signal. This signal is then applied to an electrode. This way, the trap can be cleared from all unwanted ion species simultaneously. Details can be found in [74].

3.4. Properties of ensembles of ions

In the case of multiple ions stored inside the Penning trap, a variety of further effects have to be considered. The stored ions reduce the trapping potential by their charge resulting in an decrease of the axial frequency [39]. Considering ion-ion-interactions due to the Coulomb force, the ion cloud can be described as a non-neutral plasma [40]. In the case the potential energy of the particles resulting from their Coulomb repulsion is higher than their kinetic energy, the plasma is considered to be strongly coupled. Even without strong coupling, confined ion clouds show thermalisation via the Coulomb interaction [40].

3.4.1. Ion temperature and equilibrium

Ion ensembles stored inside an ion trap have an initial energy distribution depending on the conditions upon ion creation or capture. The energies of the individual ions will settle to an equilibrium after a certain time. If an ion ensemble is in thermal equilibrium, it can be described with a temperature T, and the distribution of the ions' kinetic energy $p(E)$ is a Maxwell-Boltzmann distribution described by [40]

$$p(E) = 8\pi\sqrt{m}\left(\frac{1}{2\pi k_B T}\right)^{\frac{3}{2}} E \exp\left(-\frac{E}{k_B T}\right) \tag{3.17}$$

$$\hat{E} = k_B T \quad \text{most probable ion energy} \tag{3.18}$$

$$\bar{E} = \frac{4}{\pi} k_B T \quad \text{mean ion energy.} \tag{3.19}$$

In real Penning traps, this equilibrium is established between the stored ions and the electronic noise temperature of the trap electrodes. This can be higher than the physical temperature of the trap. The equilibrium temperature depends highly on the temperature of the surroundig electrodes and the applied electronic circuits and on the magnitude of induced electronic noise.

Figure 3.4 shows the Boltzmann distributions for three different ensemble temperatures - 10,000 K ($\hat{E} = 1\,\text{eV}$) , 50,000 K ($\hat{E} = 5\,\text{eV}$) and 150,000 K ($\hat{E} = 15\,\text{eV}$). For high temperatures, the mean kinetic energy as well as the energy spread is very high. In the case of hot ions, the Maxwell-Boltzmann distribution is very broad and consequently the escape of high-energetic ions from the potential well is more probable.

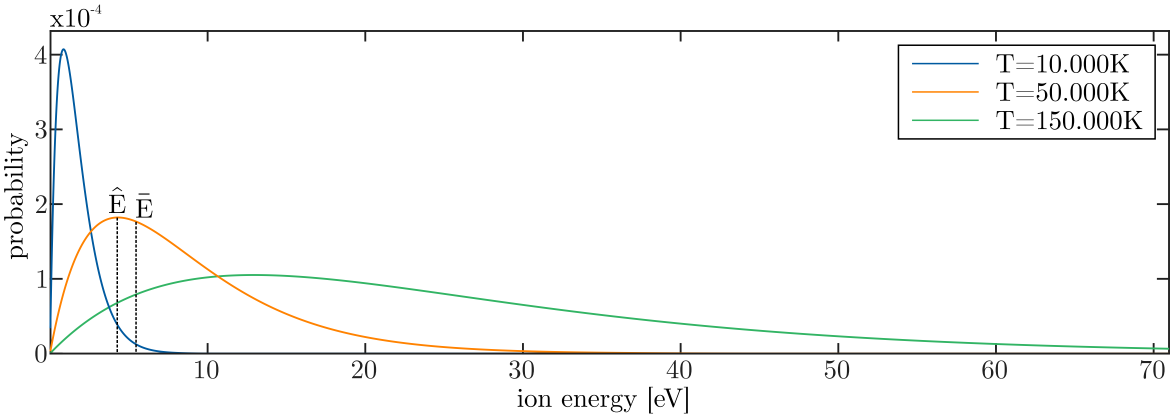

Figure 3.4.: Maxwell-Boltzmann distribution exemplarily for different temperatures and mean kinetic energies.

3.4.2. The ion cloud as plasma

At a low temperature, when the kinetic energy of the ions is comparable to the potential energy inside the ion cloud, it can be treated as a strongly correlated plasma. Depending on the ensemble properties, the ion plasma can be treated as fluid or as ion crystal. In the case of a single-species ion ensemble, a useful quantity to distinguish between these states is the plasma parameter [41]

$$\Gamma_P = \frac{q^2}{4\pi\epsilon_0 a_{ws} k_B T}, \tag{3.20}$$

where q is the charge, $k_B T$ the thermal energy of the ions and a_{ws} the effective ion-ion-separation.

$$\Gamma_P \ll 1 \quad \text{weakly correllated (gas-like) state} \tag{3.21}$$

$$2 < \Gamma_P < 174 \quad \text{fluid-like state} \tag{3.22}$$

$$\Gamma_P > 174 \quad \text{crystal-like state} \tag{3.23}$$

In the HILITE Penning trap, an ion clouds consisting of C^{5+} which is compressed to the maximum ion density, has a plasma parameter of more than 1, when the temperature is below 70 K and can also be recognised as fluid-like at the resonator temperature of 4 K. For ions with low temperatures, the ions arrange inside a small volume (see equations 3.14 - 3.16). The ion-ion-separation at which the Coulomb interaction is still significant can be estimated by the *Debye length* [42]

$$\lambda_D = \sqrt{\frac{\epsilon_0 k_B T}{2nq^2}}. \tag{3.24}$$

If it is much smaller than the dimensions of the ensemble, the ions can be considered to be strongly coupled and the ensemble can be treated as a rigid ion cloud. In the outer region of the ion cloud for a length comparable to the Debye length, the ion density rises almost step-like from zero to maximum. In the inner region it is constant at the maximum density.

3.4.3. The Rotating-wall technique

Ions in strongly correlated ensembles create a rigid ion cloud, whose shape can be controlled by an external torque [43]. This is realised by the application of a rotating dipole field with a frequency ω_r. The signal is applied to four different electrode segments with a 90° phase shift with respect to neighboring segments as depicted in figure 3.6a. The ions perform a global rotation around a common rotational axis, the so-called *rotating wall* [44]. Due

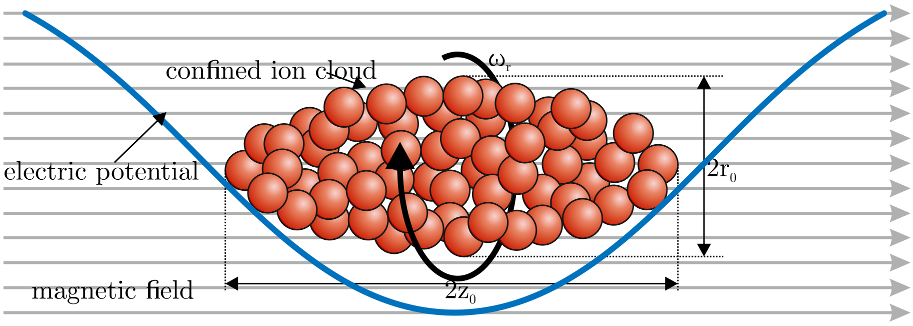

Figure 3.5.: Ion cloud confined in a Penning trap with an applied rotating electric dipole field. The cloud has a length of $2z_0$ and $2r_0$.

to the conservation of momentum, the increased rotational frequency has to result in the reduction of the radial extent and consequently the ions arrange in a spheroid, where the two principal axes in the radial direction have the same size and the third in axial direction may differ from the others. Figure 3.5 shows the geometry of an ion cloud with an axial extent of $2z_0$ and a radial extent of $2r_0$. The aspect ratio α of the ion cloud $\alpha = \frac{z_0}{r_0}$ can be controled by the trapping parameters B and U_0 as well as the applied frequency of the dipole ω_r[44].

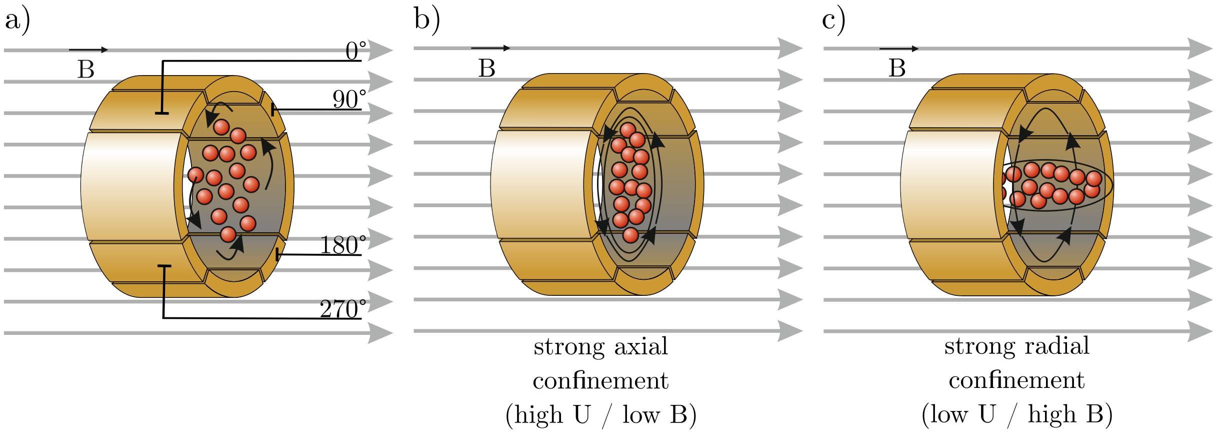

Figure 3.6.: Confinement of an ion cloud using the rotating wall technique. a) A rotating dipole field is applied to four segments of the ring electrode, b) strong axial confinement (oblate shape) c) weak axial confinement (prolate shape).

Figure 3.6a shows the phase shift of the signal applied to the four electrode segments. The ions follow the sense of the rotation of the signal. The ion density for the axial (n_a) and the radial (n_r) direction may differ from each other and can be calculated by [44]:

$$n_r = \frac{6\epsilon_0}{qa(\alpha)} \left(\frac{m}{2q} \omega(\omega_c - \omega) - \frac{U_0}{4d^2} \right) \tag{3.25}$$

$$n_a = \frac{6\epsilon_0}{qb(\alpha)} \frac{U_0}{2d^2}. \tag{3.26}$$

The coefficients in this equation are

$$b(\alpha) = 3\frac{\omega_z^2}{\omega_p^2} \tag{3.27}$$

$$3 = 2a(\alpha) + b(\alpha) \tag{3.28}$$

$$\omega_p = \sqrt{2\omega_r \cdot (\omega_c - \omega_r)}. \tag{3.29}$$

The parameter ω_p is the plasma frequency and the maximum ion density is achieved at $\omega_r = \frac{\omega_c}{2}$ and follows

$$n_{max} = \frac{B^2}{2\epsilon_0 m}, \tag{3.30}$$

the so-called *Brillouin limit* [44]. Both the axial and the radial ion density have this value. The dimensions of the ion cloud can now be determined from the ion densities, the ion number and the aspect ratio α. For prolate ion clouds ($\alpha > 1$) the aspect ratio can be calculated solving

$$b(\alpha) = \frac{3}{\alpha^2 - 1} \left[\frac{u_p}{2} \ln \left[\frac{u_p + 1}{u_p - 1} \right] - 1 \right] \quad \text{with} \quad u_p = \frac{\alpha}{\sqrt{\alpha^2 - 1}} \tag{3.31}$$

while for oblate ($\alpha < 1$) ion clouds the aspect ratio can be determined solving

$$b(\alpha) = \frac{3}{\alpha^2 - 1} \left[\frac{u_o}{2} \tan^{-1} \left[\frac{1}{u_o} \right] - 1 \right] \quad \text{with} \quad u_p = \frac{\alpha}{\sqrt{1 - \alpha^2}}. \tag{3.32}$$

The value $b(\alpha)$ is calculated with equation 3.27. Figures 3.6b and 3.6c show the two possible shapes for strong axial confinement and weak axial confinement, respectively [44].

3.4.4. Plasma modes

In confined ion clouds the interaction between the ions has a major influence on the ion ensemble which can be regarded as a plasma. This includes internal states of the plasma - so-called *plasma modes*. Plasma modes [44] are characterised with positive integer numbers l and m, and are described in terms of Legendre polynomials of the first and second kind P_{ml} and Q_{ml}[45]. They can be excited by externally applied signals and cause heating of the ions with subsequent ion loss. Applying dipole fields, (2,1) modes are most likely to be excited. (2,1) modes can be understood as a precession motion of the ion cloud's main axis around the magnetic field axis [44].

The frequencies of (2,1) plasma modes are strongly connected to the axial frequency ω_z (equation 3.4), the plasma frequency ω_p (equation 3.29) and the aspect ratio α. As these values are strongly connected to the particle properties and the trap parameters, also the plasma mode frequencies have a strong dependence on trap parameters and the particle properties. The frequencies of the (2,1) modes are given by [44]

$$\omega_{21}^k = (-1)^{k+1} \sqrt{-\omega_p^2 f_\alpha \left(\frac{\alpha^2}{3\eta_k} + \frac{1}{3}\right)} \tag{3.33}$$

$$\text{with } f_\alpha = \frac{3}{2}\left(\frac{1 - 3\omega_z^2/\omega_p^2}{1-\alpha^2}\right). \tag{3.34}$$

The negative sign in the case $k = 2$ can be interpreted as a rotation in the opposite direction than in the other cases. The parameters η_k are the solutions of the cubic equation

$$a_3\eta^3 + a_2\eta^2 + a_1\eta + a_0 = 0 \tag{3.35}$$

with the coefficients

$$a_0 = \frac{1}{3}\omega_p^2 f_\alpha \cdot \alpha^2 \tag{3.36}$$

$$a_1 = \frac{1}{3}\omega_p^2 f_\alpha \cdot (1 - 2\alpha^2) + (\omega_c - 2\omega_r)^2 \tag{3.37}$$

$$a_2 = \frac{1}{3}\omega_p^2 f_\alpha \cdot (\alpha^2 - 2) \tag{3.38}$$

$$a_3 = \frac{1}{3}\omega_p^2 f_\alpha. \tag{3.39}$$

The knowledge of the plasma mode frequencies for certain trapping conditions is necessary to avoid rotating wall excitation frequencies which cause ion heating. The other way around, the trapping parameters can be chosen properly to be free in the choice of the excitation frequency.

3.5. FT-ICR and the concept of mirror charges

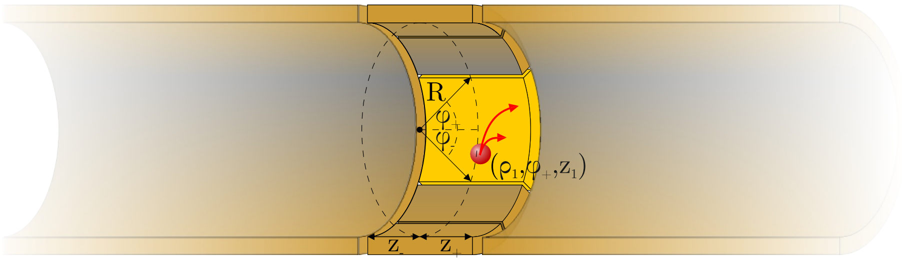

Figure 3.7.: Illustration of the principle of mirror charges. The ion (red) at position (ρ_1, φ_1, z_1) induces a voltage in the indicated electrode segment covering an area within the limits $(\varphi, z)\epsilon([\varphi_-, \varphi_+] \times [z_-, z_+])$. R is the curvature radius of the segment.

To detect ions inside the Penning trap the *FT-ICR (Fourier-transform ion cyclotron resonance)* technique is used [46]. This non-destructive ion detection technique is based on the concept of mirror charges. Here, a charged particle positioned in front of a conducting surface induces a charge and hence a corresponding voltage to the respective pick-up electrode as illustrated in figure 3.7 [47]. Typically these voltages are amplified resonantly or non-resonantly to achieve a sufficiently high signal strength [48].

The amplitude of the induced signal depends on the ion charge q, on the geometry of the pick-up electrode, and in particular on the position of the ion. The charge induced by a single ion is [49]

$$Q = R\varepsilon_0 \int_{z_-}^{z_+} \int_{\varphi_-}^{\varphi_+} \left.\frac{\partial V}{\partial \rho}\right|_{\rho=R} \mathrm{d}\varphi \mathrm{d}z, \tag{3.40}$$

depending on the perpendicular component of the electric field caused by the charged particle at the surface of the electrode integrated over the area of the electrode segment.

The geometry-dependent part of expression 3.40 can be expressed using the so-called *geometry function* Γ. Assuming a given electrode geometry, the geometry function depends only on the ion position and the induced charge can be written as:

$$Q_{ind} = -q_{ion} \cdot \Gamma(\rho_1, \varphi_1, z_1). \tag{3.41}$$

The corresponding induced voltage U_{ind} and current I_{ind} are:

$$U_{ind} = -\frac{q_{ion}}{C} \cdot \Gamma(\rho_1, \varphi_1, z_1) \tag{3.42}$$

$$I_{ind} = -q_{ind} \cdot \vec{\nabla}\Gamma(\rho_1, \varphi_1, z_1) \cdot \vec{v}, \tag{3.43}$$

where C is the capacitance of the electrode and $\vec{v}$ the velocity of the ions.
In the case of long electrodes there are analytical approaches [50], but in the more common case of an isolated pick-up electrode, the geometry function is calculated numerically. Following [47] the geometry function is identical to the spatial dependent potential created by the very same electrode set to unit voltage. Using a simulation software based on the finite-element method, the geometry function of any pick-up electrode configuration can be calculated.

3.6. Cooling concepts in Penning traps

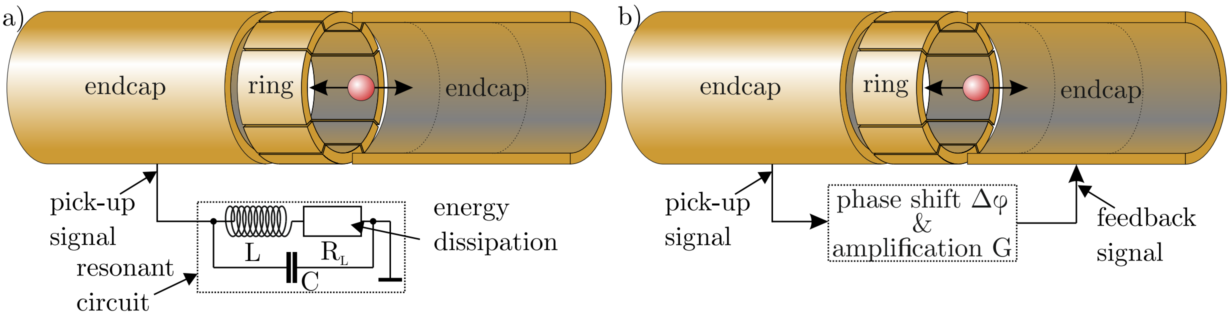

Figure 3.8.: a) Resistitve cooling of stored ions with an applied resonant circuit. b)General concept of active-feedback cooling of stored ions with an amplified and phase-shifted feedback signal.

The ions in a Penning trap have a certain energy distribution depending on the ion temperature and their correlation strength. For most experiments, ions with small energy spread and low mean kinetic energy are necessary or favourable. Also, the ion density with applied rotating wall is more homogeneous and higher with low-temperature ions.

Initially, produced or injected ions have a high energy and must be cooled in order to provide a well-defined ion ensemble for experiments. There are several cooling mechanisms, such as resistive cooling, sympathetic cooling, active-feedback cooling, evaporative cooling laser-Doppler cooling and buffer-gas cooling [51]. Resistive cooling and active-feedback cooling are favourable techniques in our Penning trap and will be described below. The energies of the different motions of the ions have to be reduced individually. Here, I will explain the cooling techniques for the axial motion only, but the techniques can be applied to other motions too.

3.6.1. Resistive cooling

The typical configuration for cooling ions resistively is depicted in figure 3.8a and always affects ions inside an ion trap, when the axial frequency is close to the resonant frequency of the attached resonator. With this technique, the temperature of the ions can be reduced down to the temperature of the resonant circuit [52]. The relevant quantity here is the electronic noise temperature of the circuit which ideally is identical to its physical temperature.

Ions stored inside a Penning trap induce a charge in the trap electrodes. The resulting current drives the resonant circuit connected to a particular electrode. When the ions are in resonance with the resonator, the current and hence the stored energy inside the resonator is maximum and the cooling is most efficient. The energy inside the resonator is then dissipated via the impedance of the resonator which is purely Ohmic in the resonant case and the energy loss $\mathrm{d}E/\mathrm{d}t$ can be calculated following

$$-\frac{\mathrm{d}E_z}{\mathrm{d}t} = \langle i^2 R\rangle = \frac{q^2 \cdot Z}{4mD_{\mathrm{eff}}^2} E_z, \tag{3.44}$$

where $\langle i^2\rangle$ is the mean squared induced current driving the resonator. Z is the impedance of the resonant circuit in the resonant case and is calculated following:

$$Z = \frac{L}{C \cdot R_L}. \tag{3.45}$$

The energy loss follows an exponential decay with the resisitive cooling time constant τ_R:

$$-\frac{\mathrm{d}E_z}{\mathrm{d}t} = \tau_R \cdot E_z. \tag{3.46}$$

Comparing the expressions 3.44 and 3.46, the cooling time constant can be found to be [53]:

$$\tau_R = \frac{q^2 Z}{4mD_{eff}^2}. \tag{3.47}$$

The geometry of the electrodes is represented by the so-called *effective electrode distance* D_{eff}. It is defined as an virtual distance of a pair of electrodes with infinite area which would be necessary to cause the same electric field as the trap electrode and can be calculated following [54]:

$$D_{eff}(x,y,z) = \frac{U_c}{\vec{\mathbf{e}} \cdot \vec{\mathbf{E}}_c(x,y,z)}. \tag{3.48}$$

In this formula, U_c is the voltage applied to the electrode, $\vec{E_c}$ the resulting electric field configuration and $\vec{e}$ the unit vector of the coordinate to be cooled. The effective electrode distance is obviously spatially dependent and hence the ion cooling efficiency is spatially dependent, too. For an arbitrary electrode configuration, the electric field - and hence the effective electrode distance - is typically calculated using common numerical simulation tools.

For ensembles of N ions the cooling time constant is highly dependent on the ions' phase with respect to each other. If all ions have the same phase, the induced current is N times larger and hence the damping time τ_N of N ions is [53]

$$\tau_N = \frac{1}{N}\tau_R. \tag{3.49}$$

This means that any centre-of-charge motion is dampened very rapidly. For ions with arbitrary phase, the time-averaged mean square of the induced current in equation 3.44 is

$$\langle i^2 \rangle = \underbrace{\sum_{j=1}^{N} i_0^2}_{=N\cdot\langle i_0^2\rangle} + \underbrace{\sum_{\substack{j,k=1\\ j\neq k}}^{N} \langle i_j i_k \rangle}_{=0,\text{ for symmetry reason}} \quad . \tag{3.50}$$

Consequently, ions with arbitrary phase have the same damping constant as a single ion [53].

3.6.2. Active-feedback cooling

Active-feedback cooling is a common technique to pre-cool ions in storage rings. There, this technique is called *stochastic cooling* [55]. In ion traps, this technique is used to cool ions below the limit of resistive cooling or to decrease the cooling time. The ion cooling principle is sketched in figure 3.8b. The signal is picked up at a certain electrode, amplified by a factor G, phase-shifted by 180° and applied via another electrode back to the ions continuously [51]. When T is the temperature of the resonator, the final temperature T_F of the ions reached with this technique is [56]

$$T_F = (1 - G) \cdot T. \tag{3.51}$$

Using this technique, the final temperature was reduced down to 850 mK at an environmental temperature of 5.2 K [57]. While the final temperature can be decreased, the cooling time constant for active-feedback cooling τ_f is increased compared the resistive cooling time constant τ_R and follows [56]

$$\tau_f = \frac{1}{1 - G} \tau_R. \tag{3.52}$$

It is also possible to use a negative gain factor G. In this case, the cooling time can be decreased significantly but with the cost of higher final temperature [58]. In the case of an ion ensemble, the cooling affects only the centre-of-mass motion. Its amplitude z_{cm} decays following [59]:

$$\frac{\mathrm{d}z_{cm}^2}{\mathrm{d}t} = \langle z_{cm}^2 \rangle \sigma_\omega, \tag{3.53}$$

where $\langle z_{cm}^2 \rangle$ is the expectation value of the square of the amplitude of the center-of-mass motion and σ_ω is the standard deviation of the axial amplitudes of the stored ions. Obviously, for efficient active-feedback cooling of an ion ensemble it is necessary to have a non-zero energy spread caused by trap anharmonicities and a non-zero centre-of-mass motion.

3.6.3. Buffer-gas cooling

Collisions between stored charged particles and residual gas inside the trapping region cause momentum und hence energy transfer from one to the other. If the temperature of the background gas is much smaller than the ion temperature, the stored particles are cooled. The cooling rate depends on the particle properties mass m and charge q as well as on the mobility M of the gas particles. Assuming a single-species ion ensemble colliding with a single component residual gas with background pressure p and temperature T, the cooling time constant is [60, 61]:

$$\tau = -2 \cdot \frac{m}{q} M \frac{p_0 T}{p T_0}. \tag{3.54}$$

Here, p_0 and T_0 are the respective values at the gas standard conditions. Examplarily, mobilities of different background gases are listed in table 3.1. The values are taken from [62].

Table 3.1.: Examplary mobility values of different residual gases. The values are taken from [62]. The values depend also on the species of the stored ions and the values can only be taken as a reference.

gas	**mobility M** [$\mathrm{cm^2\,V^{-1}\,s^{-1}}$]
hydrogen	12
helium	20 - 25
nitrogen	2.0 - 2.5
argon	1.0 - 2.5
carbon dioxide	1.2 - 1.6

3.7. Charge-state lifetime

A substantial contribution to the limited lifetime of ions stored inside a Penning trap is the collision with the residual gas and subsequent recombination between the highly charged ions and the residual gas. The ions' charge state decays following [53]

$$N = N_0 \exp\left(-\frac{t}{t_c}\right), \tag{3.55}$$

with N_0 - initial ion number of the initial charge state and t_c the lifetime. The lifetime t_c is strongly connected to the background pressure p and the temperature T of the stored ions as well as the residual gas following

$$t_c = \frac{1}{\sigma p} \sqrt{\frac{k_B T \mu_m}{3}} \quad \text{with} \quad \mu_m = \frac{m_R m_{ion}}{m_R + m_{ion}}. \tag{3.56}$$

The masses m_R and m_{ion} are the masses of the residual gas atoms and the stored ions, respectively. The cross section of the specific collision partners is given by σ. Typically, the classical *Over-the-Barrier* [63] model is used to describe the electron capture by a charged particle from a neutral atom. In this model, the cross section is expressed as

$$\sigma = \frac{1}{2}\pi R_C^2, \tag{3.57}$$

where R_C is the *effective collision radius* given in terms of the Bohr radius a_0 by

$$R_C = \frac{27.2a_0(2\sqrt{q/e}+1)}{I}. \tag{3.58}$$

The charge of the ion is given by q and I is the ionisation energy of the weakest bound electron in the residual gas atom. [36]

4. The ion cloud as laser target

The HILITE Penning trap is built to prepare a well-defined ion cloud for laser-ion experiments. In the experiment, the laser is focussed inside the ion cloud where the laser ionisation takes place. Working with ions stored inside the Penning trap has the big advantage that the shape of the ion cloud and its density can be controlled by the trapping parameters. In this chapter, I will describe how the laser is focussed in the trap centre and guided out of the setup. I will point out the benefits and challenges connected with the laser interaction of confined highly charged ions.

4.1. Focussing the laser inside the trap

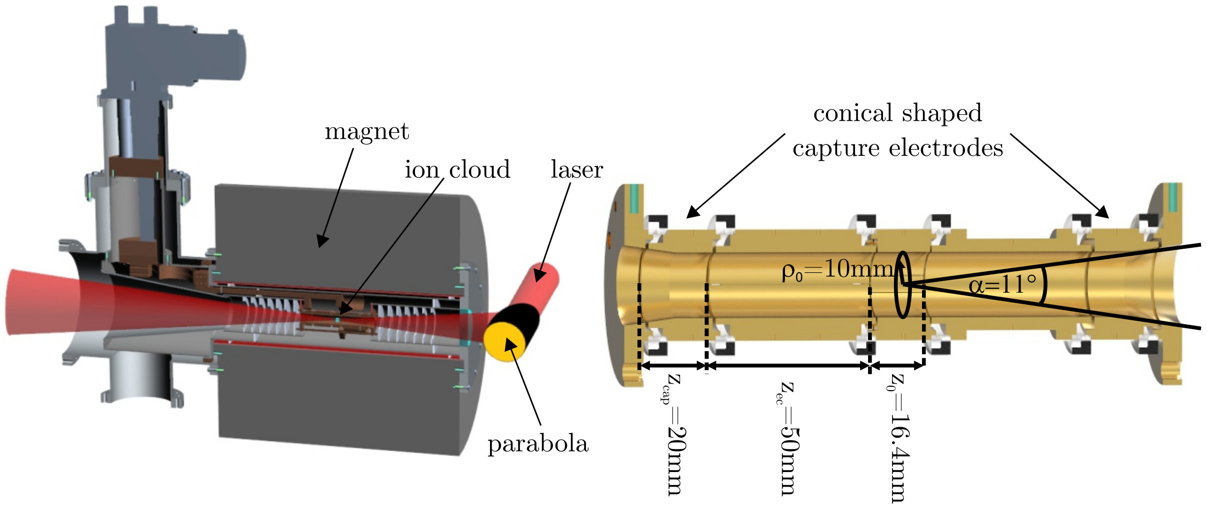

Figure 4.1.: Left: The laser is focussed inside the Penning trap setup by a parabolic mirror. Right: The trap capture electrodes have a conical shape to allow strong laser focussing.

To achieve high laser intensities in the focus, the laser beam has to be focused tightly. In the high-intensity regime, this is done by the use of coated parabolic mirrors with a focal length of a few centimetres up to metres. The focussing mirror is placed outside the magnet bore as shown in figure 4.4, wherefore the minimum focal length is about 500 mm. The minimum achievable focus diameter is connected directly to the laser parameters and the properties of the focussing mirror. In particular, a large full opening angle α shown in figure 4.1 is necessary to have a small focal diameter. In order to increase the acceptance angle of the trap, the capture electrodes and the endplates of the trap are conically shaped to allow a full opening angle of the laser of $\alpha = 11°$ which corresponds to an aperture of f/5.2. For example, a titanium:sapphire laser with a central wavelength of $\lambda = 800\,\mathrm{nm}$ is focussed to a beam diameter of about 4.2 µm with this configuration in the diffraction limit. In reality, the minimum beam diameter is also limited by the beam quality factor M^2. The higher the beam quality factor, the larger is the minimum possible laser focus diameter. For lasers with a gaussian intensity distribution, the parameters defining the shape of the laser focus are: f - focal length, h - $1/e^2$ diameter of unfocused beam, M^2 - beam quality factor and λ - laser wavelength [64]. The shape of the laser focus can be calculated using the concept of transfer matrices as desribed in [65].

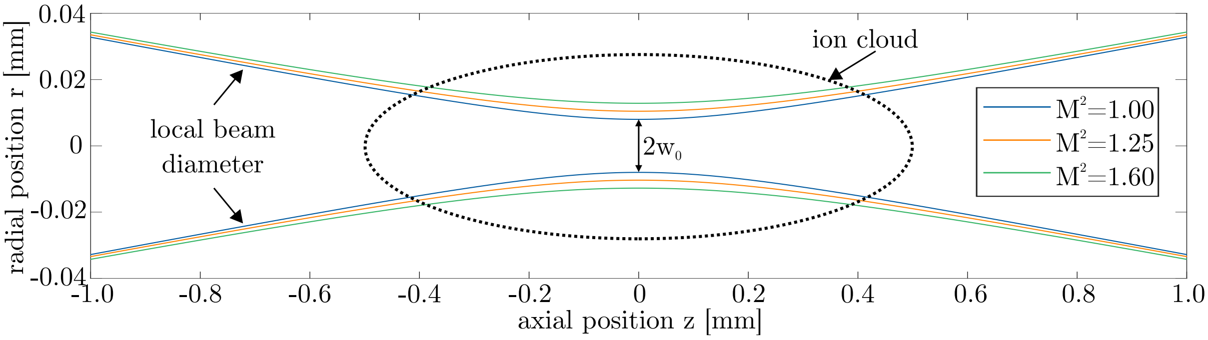

Figure 4.2.: Dependence of the laser waist ($2w_0$) with respect to the beam quality factor M^2. The higher the quality factor, the larger the focal diameter and hence the lower the maximum laser intensity. The laser intensity in the sketched ion cloud is spatially dependent. Consequently, the ionisation probability also depends on the position of the ion with respect to the laser focus.

Figure 4.2 depicts the shape of lasers with different beam qualities up to $M^2 = 1.6$, where the focus diameter is increased significantly. The lines denote the local beam diameter $w(z)$ defined by the $1/e^2$-value at certain axial positions with respect to the position of the laser waist. Especially the diameter of the waist w_0 of the laser is strongly connected to the laser parameters and hence the maximum laser intensity and the size of the interaction volume are. The dashed line sketches the shape of an ion cloud stored in the trap centre.

4.2. Ion cloud formation and overlap with the laser pulse

As described in section 3.4.3, confined charged particles can be arranged actively inside the ion trap controlled with the trap parameters. In comparision to a solid target with a particle density of typically $10^{30}\mathrm{mm}^{-3}$ or gases with $10^{11}\mathrm{mm}^{-3}$, ionic targets have a density of up to $10^{6}\mathrm{mm}^{-3}$. The big benefit of working with confined ions is the fact that their positions and their number inside a certain volume can be predicted reliably. Ion clouds cooled down to temperatures well below 100 K have a sharp edge and the ion position is well known. For a single-species ion cloud the cloud parameters are well defined for given trap parameters U_0 and B. The shape and dimensions of the cloud are given by equations 3.27 and 3.28 and the density by equation 3.30.

The ionisation probability is highly dependent on the laser intensity and can be calculated with the ADK theory given by equation 2.14. Moreover, the temporal peak intensity I_0 at the position of a certain ion inside the focal volume is dependent on the axial and radial position of any ion with respect to the focus position of the laser. The local intensity of a laser with a temporal peak power of P_{max} at position (r,z) relative to the laser focus located at (0,0) is described by

$$I(r,z) = 2 \cdot \frac{P_{max}}{\pi w(z)^2} \cdot \exp\left(\left(-\frac{r}{w(z)}\right)^2\right). \tag{4.1}$$

Hence, the ionisation probability $P_{ion}(Z,q,I)$ also has a spatial dependence and the overall number of prospected further ionised ions N_{ion} can be described by the following expression:

$$N_{ion} = \pi \cdot n \cdot \int_{-z_0}^{+z_0} \int_0^{r_0} r \cdot P_{ion}(Z,q,I(r,z)) \mathrm{d}r \mathrm{d}z. \tag{4.2}$$

In this equation, the ions are assumed to be distributed homogeneously and continuously with the ion number density n. In fact, the positions are distributed discretely and the mean distance between any two ions is of the order of 10 µm in the case of a strongly correlated plasma. Consequently, this equation is only valid when many ions are ionized with a single shot or when several laser shots interact with the target with a depletion much smaller than the initial ion number. Combining the information of ion cloud shape, laser-focus shape and intensity-dependent ionisation probability, the prospected number of ions can be calculated.

4.3. The laser-beam dump

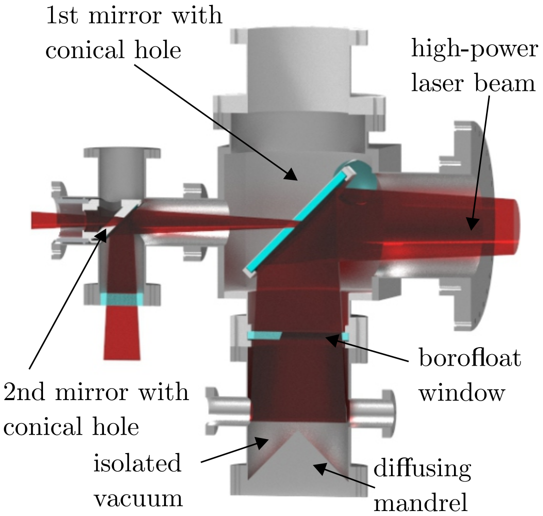

Figure 4.3.: Laser-beam dump for high-power laser pulses. The first stage consists of two separated chambers, where the main chamber has a mirror and the second contains a mandrel with a diffusing surface.

During the interaction with the stored ions, the laser only loses a very small amount of energy. That is why there has to be a certain volume where the laser is dumped. Here are two main challenges:

- the collinear guided laser and the ions have to be separated
- inside the vacuum the laser must not hit any metallic wall.

To accomplish both demands, I have designed, built, and tested a *beam dump*, consisting of two stages, where the first is separated into two vacuum chambers by a borofloat laser window as depicted in figure 4.3. The main chamber contains a mirror with a conical hole under 45° with respect to the surface normal. This allows the ions to pass the mirror into the trap. The remaining mirror area reflects 99% of the laser through a window onto a diffusing mandrel which destroys the structure of the laser pulse. This chamber has a separated vacuum, so any ablated particles do not pollute the trap vacuum. The part of the laser beam which passes the hole in the mirror is reflected by another mirror about half a metre downstream through a laser window to the outside and is dumped there. Further downstream, a 90°-bender for ions is foreseen, where the laser is guided through. Afterwards it hits a diffusing wall. As the beam power is less than 1% of the initial power and widened up, there are only a few ablated particles which are far away from the laser ion interaction volume and do not pollute the interaction volume seriously.

4.4. Prospected ion number

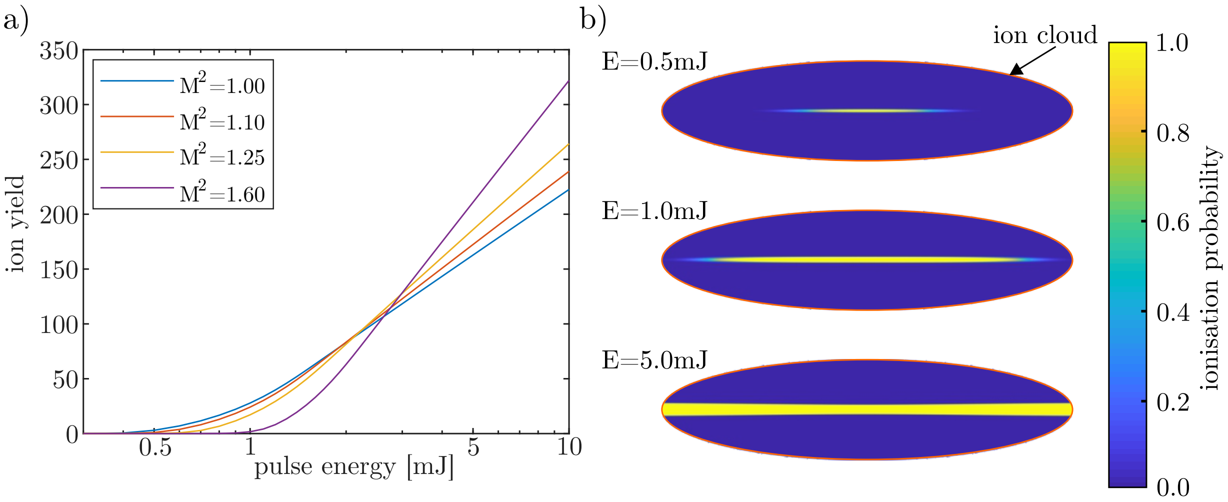

Figure 4.4.: a) Pulse-energy dependence of the ion yield for different beam qualities with 10,000 Ar^{4+} ions as target forming a prolate ion cloud. Here I assume a titanium:sapphire laser with a pulse duration of 40 fs focussed by a parabola with f/30. b) The contour plots of the ion clouds show the spatial dependence of the ionisation propability inside the ion target for different pulse energies.

Using a well-known ionic target, an upper and lower integration limit in equation 4.2 is defined sharply by the axial extent of the ion cloud. For low laser intensities the interaction volume is determined by the laser intensity only and is located in the very region of the laser focus, while for higher intensities, when ions over the whole cloud length are ionised, the axial extent of the ion cloud limits the interaction volume. In the latter case, the ion number increases with the logarithm of the intensity I, resulting from radial increase of the focal volume only. Figure 4.4b shows the ionisation probability and hence the interaction volume for different pulse energies. Figure 4.4a shows a calculated plot of the expected ion number with a confined Ar^{4+} cloud containing 10,000 ions irradiated with a focused 800 nm titanium:sapphire laser. The ions are stored at a magnetic field of 3 T and a trap voltage of U$_0$ = 350 V. The ion cloud is assumed to be compressed to the Brillouin limit with a particle density of $n = 0.6 \times 10^6\,\mathrm{mm}^{-3}$. The cloud diameter and length are 200 µs and 800 µm, respectively. The laser is focused by a mirror with a focal length of f = 550 mm to a focal diameter of 10 µm in the case of a beam quality $M^2 = 1$. The plot shows the number of ionised ions in relation to the pulse energy for different beam qualities. Obviously, the threshold pulse energy is higher with a less focussed laser beam but however the expected ion yield is better at high pulse energies. Furthermore, the slope of the curves in logarithmic scale shows a clear dependence on the beam quality. This could offer a chance to deduce the beam quality in situ out of the slope from a logarithmic scaled pulse energy.

4.5. Plasma modes

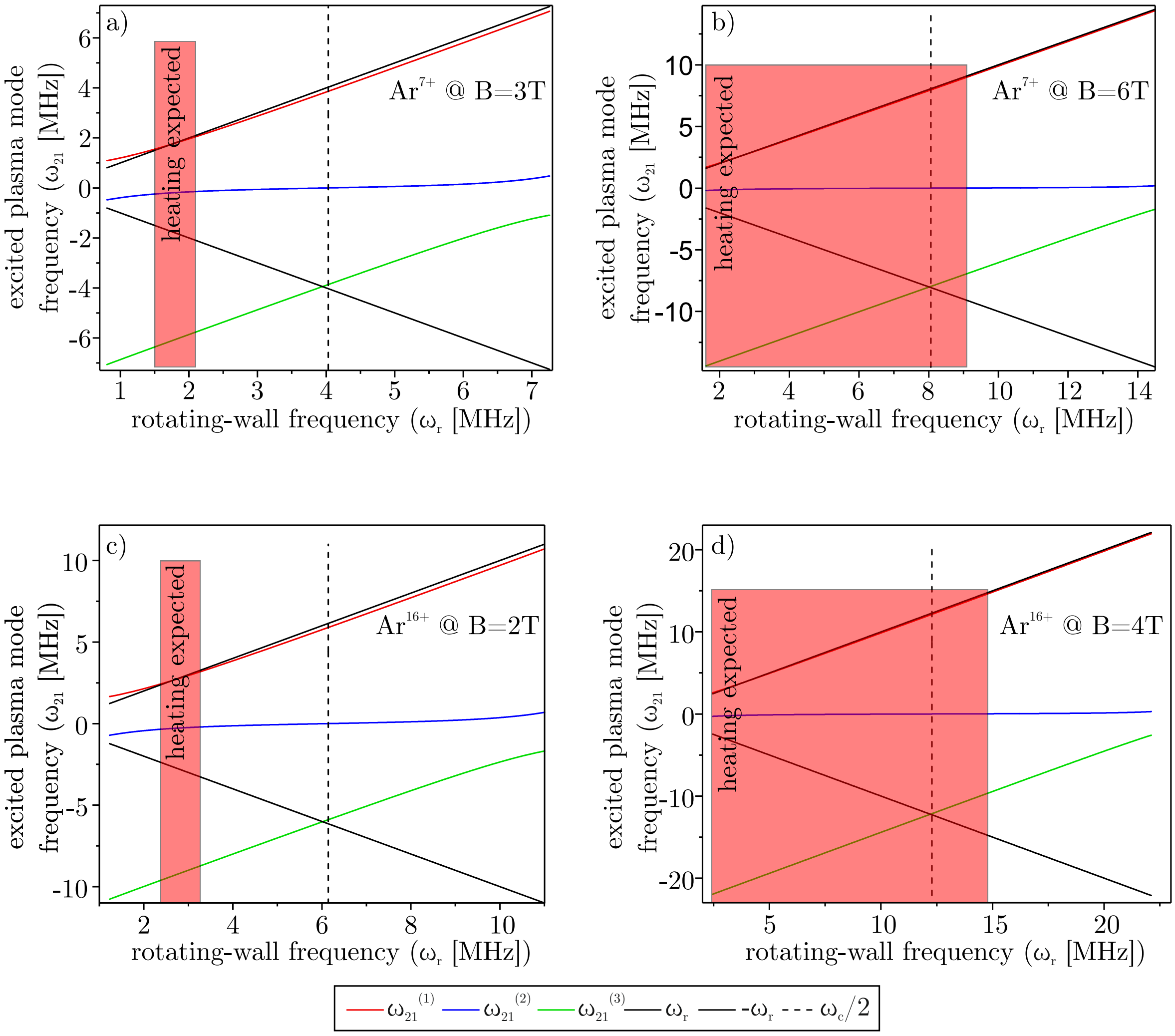

Figure 4.5.: Plasma modes of argon at two different charge states for a low (left column) and a high (right column) magnetic field strength. For high magnetic fields an excitation at the Brillouin frequency will cause significant ion heating.

To have a huge number of ions inside the interaction volume, the ion cloud has to be confined and compressed using the rotating-wall technique. Additionally, to have also a sharp boundary, the ions have to be cooled to low temperatures. In this limit of a strongly coupled plasma, the strength of plasma modes is increased [44]. When the excitation frequency matches a plasma mode frequency of the confined ion cloud, it is heated and the strength of confinement is reduced resulting in a decreased ion density and ion homogeneity. The frequencies of the plasma modes are calculated by equation 3.33. In the case of strong radial confinement and comparably weak axial confinement, the frequency of the plasma modes almost matches the excitation frequency. Holding the trapping parameters constant, the aspect ratio $\alpha = z_0/r_0$ and hence the ratio between radial and axial confinement increases linearly with the charge-to-mass ratio of the ions. Consequently, with highly charged ions, the plasma modes are close to the excitation at high magnetic fields and comparably low trapping voltage. Figure 4.5 shows the (2,1)-plasma modes of Ar^{7+} and Ar^{16+} stored and confined with a trapping voltage of 350 V at different magnetic field strengths. The maximum possible electrode voltage is 400 V limited by the surface quality. Bharadia et. al. investigated ion clouds of Ca^{+} ions stored inside a Penning trap [43]. When the difference between excitation frequency and plasma mode frequency was smaller than 3% of the excitation frequency, ion loss was observed. Using this result and transfering it to clouds of highly charged ions, the possible critical regions of expected ion heating can be found. These regions are highlighted by the red boxes. As the ion density is identical for the radial and the axial direction at the Brillouin frequency, this frequency is the most favourable frequency to excite and hence has to be outside of the critical regions. Although plasma frequencies have not been investigated for highly charged ions in an experiment so far and there is no proof that the outcomes of [43] can be transfered one-by-one, an upper limit of the applicable magnetic field strength of 3 T in the case of Ar^{7+} or even only 2 T for Ar^{16+} should be taken into account, when predicting the possible number of ions in the interaction region. The real limits will be measured in upcoming experiments.

5. HILITE: setup and characterising measurements

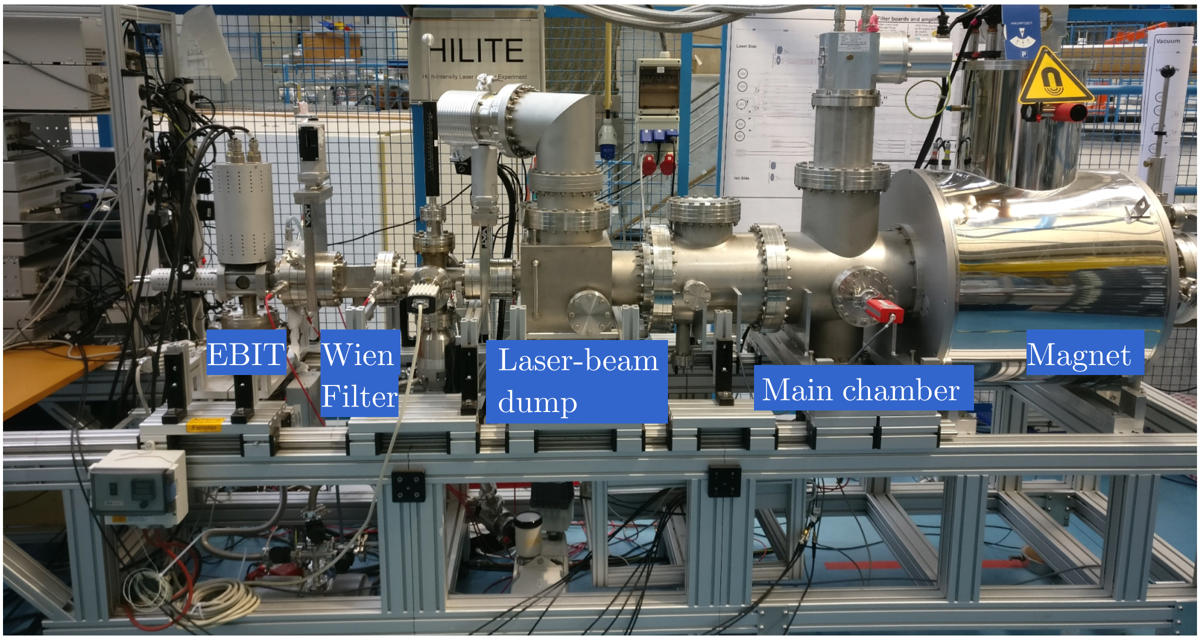

Figure 5.1.: Full experimental stand consisting of EBIT, Wien Filter, laser-beam dump, main chamber and the magnet containing the trap (from left to right).

The HILITE Penning trap is an experimental device to provide a well-defined ion target for laser experiments. It is designed in a so-called cylindrical open-endcap design [34] to allow access from both sides for ion loading and laser access. The Penning trap is equipped with several non-destructive and destructive ion measurement devices in order to characterise the laser reaction educts and products. For ion production, we use an EBIT (Electron-beam ion trap) which provides ions up to high charge states, for example Ar^{16+}. The magnetic field is provided by a superconducting magnet which is capable of producing a magnetic field of up to 6 T in the centre. For dynamic ion capture, the setup is equipped with an integrated pulsed drift tube for ion deceleration as well as two fast switched electrodes for ion re-bunching and ion capture. The setup is independent from any external ion beam line and can hence be operated at different laser facilities.

The overall setup has a length of about 3 m and a height of less than 2 m. The width is about 70 cm. These compact dimensions allow the use at different laser facilities. Figure 5.1 shows the full setup consisting of ion source (EBIT), Wien filter, laser-beam dump, main chamber and magnet with electrode stack. In this chapter I will describe the experimental apparatus and will characterise the devices. In particular, I will explain the capabilities of the setup to count ions inside the trap and while they are flying into or out of the trap.

5.1. The ion source - monochromatic ions

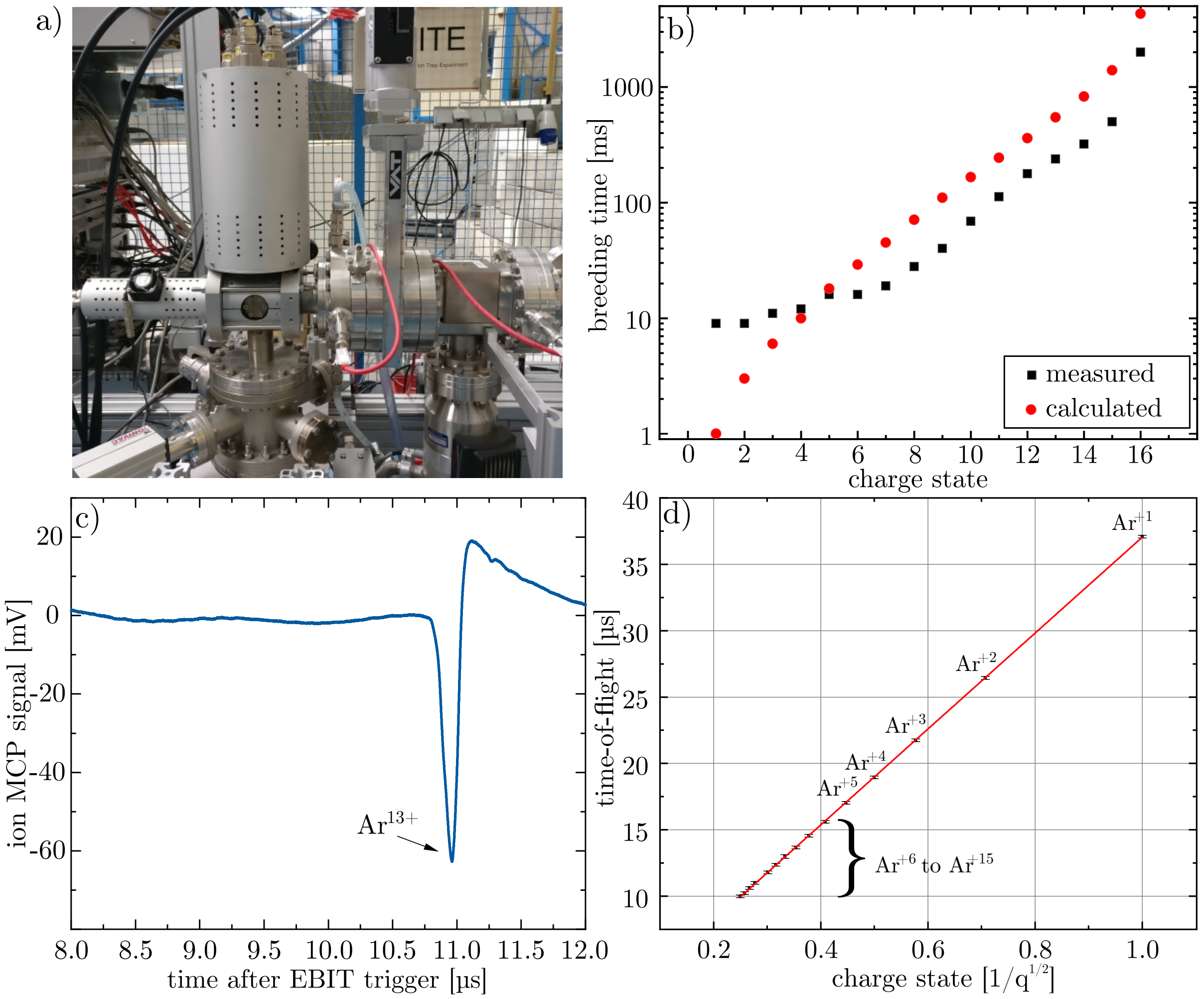

Figure 5.2.: a) Photo of the EBIT and the Wien Filter. b)measured and calculated optimum breeding time t_b for each argon charge state up to q=16. The calculation was performed with CBSim3 [66]. c)typical ion signal on the MCP acquired with an oscilloscope d) dependence of the time of flight on the charge state [67].

As ion source we use a commercially available *DREEBIT*. The ions are created using an intense electron beam ionising initially neutral particles. A detailed working principle can be found in [68]. During ion creation, the axial confinement is achieved with a set of three drift-tube electrodes. The drift-tube electrode which is closest to the output can be switched fast to a lower potential in order to extract ion bunches out of the EBIT. The moment of ion release is controlled by an external delay-gate generator.
The dominant charge state of the desired element produced by the EBIT depends on the EBIT parameters, namely:

- breeding time t_b - time the ions are trapped inside the EBIT
- U_{trap} - depth of the trapping potential
- U_{drift} - potential of the drift tube with respect to ground
- U_{cat} - cathode voltage which controls the kinetic energy of the electron beam.

The velocity of the extracted ions with charge q and mass m is controlled by the potential of the drift tube following:

$$v = \sqrt{\frac{2 \cdot q \cdot (U_{drift} - U_{trap})}{m}}. \tag{5.1}$$

The extracted ions pass a Wien filter which uses a crossed electric and magnetic field to filter the ions with respect to their velocity [69]. As the velocity depends on the charge state (see equation 5.1) the Wien filter also acts as charge filter.
The ions are created from an injected gas with a background pressure of typically 2×10^{-9} mbar and the cathode voltage is set to 3000 V to ionise the gas. Using a fixed acceleration voltage of 979 V and a magnetic flux density of 140 mT we have scanned the Wien filter voltage to detect different charge states. To identify the individual charge states we use a micro-channel plate (MCP) as destructive ion detector placed approximatly 2.40 m downstream and have measured the time of flight. Figure 5.2c shows a time-of-flight signal of Ar^{13+} ions detected with the MCP and recorded by an oscilloscope. The time of flight is relative to the opening pulse of the EBIT. We have tuned the voltage of the Wien filter and found several ion signals with different times of flight. Plotting the time of flight as a function of $1/\sqrt{q}$, assuming that the time of flight of the slowest ion species can be denoted to be Ar^{1+} and the following are occurences of the next charge states in ascending order, we have obtained a linear function as expected. For each charge state we have optimised the breeding time to obtain a maximum ion signal [67].

5.2. The magnetic field

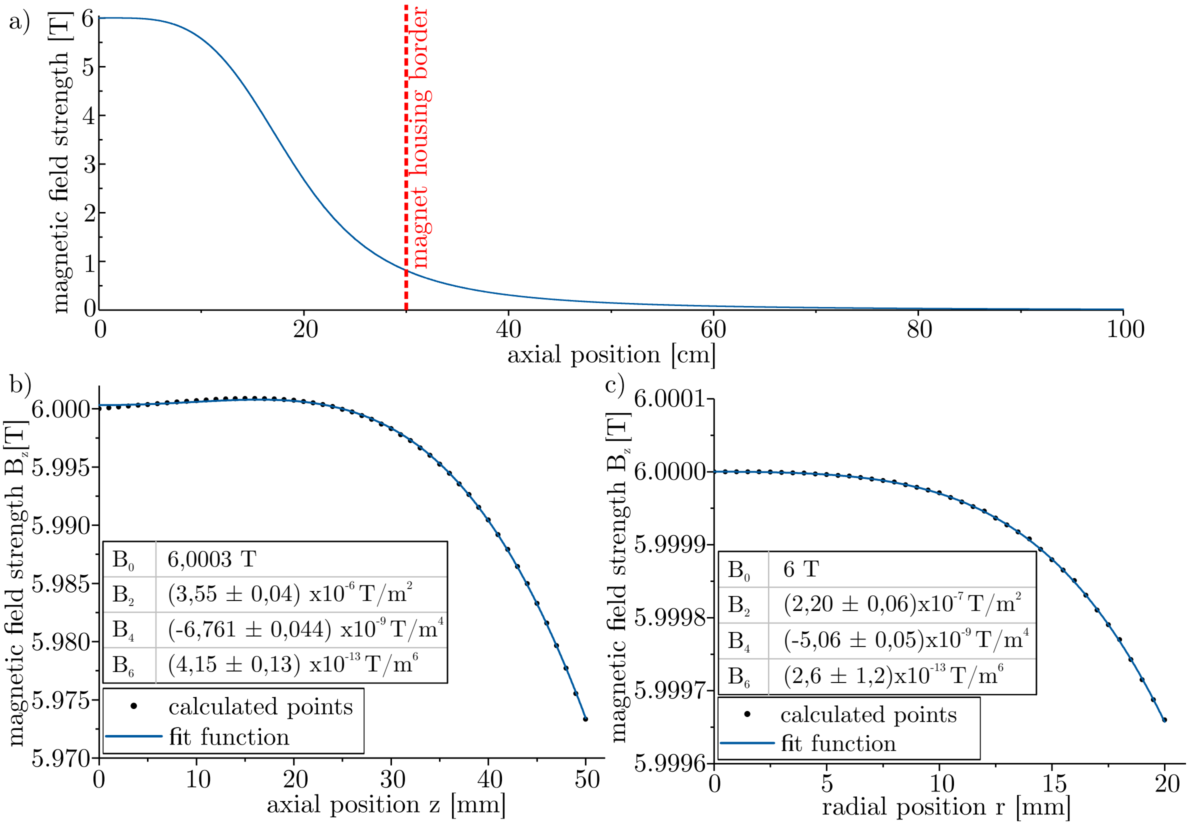

Figure 5.3.: Magnetic field plots of the HILITE magnet. a) Along the magnet axis b) Along the magnet axis close to the trap centre c) In the radial direction in the trap centre. The calculated data was provided by the manufacturer of the magnet.

The magnetic field of the HILITE Penning trap is created by a superconducting magnet which is equipped with a cryostat maintaining a temperature of less than 5 K. The maximum achievable magnetic field strength in the magnet centre is 6 T with a homogeneity better than 10×10^{-6} in a region of 10 mm around the centre. The magnet is also optimised to have a stray field which is below 5 mT at a distance of 1 m from the magnet housing (details in section A.1). Figure 5.3a shows the magentic field strength along the magnetic axis. The dashed vertical line denotes the end of the magnet bore. To calculate the inhomogeneity parameters of the magnet I have taken the design values and plotted the axial magnetic field component along the z-axis and along the r-axis. The results are depicted in figure 5.3b and 5.3c. The fitting parameters differ from each other slightly. To estimate any ion-energy dependent frequency shifts due to the magnetic field inhomogeneity one has to take the respective parameters B_2 and B_4 [36] into account depending on, whether the shift is caused by high axial or radial energy.

5.3. The temperature shields

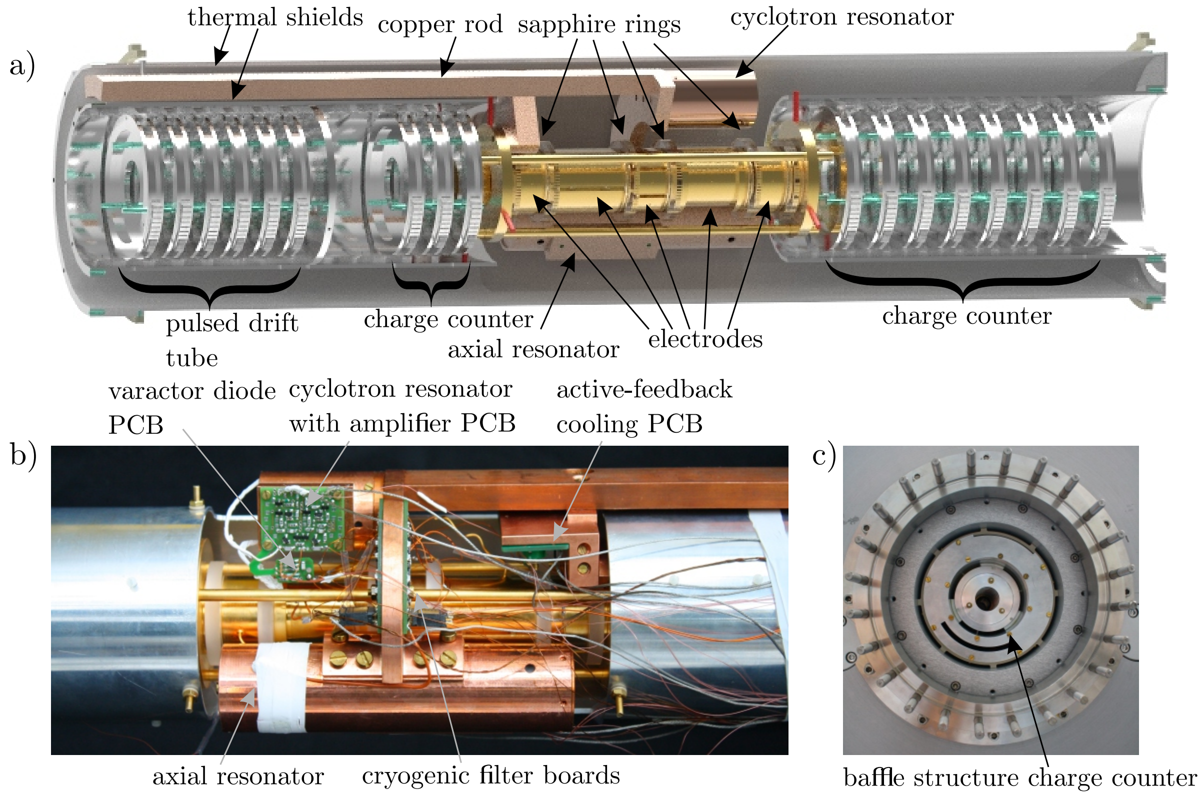

Figure 5.4.: a) A CAD drawing of the outer and inner temperature shield inside the magnet bore. The electrodes are surrounded by the shields to protect them from the ambient temperature. b) Photo of the trap electrodes, the resonators and the cryogenic electronics. c) Inner and outer shield inside the magnet bore. Inside the inner shield the baffle structured charge counter is placed.

The trap electrodes are nested inside a 45 K temperature shield to be thermally protected from the ambient-temperature radiation. The electrode stack itself is kept at a temperature of 4 K to allow cryogenic pumping in order to achieve a low background pressure in the trapping volume and correspondingly long ion storage times. The trap is connected to the 4 K stage of the cryostat with a copper rod. Figure 5.4a shows a CAD drawing of the outer and inner temperature shield housing the trap electrodes inside and figure 5.4b shows a photo of the trap with the axial and radial resonator housing and the cryogenic electronics.

The baffle structures on either side of the trap reduce the number of particles moving from the outside into the trap centre and hence improve the vacuum inside the storage volume. These baffle structures are also used as charge counters and as pulsed drift tube and are described later in detail. As the ions will be injected from the left and the laser from the right, in this thesis the sides are called *ion side* and *laser side*, respectively.

5.4. The trap electrodes

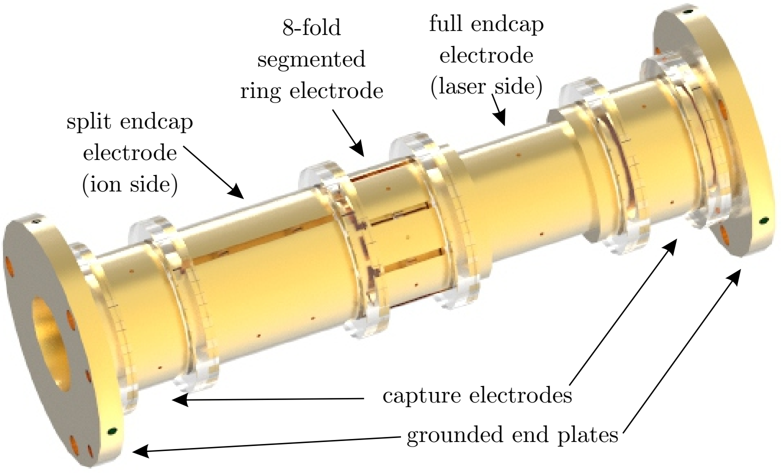

Figure 5.5.: The electrode stack of the HILITE Penning trap consisting of capture electrode, split endcap electrode, 8-fold segmented ring electrode, full endcap electrode, and capture electrode (from left to right). The electrodes are separated by rings made of sapphire.

The HILITE Penning trap is a cylindrical Penning trap with an open-endcap design [70]. The anharmonic parts of the confining potential represented by the higher-order parameters in equation 3.2 are compensated mechanically by an appropiate ratio between the endcap separation z_0 and the inner diameter r_0 [34]. The trap depicted in figure 5.5 consists of five electrodes, where the inner three (endcap - ring - endcap) maintain the trapping potential and the outer two are dedicated for the dynamic capture of injected ions. The electrode stack is held by two grounded endplates at both sides.

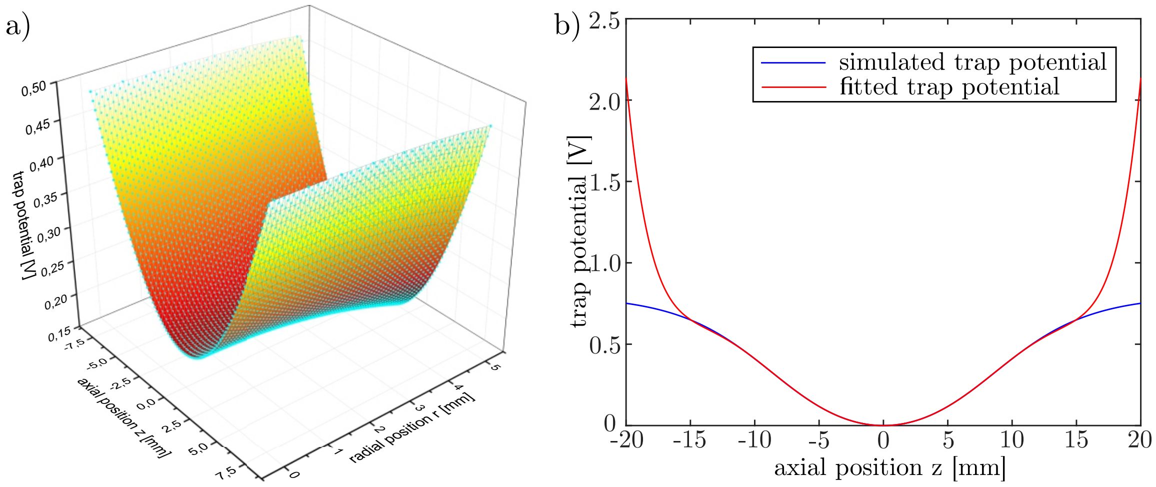

Figure 5.6.: a) The calculated trap potential is given by the turquoise points. The surface is a two-dimensional fit function with equation 3.2 up to the 8th order. b) The cross section along the z-axis over a large axial range. The red curve is the calculated curve from the fit parameters.

5.4.1. The trapping potential

The trapping potential is maintained by the ring electrode and the two endcap electrodes with a separation of the ring electrode from the endcap electrodes of 0.5 mm.

To determine the geometrical parameters $\mathrm{c_k}$ of the trap I have performed a numerical calculation of the trap potential with the FEM - solver ComSol [71]. The voltages of both endcap electrodes is set to 1 V, while the ring electrode is set to ground. Figures 5.6a and 5.6b show the electric potential inside the r-z - plane and a cross section along the z-axis, respectively. As fit function I have used a polynomial up to 8th order according to equation 3.2 and the calculated ComSol data in the interval $r = [0, 5]\,\mathrm{mm} \times z = [-8, 8]\,\mathrm{mm}$. Close to the trap centre the potential is well described by the fit function. The resulting trap parameters are shown in table 5.1. The characteristic trap parameter d is calculated following equation 3.3 directly from the design electrode geometry.

Table 5.1.: Geometrical parameters of the HILITE Penning trap. The parameters $\mathrm{c_0}$ to $\mathrm{c_8}$ are determined with a polynomial fit of the potential and the characteristic trap parameter d is calculated from the trap design values.

$\mathrm{c_0}$	$\mathrm{c_2}$	$\mathrm{c_4}$	$\mathrm{c_6}$	$\mathrm{c_8}$	d
0.401270	0.59567	0.00365	-0.04532	0.00732	7.93 mm

5.4.2. The eight-fold segmented ring electrode

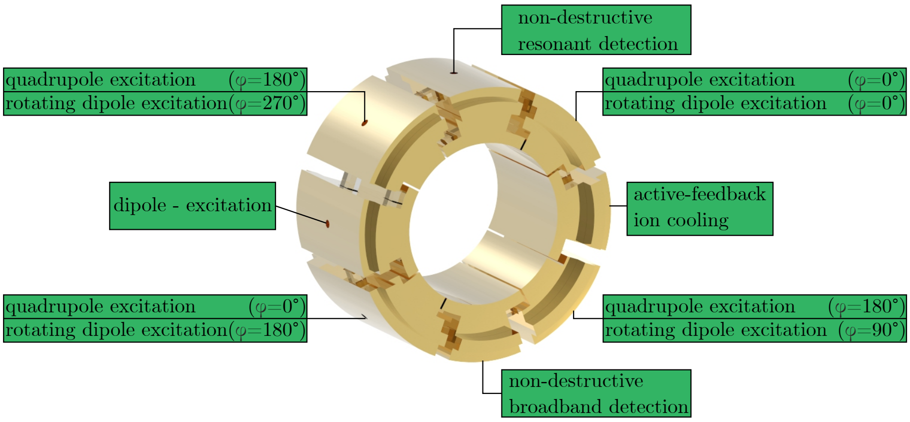

Figure 5.7.: Schematic drawing of the manipulation and non-destructive ion-detection techniques applied via the ring electrode. The ring electrode consists of eight segments where four of them cover 60° each and the others cover 30° each.

The HILITE Penning trap is equipped with an eight-fold segmented ring electrode to allow a variety of ion manipulation techniques, e.g. resonant excitation of the radial motions, ion axialisation and ion-cloud formation as well as non-destructive ion detection. Four segments have an azimuthal extent of 60° and the other four cover 30° each. Figure 5.7 shows a CAD drawing of the ring electrode with schematics showing the respective detection and excitation mechanisms which are applied to the segments.

The resonant cyclotron non-destructive detection

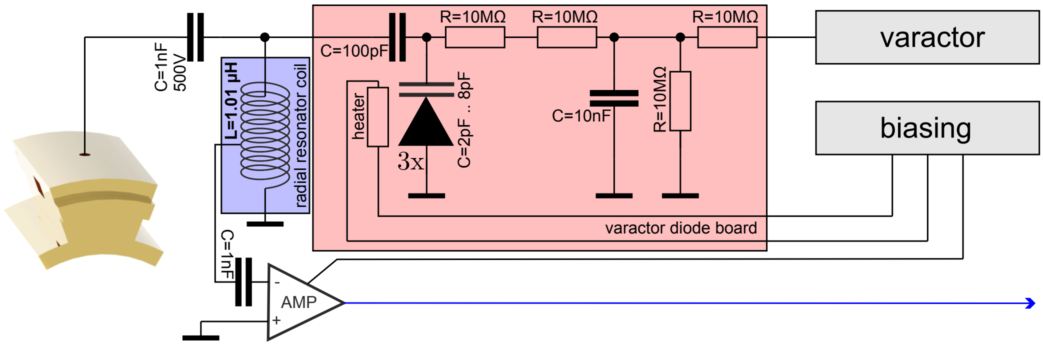

Figure 5.8.: Radial resonator (blue) connected capacitively to the ring-electrode segment. The resonant frequency can be tuned applying a bias voltage to the set of three parallel varactor diodes (red). This set is represented by a single symbol.

For the non-destructive ion detection we pick up und amplify the signals of the ions resulting from the cyclotron motion. For resonant detection we have applied a non-superconducting coil as resonator. We have decided for a non-superconducting detection, as it has no demand for extremly low temperatures. As the radial frequencies of the ions are fixed due to the applied magnetic field, we have equipped the resonator with a tunable capacitance - a so-called *varactor diode*. Applying a DC-voltage between 0 V and 10 V to a set of three parallel varactor diodes changes the capacitance [72], allowing a shift of the resonance frequency of the resonant circuit. Figure 5.8 shows the full resonant circuit connected to the ring-electrode's segment including the varactor diodes.

Table 5.2.: Electronic properties of the radial resonator.

resonance frequency f_R	26.9 MHz - 38.6 MHz (tunable)
quality factor Q	up to 200 (depends on f_R)
parasitic capacitance	34.7 pF - 16.8 pF (tunable)
inductivity of the coil	1.01 µH
Ohmic resistance	0.35 Ω

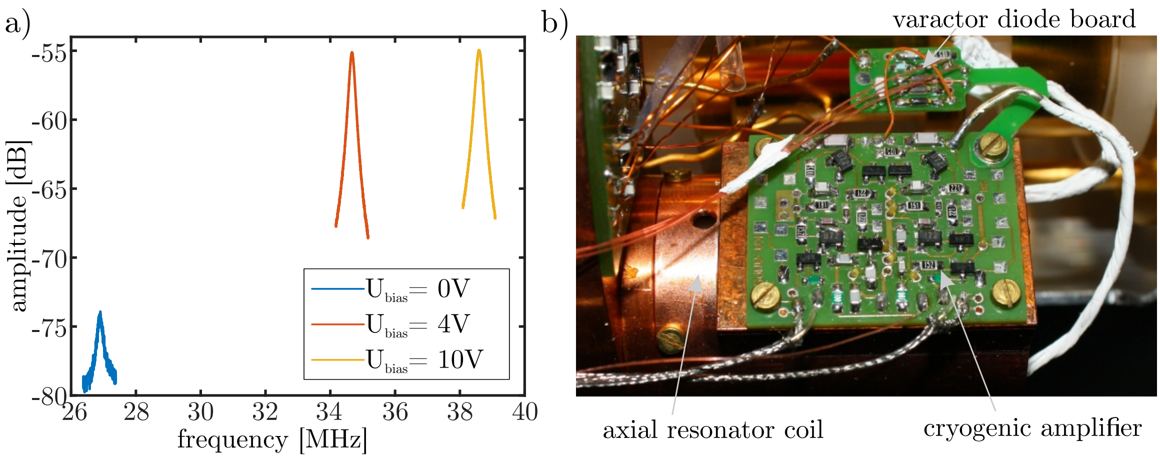

Figure 5.9.: a) Characteristic curves of the cyclotron resonator for different varactor-diode voltages. The resonance frequency can be tuned. b) Photo of the cyclotron cryogenic amplifier and the varactor diode board.

Figure 5.9 shows the frequency-tuning capability of the cyclotron resonantor and a photo of the amplifier. The resonance frequency can be tuned from 26.9 MHz to 38.6 MHz.
The resonantly amplified signal is further amplified by a two-stage amplifier containing a cryogenic and a room-temperature stage. The voltage amplification of both in combination is G_{radial}=100. The properties of the radial resonator are summarised in table 5.2.

The geometry function of a ring-electrode segment

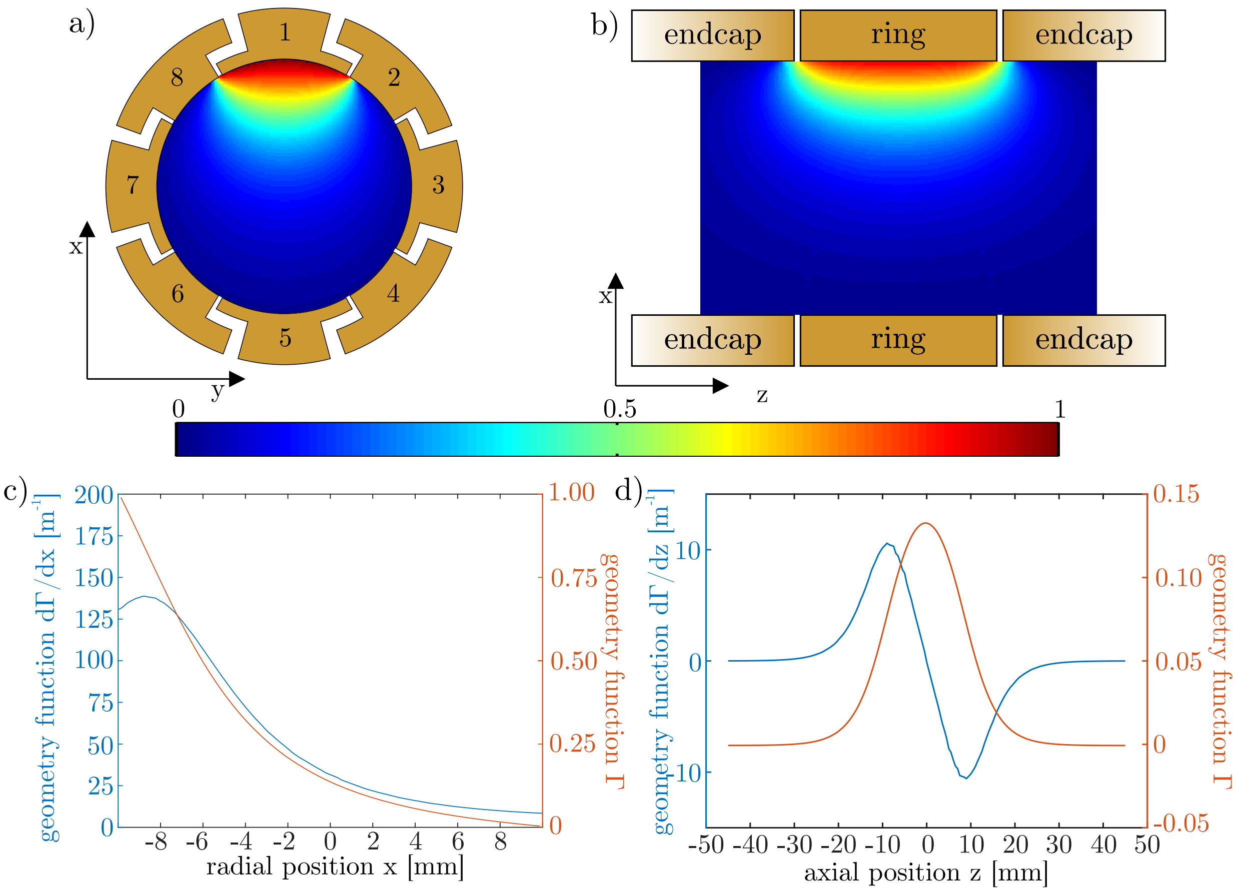

Figure 5.10.: Geometry function of a single large ring-electrode segment in the a) x-y-plane and b) in the x-z-plane. The cross sections for c)the radial direction and d) the axial direction show the absolue value of the geometry function and its respective first derivative.

Three of the large ring-electrode segments are used as pick-up electrodes for non-destructive ion detection or active-feedback cooling. The magnitude of the induced ion signal is directly connected with the geometry function of the segments according to equation 3.41. I have calculated the geometry function using the FEM-solver ComSol with the procedure described in section 3.5. The spatial dependence of the geometry function is illustrated in figure 5.10. The subfigures 5.10c-d show cross sections of the geometry function itself and its first derivative with respect to r and z. These values are important to calculate the induced voltage and current of the stored ions.

Minimum detectable number of ions

The most crucial parameters limiting the number of detectable ions is the input noise level e_{na} of the amplifier which competes with the amplitude of the pick-up signal. We have measured the electronic noise with a spectrum analyser using a resolution bandwith of 10 kHz. The amplifier was powered with a bias voltage of 6 V. Figure 5.11 shows the frequency-dependent input noise density of the cyclotron amplifier. The overall noise is measured here including noise of the detection electronics and in particular the thermal noise amplified by the resonator.

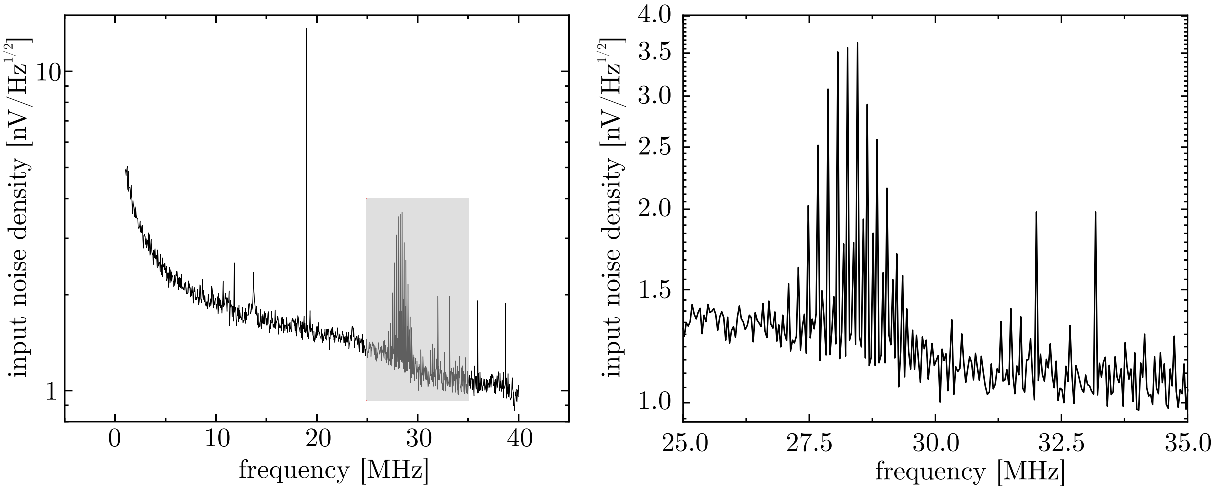

Figure 5.11.: Frequency-dependent input noise of the cyclotron amplifier. The magnified region is the frequency range in which the resonator can be tuned.

Depending on the frequency, the noise density varies between 1.1 nV/ $\sqrt{\text{Hz}}$ and 3.5 nV/ $\sqrt{\text{Hz}}$. I assume the signal to be distinguishable from noise, when it exceeds the noise level by a factor of 3. The signal amplitude induced by a stored ion is on the one hand connected to the ions' kinetic energy and on the other hand to the electrode geometry and the properties of the resonator. To estimate the signal height inside the resonator I have calculated the voltage inside the resonator coil, when it is driven by a single ion with charge q assuming only a radial motion. To this end, one has to solve the set of two differential equations

$$\frac{\mathrm{d}U_c}{\mathrm{d}t} = \frac{1}{C}\left(I(t) - I_L(t)\right) \tag{5.2}$$

$$\frac{\mathrm{d}I_L}{\mathrm{d}t} = \frac{1}{L}\left(U_C(t) - I_L(T)\cdot R_L\right). \tag{5.3}$$

The coefficients can be taken from figure 3.8 and the driving current is

$$I(t) = q \cdot \left(\frac{\mathrm{d}\Gamma\left(x(t), y(t)\right)}{\mathrm{d}x} \cdot v_x + \frac{\mathrm{d}\Gamma\left(x(t), y(t)\right)}{\mathrm{d}y} \cdot v_y \right). \tag{5.4}$$

The coordinates and the velocities are described by the motions given in equations 3.8, 3.9, 3.11 and 3.12 and the ion radius for a given radial energy can be deduced from 3.14. The magnetron radius is assumed to be zero. The magnitude of the derivative of the geometry function can be found in figure 5.10c. The resulting amplitudes from this calculation are shown in table 5.3 for Ar^{13+} and C^{5+} at different cyclotron energies.

Table 5.3.: Amplitudes of the induced signals in the cyclotron resonator by a single ion. The amplitude depends on the ions' energy.

radial ion energy	signal amplitude of Ar^{13+}	signal amplitude of C^{5+}
0.1 meV	0.27 nV	0.31 nV
1 meV	0.85 nV	0.99 nV
10 meV	2.7 nV	3.1 nV
100 meV	8.5 nV	9.9 nV
1 eV	27 nV	31 nV
10 eV	85 nV	99 nV

The noise level at a particular frequency f is the integral of the noise density over the resolution bandwidth (RBW) of the spectrum analyser around this very frequency:

$$V_{noise,rms} = \sqrt{\int_{RBW} e_{na}^2(f)\mathrm{d}f}. \tag{5.5}$$

Typically, the RBW for a radial detection is of the order of 1 Hz and so the induced signal amplitude at the resonator should be about 10 nV.
To be sensitive to a single stored particle, an ion energy of about 100 meV is necessary. If the stored ions have less energy, a higher number is required or the ions have to be excited resonantly to achieve higher kinetic energies.

5.4.3. The split endcap electrode

The endcap electrode on the ion side is split into two segments, where the upper one is used for ion excitation and the lower one for non-destructive ion detection via resonant pick-up of the axial oscillation of the ions. To this end, we have connected a resonant circuit to the lower half of the endcap electrode which is also responsible for resistive ion cooling.

The induced signal strength

The ion signal is picked up by one half of the endcap and drives the resonant circuit. The magnitude of the pick-up signal and the efficiency of the resistive ion cooling depends on the effective electrode distance (see equation 3.48). The spatial dependent electric field in this equation is calculated with ComSol. The resulting relation between ion position and the lokal effective electrode distance is illustrated in figure 5.12.

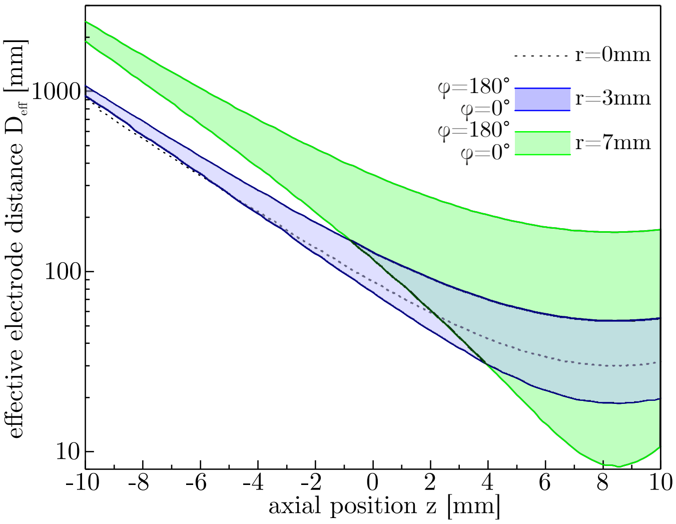

Figure 5.12.: Spatial dependence of the effective electrode distance D_{eff}. The electrode is on the right side. $\phi = 0°$ corresponds to the point which is closest to the electrode and $\phi = 180°$ is the point on the opposite side.

The lower the effective electrode distance, the higher is the induced signal. Obviously, high energetic ions with amplitudes higher than 10 mm will cause a non-linear voltage drop, as the magnitude of the induced signal varies by two orders of magnitude within one oscillation period. Additionally, the azimuthal dependence of the induced voltage becomes significant, when the ion is close to the endcap on the ion side. In the case of large radii there is also a significant azimuthal dependence. This influences the detection sensitivity of stored ions, and in particular the strong spatial dependence of D_{eff} may have a considerable influence on the efficiency of resistive cooling.

The axial resonant circuit

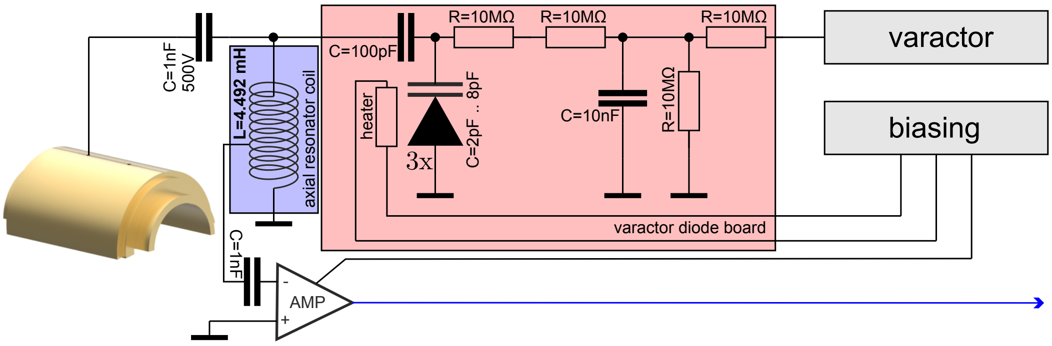

Figure 5.13.: The electric circuit of the axial non-destructive detection system consisting of the pick-up electrode, coil, varactor diode board and axial amplifier.

The HILITE Penning trap uses a normal-conducting tunable resonator which covers the frequency range from 351 kHz to 436 kHz. Like in the radial case, the tuning is enabled by a set of three varactor diodes. The electric circuit is depicted in figure 5.13. The signal is picked up in the half electrode on the left hand side and the capacitance of the electrode is added to the tunable capacity of the varactor diodes and in combination with the inductivity of the coil (L=4.492 mH) forms the resonant circuit.

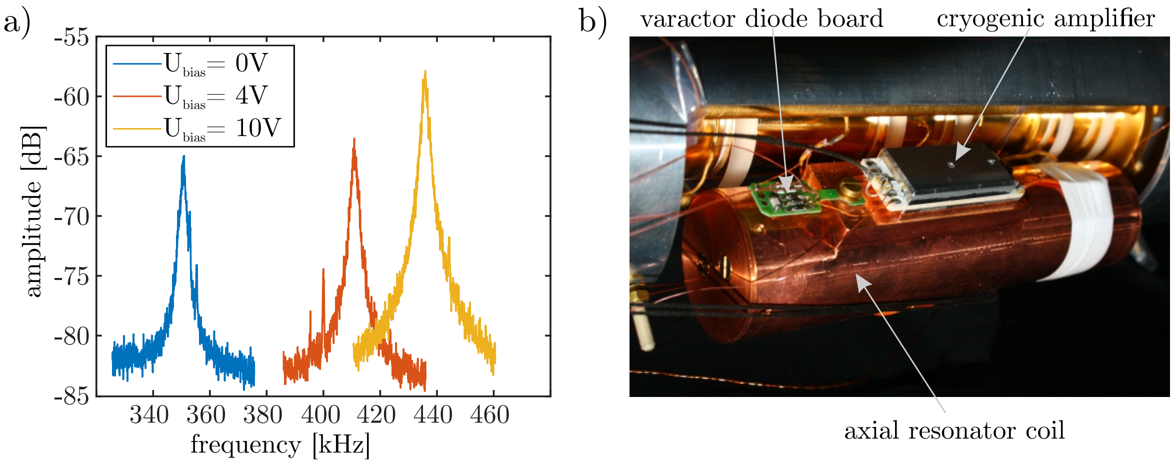

Figure 5.14.: a) Characteristic curves of the axial resonator for different varactor diode voltages. The resonance frequency can be tuned. b) Photo of the axial cryogenic amplifier and the varactor diode board.

The characteristic curves of the resonator are acquired at an operation temperature of 5.2 K. They are shown in figure 5.14 where the frequency dependence of the amplification for different varactor-diode voltages is depicted. From the 3 dB width the quality factor of the resonator is calculated.

Table 5.4.: Electonic properties of the axial resonator.

resonance frequency f_R	351 kHz - 436 kHz (tunable)
quality factor Q	up to 230 (depends on f_R)
parasitic capacitance	45.8 pF - 29.7 pF (tunable)
inductivity of the coil	4.492 mH
Ohmic resistance	120 Ω

Minimum detectable ion number

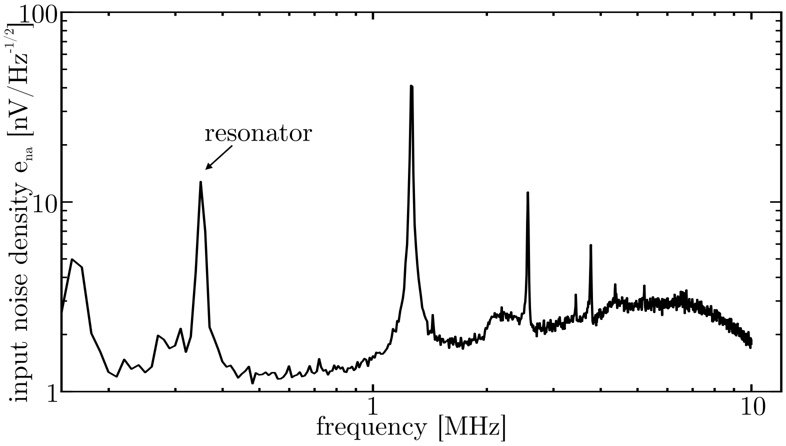

Figure 5.15.: Frequency-dependent input-noise density of the axial amplifier. The marked peak is amplified thermal noise caused by the axial resonator.

The signal of the axial resonator is amplified by a low-noise amplifier optimised for frequencies between 1 kHz and 4 MHz. The input noise density in this region is roughly 1 nV/ $\sqrt{\text{Hz}}$ as shown in figure 5.15. The frequency band covered by the axial resonator has an input noise density of roughly 10 nV/ $\sqrt{\text{Hz}}$. To determine the prospective sensitivity of the resonator I have calculated the amplitude of the signal inside the resonator coil excited by the axial motion of a single ion inside the trap. The calculation is very similar to the method described in section 5.4.2, despite that the z-components are considered. Table 5.5 shows the amplitudes of the induced signals caused by ions with different axial energies. Assuming again a RBW of 100 Hz, the minimum amplitude has to be about 300 nV. With our setup this is fulfilled for a single ion with an energy of about 5 meV.

Table 5.5.: Amplitudes of the signals induced in the axial resonator by a single ion. The amplitude dedends on the ions' amplitude.

axial ion energy	signal amplitude of Ar^{13+}	signal amplitude of C^{5+}
0.1 meV	65.5 nV	46 nV
1 meV	207 nV	145 nV
10 meV	655 nV	460 nV
100 meV	2.08 µV	1.46 µV
1 eV	6.58 µV	4.65 µV

5.4.4. The full endcap electrode

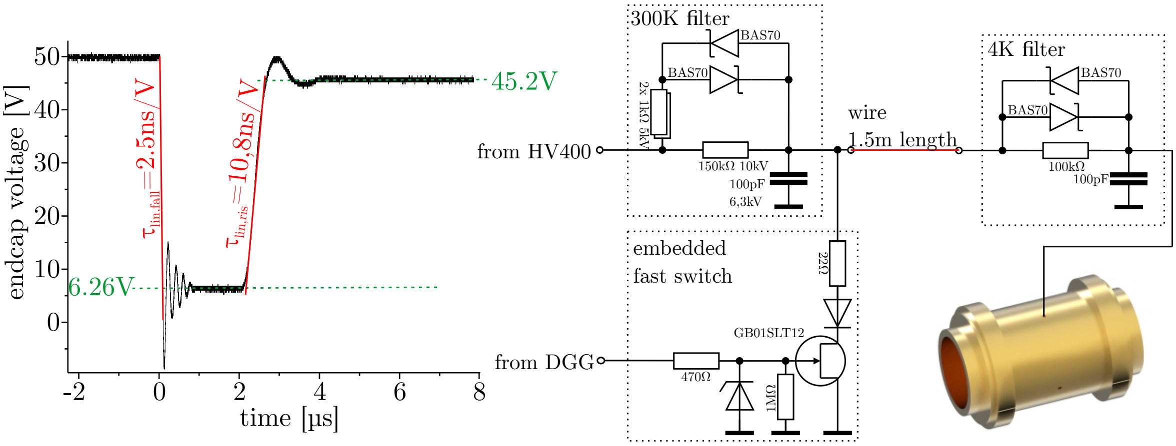

Figure 5.16.: Switching behaviour of the full endcap electrode. The graph shows the discharge of the endcap electrode with a fast switch. The electric circuit contains the two-stage electrode filter and the fast switch.

Fast switching of electrodes opens up a lot of possibilities concerning ion capture [73] and ion selection. As the endcap electrode is located close to the magnetic field maximum, where the ions are compressed well in the radial direction, ion deceleration is very efficient there. Also ion selection is very effective, as excited unwanted ions can be ejected efficiently after resonant axial excitation [74]. To this end, we have applied a MOSFET-based switch to the electrode which, if enabled, pulls the endcap electrode to ground. The switch is embedded in the 300K filter box and can be enabled with a +5V pulse. Figure 5.16 shows the electronic circuit of the fast switch. The maximum discharge current is mainly limited by the 22 Ω resistor located between drain of the npn-transistor and the filter circuit. The cable length outside the vacuum is only about half a metre and about one metre inside the vacuum to allow a low switching time.

To test the switching behaviour of the embedded switch together with the full endcap electrode, we have sent a TTL-signal with a pulse width of 2 µs by the delay-gate generator (DGG). The electrode initially has been set to a voltage of 50 V. Figure 5.16 shows the switching behaviour of the full endcap electrode. The voltage drops down to −8.35 V with a slew rate of 2.5 ns V^{-1} and oscillates for 1 µs before settling at a voltage of 6.26 V. The rise time up to 45.2 V is 430 ns and hence four times longer than the falling time, but for ion capture issues still sufficiently short. For comparision, ions with a kinetic energy of 15 eV/q travel about 15 mm in this time which is roughly the length of the ring electrode. At this point, one has to point out that the embedded fast switch is designed only to switch fast from positive potential to ground. The fast charging of the electrode is caused by a not completely discharged capacitor located in the high-voltage power supply HV400.

5.5. Pulsed drift tube for ion deceleration

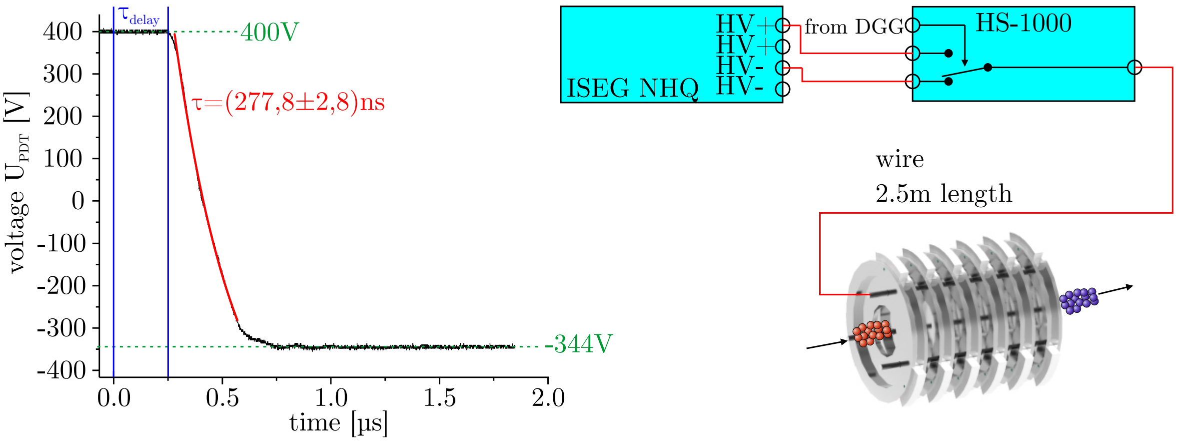

Figure 5.17.: Switching time and connection of the pulsed drift tube. The fast switching is provided by a commercially available low-noise fast switch. The switching signal is controlled by a delay-gate generator.

The HILITE Penning trap is loaded by an EBIT which delivers ions with kinetic energies of around 1 keV/q. We use the technique of *dynamic ion capture* to capture and trap the ions efficiently [73]. In our setup, we use the first set of baffles in the direction of the ions (see figure 5.4a) as pulsed drift tube to decelerate the ions. The efficiency of the dynamic ion-capture process is highly dependent on the switching parameters of this electrode. It is switched with the commercially available low-noise fast switch 'HS-1000' by

Stahl Electronics which is capable of switching a voltage difference of up to 1000 V. The switching TTL-signal is sent by a delay-gate generator which allows to set the point in time with steps of 10 ns. The actual timing precission is 1 ns. The switching behaviour is shown in figure 5.17. The two inputs of the voltage switch are set to 400 V and −400 V, respectively. Depending on whether the switching signal is 5 V or 0 V, the output voltage of the switch is the higher or the lower value, respectively. The measured falling time of the voltage at the pulsed drift tube is 277 ns. This is approximately half the time a C^{5+} ion with a kinetic energy of 500 eV/q needs to pass the pulsed drift tube which is 477 ns and is hence assumed to be sufficiently short. Although the lower voltage has been set to −400 V the voltage has fallen only to −344 V which has to be taken into account and can be compensated easily by proper choice of the low pulsed-drift-tube voltage.

5.6. Capture electrode

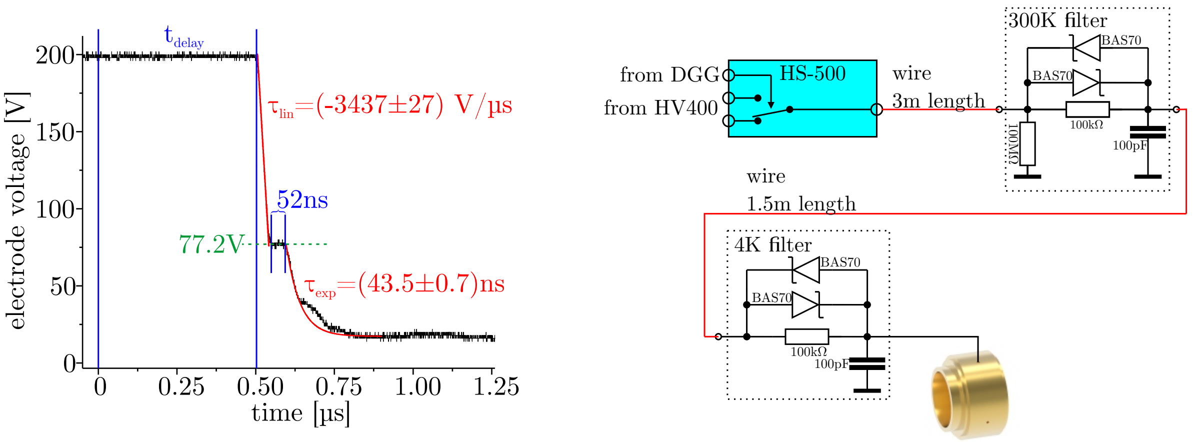

Figure 5.18.: Voltage evolution at the capture electrode and the electronic circuit. In parallel to the low-pass filters, Schottky diodes are applied to bypass the filters for high voltage differences.

The HILITE Penning trap is equipped with two dedicated electrodes which provide the dynamic ion capture. The one on the laser side can be set to any voltage between 400 V and −400 V limited by the power supply. The capture electrode on the ion side is connected to a fast switch 'HS-500' by Stahl Electronics. The switching behaviour of the capture electrode is shown in figure 5.18. The electronic circuit includes the fast switch and the two-stage filter. They filter low noise signals with frequencies over 10 kHz, but provide fast switching of voltage differences down to 2 V. This is accomplished by the parallel Schottky diodes BAS70 which have a threshold voltage of about 500 mV. The step-like decrease is due to the combination of several devices and filter systems and still allows an efficient ion capture capability. The overall falling time is about 250 ns which is close to the time a C^{5+} ion with a kinetic energy of 100 eV/q needs to pass the electrode. This is a typical kinetic energy for decelerated ions which will be presented in the next chapter.

5.7. Single-pass charge counter

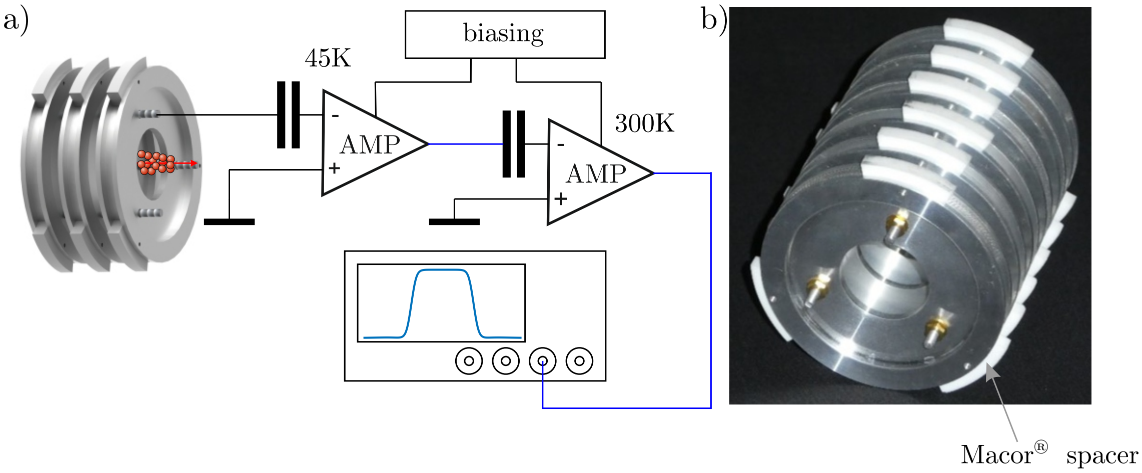

Figure 5.19.: a)Working principle of the single-pass charge counter. The induced signal by the passing ions is amplified twice and recorded by an oscilloscope. b)Baffle structured charge-counter electrode. The Macor spacer conduct the heat to the inner shield while they insulate the device electrically.

For single-pass non-destructive charge counting we use three and seven segments of the baffle structures on the ion side and the laser side, respectively. This allows the detection of ion bunches which are flying into or out of the trap and their characterisation with respect to number, kinetic energy and bunch length. The signal is picked up via mirror charges induced by the passing ions in the baffle structure. The magnitude of the induced charge by an ion is related to the geometry function following equation 3.41. The induced charge is amplified twice, by a cryogenic amplifier at 45 K and by a room-temperature amplifier, as shown in figure 5.19a. The baffles have an inner diameter of 28 mm and are electrically insulated from the inner shield by ceramic spacers which are also thermally conductive (see figure 5.19) in order to cool the baffles down to the shield temperature.

5.7.1. Geometry function of the charge counter

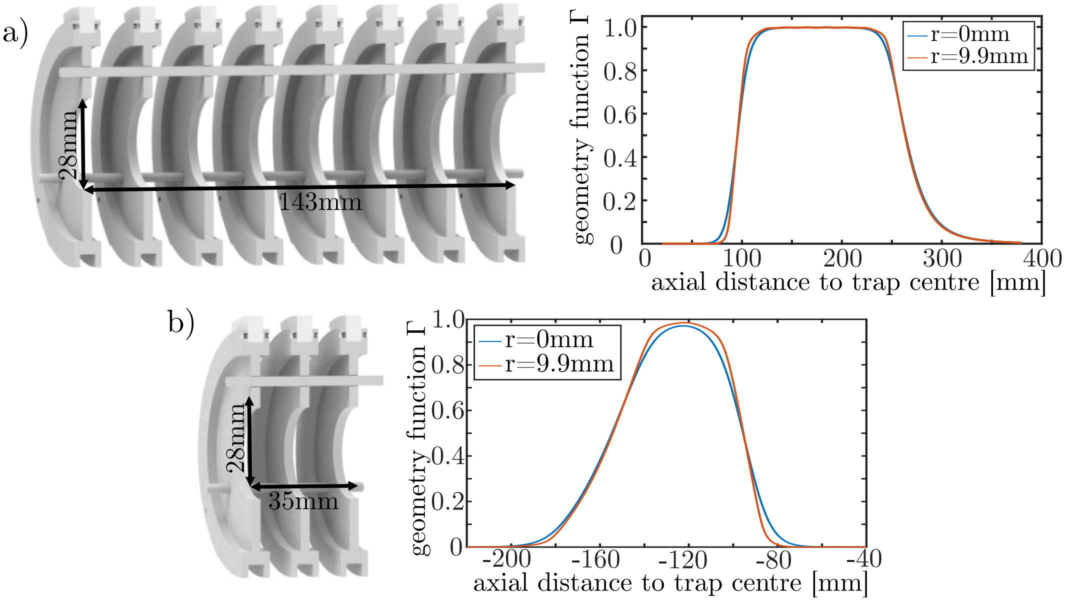

Figure 5.20.: Dimensions and geometry function of the charge counter on a) the laser side and on b) the ion side.

To calculate the geometry functions of the charge counters we have performed a simulation with the FEM-solver ComSol Multiphysics [71] following the procedure introduced in section 3.5. Figures 5.20a and 5.20b show the cross sections along the z-axis of the charge counters on the laser side and on the ion side, respectively. The geometry functions are given at two different distances r to the z-axis. For both devices there is only a negligible influence of the radial position of the ion. Consequently, the radial position will influence the result only slightly. The axial shapes of the cross sections of the charge counters differ from each other. While the charge counter on the ion side has a peak structure with a maximum value of about 0.93, the charge counter on the laser side has a plateau with a constant value of nearly unity over a length of approximately 120 mm. As we have used only the charge counter on the laser side to determine the ion bunch properties, I will focus exclusively on this one in the following section, but will give the properties of the charge counter on the ion side in the summary at the end.

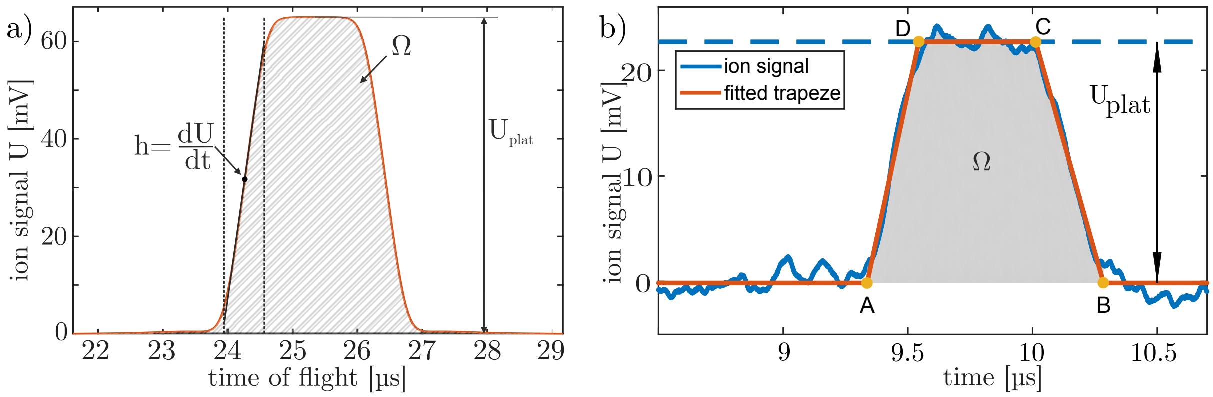

Figure 5.21.: a)Characteristic properties of a charge counter signal. b) To calculate the respective parameters, a trapeze-shaped function with parameters A,B,C,D, U_{base} and U_{plat} is fitted to the acquired signal. The measurement uncertainties are related to the uncertainties of the coefficients [75].

5.7.2. Determination of the ion bunch properties

The single-pass charge counter is capable of determining the number of passing ions in an ion bunch on a shot-to-shot basis. If the ion charge state and the ion velocity are known well, the absolute ion number can be deduced from the area Ω below the signal curve in figure 5.21a following [76]:

$$N = \frac{v}{q \cdot L \cdot S} \underbrace{\int U(t)\mathrm{d}t}_{=\Omega}, \tag{5.6}$$

where $L = \int_{-\infty}^{\infty} \Gamma(z)$ is the so-called *characteristic length* and S is the *characteristic sensitivity* of the device defined as

$$S = \frac{\alpha}{C}. \tag{5.7}$$

Here, α is the combined amplification of both amplifiers and C is the combined capacitance of the pick-up electrode, the input capacitance of the cryogenic amplifier, and of the connection cable. The knowledge of the sensitivity S of the entire charge-counter device enables even the measurement of absolute ion numbers. The sensitivity has to be measured for each device individually and will be described in the following section.

For ion bunches with an axial extent less than the plateau length of the charge-counter geometry function, even the bunch kinetic energy and the bunch length can be determined by evaluating one single-pass ion signal only. In this case, the geometry function $\Gamma(r_i, z_i)$ of all ions is unity simultaneously and the ion signal itself has a pronounced plateau. Figure 5.21b shows the acquired signal of a single ion bunch of about 6,000 Ar^{13+} ions with an axial extent of less than 120 mm. All signals of sufficiently short ion bunches have this typical shape in common - a linear rising edge, a plateau of constant signal and a linear falling edge. That is why we have chosen to fit a trapeze-shaped function to the signal. Here, the corners A and B as well as C and D are on the same level. The voltage difference between both levels is the so-called plateau voltage U_{plat}.

From the plateau voltage U_{plat} the absolute number of ions can be deduced with [77]:

$$N = \frac{U_{plat}}{S \cdot q \cdot e}. \tag{5.8}$$

Though this method is highly demanding with respect to the ion bunch conditions, it has the big advantage that the velocity needs not to be known as in the case desribed by equation 5.6. Combining equations 5.6 and 5.8 one gets a formula to calculate the kinetic energy of the ions [77]:

$$E_{kin} = \frac{1}{2} \cdot m_{ion} \cdot L^2 \frac{U_{plat}^2}{\Omega^2}. \tag{5.9}$$

This equation in particular is independent from the sensitivity of the detection system.

The plateau length and hence the slope of the rising edge are connected directly with the length of the ion bunch. As described above, the plateau will only be established when the ion bunch is shorter than the plateau of the geometry function of the pick-up electrode. This geometry factor of the setup is the upper limit for the bunch-length determination. In the case of the charge counter on the laser side, the upper limit is about 150 mm. For shorter bunches, the slope of the leading edge h is a measure for the bunch length as depicted in figure 5.21a. Assuming an ion bunch with uniformly distributed ions within the bunch length l_b, the slope of the ion signal is:

$$\frac{\mathrm{d}U}{\mathrm{d}t} = \frac{N \cdot S \cdot q \cdot e \cdot v}{l_b} \cdot \left(\Gamma(z(t) + l_b/2) - \Gamma(z(t) - l_b/2)\right). \tag{5.10}$$

In the region where the geometry function is between 0.1 and 0.9, marked by the dashed vertical lines in figure 5.21, the slope is nearly constant. If the bunch is shorter than the length of the rising edge, the slope is independent from the bunch length. In this case one can only give an upper limit of the bunch length. If the bunch is longer, the leading part of the bunch has a geometry function value of 1 und the last part has 0. So from equation

5.10 one gets for the bunch length using $h = \mathrm{d}U/\mathrm{d}t$ with equations 5.6 and 5.8 [77]

$$l_b = \frac{U_{plat}^2 \cdot L}{\Omega \cdot h}. \tag{5.11}$$

5.7.3. Measurement of the sensitivity

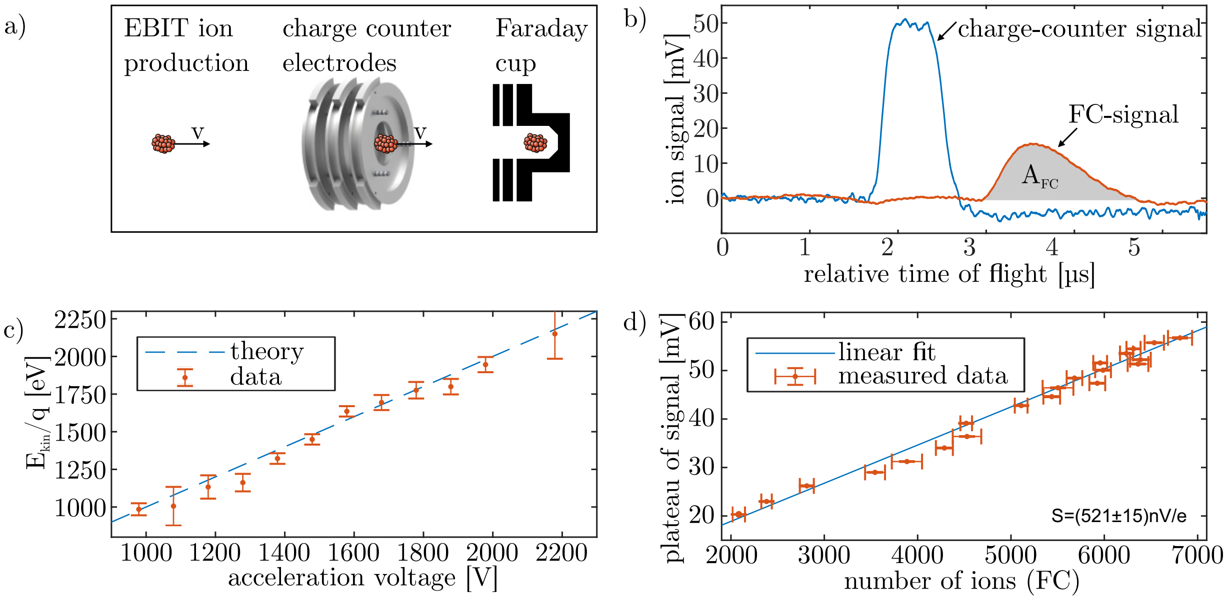

Figure 5.22.: a)The ions from an ion source are detected with the charge counter on the laser side non-destructively and destructively with a Faraday cup as reference. b)Example signals of both detection devices. c)Comparision of the kinetic energy with the respective acceleration voltage. The dashed line is the expected relation. d)Calibration curve to determine the characteristic sensitivity of the charge counter.[75]

To measure absolute ion numbers, the sensitivity as characteristic parameter of the measurement device has to be known. Therefore, we have performed a calibration measurement using a Faraday cup (FC) as a reference (see figure 5.22a). When an ion hits the Faraday cup, it transfers its charge which subsequently causes a current. The current is amplified by a current amplifier with a calibrated amplification factor of $\alpha_{FC} = 1 \times 10^6\,\mathrm{V\,A^{-1}}$. The ion signals at the Faraday cup and at the charge counter are recorded by an oscilloscope with a temporal resolution of 2.5 GSa/s. Figure 5.22b shows a typical FC-signal and a charge-counter signal. The number of particles detected by the Faraday cup is proportional to the area below the signal curve A_{FC} as follows:

$$N = \frac{A_{FC}}{q\alpha_{FC}}. \tag{5.12}$$

The ions used for the calibration measurement produced inside the EBIT are charge-state and velocity selected by a Wien filter. The EBIT is run in the bunch mode and delivers isolated ion bunches. The ion number can be controlled by the adjustment of the EBIT breeding time. The ion signals for different breeding times and so different ion numbers have been acquired and evaluated using expressions 5.12 and 5.8. From the slope of the calibration curve in figure 5.22c, the sensitivity of the charge counter on the laser side can be calculated in terms of the elementary charge:

$$S_{CCL} = (521 \pm 15)\mathrm{nV/e}. \tag{5.13}$$

At room temperature, the capacitance of the charge counter pick-up electrode has been measured to be $C = (116.1 \pm 0.1)\,\mathrm{pF}$ [75]. We expect the capacitance to vary only slightly with decreasing temperature and from the determined sensitivity and the measured capacitance, the actual amplification factor can be determined with equation 5.7 to:

$$\alpha_{CCL} = (559 \pm 21)\mathrm{nV}. \tag{5.14}$$

For the determination of the ion bunch kinetic energy or velocity, a calibration measurement is not necessary. Nevertheless, we have performed a verification measurement here. Therefore, we have tuned the acceleration voltage between 980 V and 2180 V. We have recorded the ion signals with the oscilloscope and have evaluated the signals according to equation 5.9. Figure 5.22d shows the measured kinetic energy with respect to the applied acceleration voltage. We expect the kinetic energy per charge to be equal to the acceleration voltage which is denoted by the dashed blue line. The measurement values match the theory well within the measurement uncertainties. So this measurement device is a reliable tool to measure the kinetic energy of passing ions. The parameters needed for the determination of the bunch properties of both charge counters are summarised in table 5.6.

5.7.4. Minimum number of detectable ions

To estimate the minimum number of detectable ions, we have determined the noise density at the amplifier input to compare it with the amplitude of the induced voltage. Therefore,

Table 5.6.: Properties of the charge counters. The values are taken from [75].

property	value CCL	value CCI
sensitivity S	$(526 \pm 20)\,\mathrm{nV/e}$	$(1460 \pm 20)\,\mathrm{nV/e}$
amplification	-559 ± 28	-477 ± 32
capacitance	$(116.1 \pm 1.1)\,\mathrm{pF}$	$(52.4 \pm 1.1)\,\mathrm{pF}$
characteristic length	171.6 mm	59.7 mm

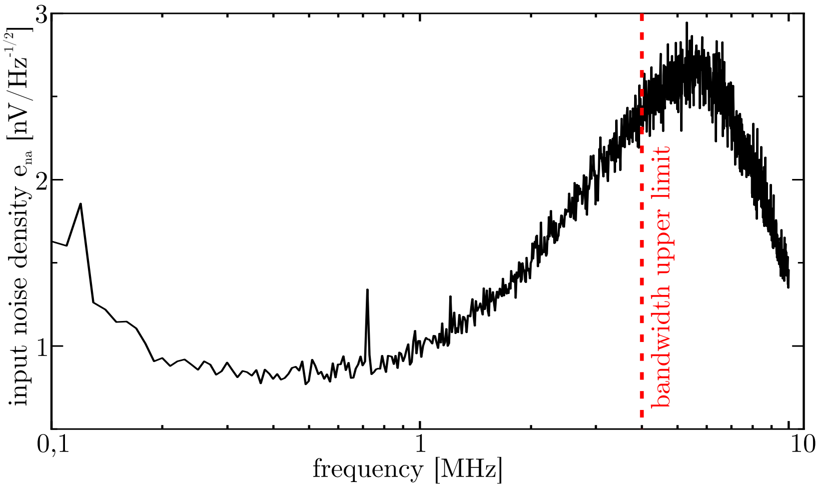

Figure 5.23.: Input-noise density of the charge-counter amplifier. The dashed red line is the upper frequency limit of its bandwidth. The lower limit is the y-axis.

we have measured the noise amplitude at the amplifier output and calculated the input noise density $e_{na}(f)$. The input noise density of the amplifier is shown in figure 5.23. The noise amplitude of a signal acquired in the time domain is then

$$V_{noise,rms} = \sqrt{\int_{100\,\mathrm{kHz}}^{4\,\mathrm{MHz}} e_{na}^2(f)\mathrm{d}f}. \tag{5.15}$$

The integration limits are the upper and the lower limit of the bandwidth shown in figure 5.23 which yields to a noise amplitude of

$$V_{noise} = 3.28\,\mathrm{\mu V}. \tag{5.16}$$

Combining the determined sensitivity with the measured noise and the determined amplification factor, the minimum number of measurable charges is about 6400 which corresponds to approximatly 490 Ar^{13+} ions. In this case, the induced signal is $3 \cdot V_{noise}$. An amplifier with a reduced input noise density is currently in development.

6. Ions in the trap: methods and measurements

To determine absolute cross sections of non-linear laser ionisation, the ion target has to be prepared carefully. The ions have to be captured, stored inside the trap centre, and the species and number of ions have to be determined. Additionally, the ions have to be cooled in order to achieve a strongly-coupled ion ensemble and a compact ion cloud. In this chapter I will describe the capture of ions and the investigation of the stored ion species. I will present the storage time of the captured ions and the temporal evolution of the trap content. The measurements are part of the ion-trap commissioning and were initially performed with Ar^{13+} and later with C^{2+}. The first was chosen because of its large number of possible charge states and the latter because carbon will be the ion to be investigated in our upcoming beamtime.

6.1. Loading the trap from external source

The principle of dynamic ion capture is based on the idea to produce ions in an external source with subsequent deceleration and storage in the trap [73]. In our case, the ions are emitted in bunches of several thousands of ions which are focussed by an Einzel lens and guided into the trapping region inside the magnet's bore. The ions are captured in-flight to end up between the endcap electrodes of the ion trap. The sequence of trap electrode switching is illustrated in figure 6.1. The individual steps of the capture procedure are described in the following section.

6.1.1. Ion decelaration and ion bucketting

The ions emitted from the EBIT have a kinetic energy of the order of $1\,\mathrm{keV/q}$. For ion capture using the trap electrodes it is necessary to reduce the energy below $400\,\mathrm{eV/q}$. Even lower kinetic energies reduces the need for subsequent ion cooling.

To measure the deceleration efficiency we have determined the kinetic energy of the decelerated ions. To this end, we have used the charge counter on the laser side with the

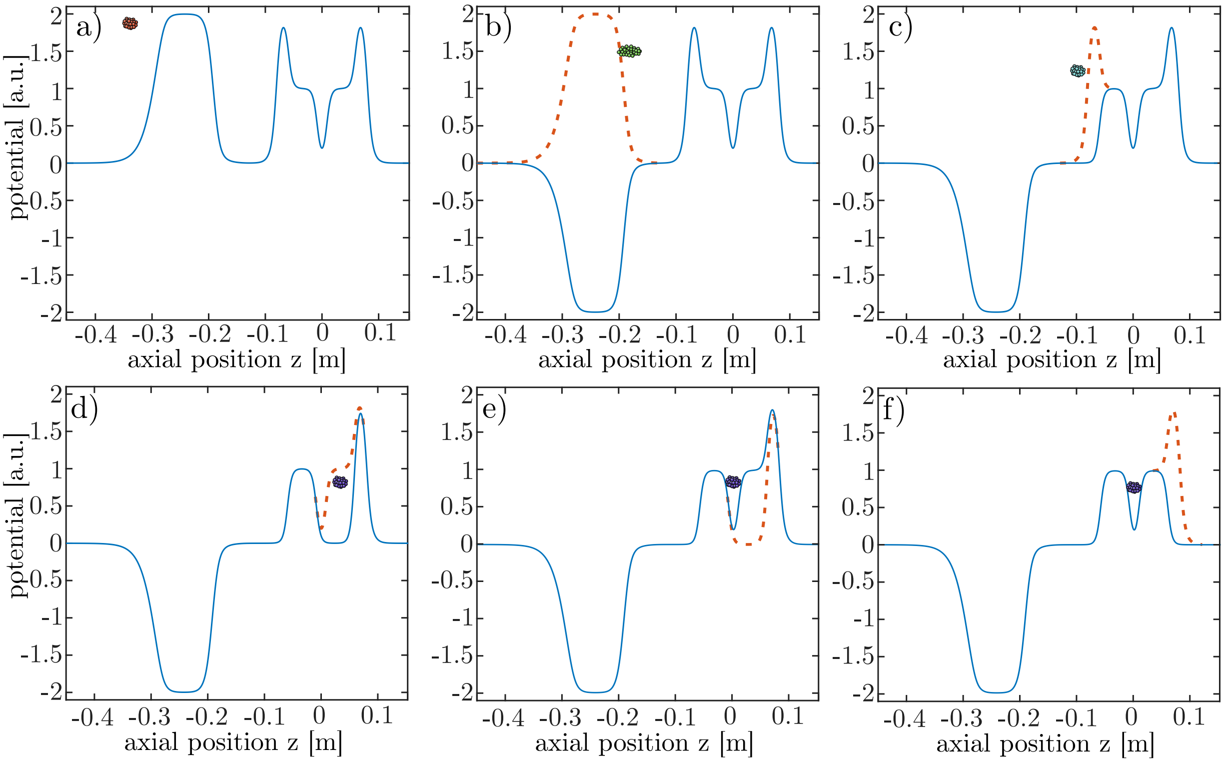

Figure 6.1.: Electrode timing for dynamic ion capture: a) incoming ions towards positively charged pulsed drift tube, b) decelerated ions retracted by negatively charged pulsed drift tube c) ion bucketting with positively charged capture electrode d) ion deceleration by fast off-switching of the endcap electrode close to trap centre e) fast on-switching of the same endcap electrode for ion trapping f) captured ions between endcap electrodes.

evaluation procedure descibed in section 5.7.2 together with equation 5.9. The ions ejected from the EBIT travel along the trap axis in bunches towards the trap (figure 6.1a). Figure 6.2a shows the measured ion signal of an undecelerated bunch of about 3400 Ar^{13+} ions with a kinetic energy of 979 eV/q. The main deceleration takes place inside the pulsed drift tube which was switched from 400 V to -400 V (figure 6.1b). The voltage drop as well as the point in time t_{PDT} are crucial for efficient ion deceleration. For Ar^{13+} a switching time t_{PDT} of 7.36 µs after ion ejection was found to be most efficient with respect to deceleration. In this configuration, about 75% of the ions have passed the pulsed drift tube while only a small portion was lost. Mainly ions are lost on trajectories off the axis where the field properties of the magnet and the pulsed drift tube are unpropicious. Figure 6.2b shows the ion signal of a decelerated ion bunch. Here, the ion bunch is too long to create a well-pronounced plateau in the signal and cannot be characterised concerning number and energy directly from the charge-counter ion signal. From the time of flight between charge counter and MCP the kinetic energy can determined to be about 200 eV/q. The increase of the axial extent of the ion bunch is an intrinsic effect of the deceleration procedure and reduces the capture efficiency significantly. To reduce the axial extent of the decelerated ion bunch, we use the first trap electrode (capture-electrode ion) for ion bucketting.

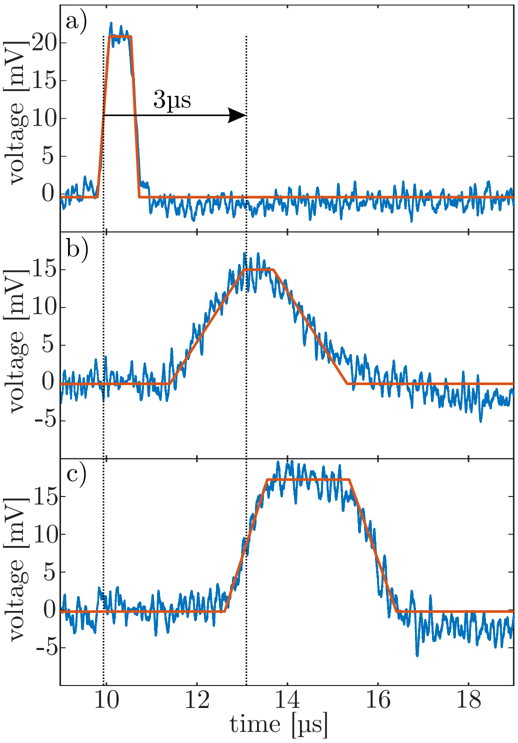

Figure 6.2.: Charge-counter signals (blue) of a) undecelerated ions, b) decelerated ions and c) decelerated and rebunched ions. The orange curves are trapeze functions fitted to the data. From them, the ion bunch properties are determined according to the procedure described in section 5.7.2.

Initially it is set to a voltage U_{cei} and switched to zero after a time t_{cei} (figure 6.1c). The point in time t_{cei} is well chosen, such that the leading and hence faster ions of the ion bunch are affected by the electrode potential resulting in a deceleration, while the following slower ions are affected less. The effect of ion bucketting using the capture electrode is shown in figure 6.2c. Here, the electrode voltage was 95 V and $t_{cei} = 9.75\,\mu s$. The plateau is again well-pronounced and the leading edge is again shifted to longer times. Using equation 5.11 the axial length of the bunch after bucketting is determined to be below the lower detection limit of 50 mm. The kinetic energy of the ion bunch is reduced to (87 ± 5) eV/q.

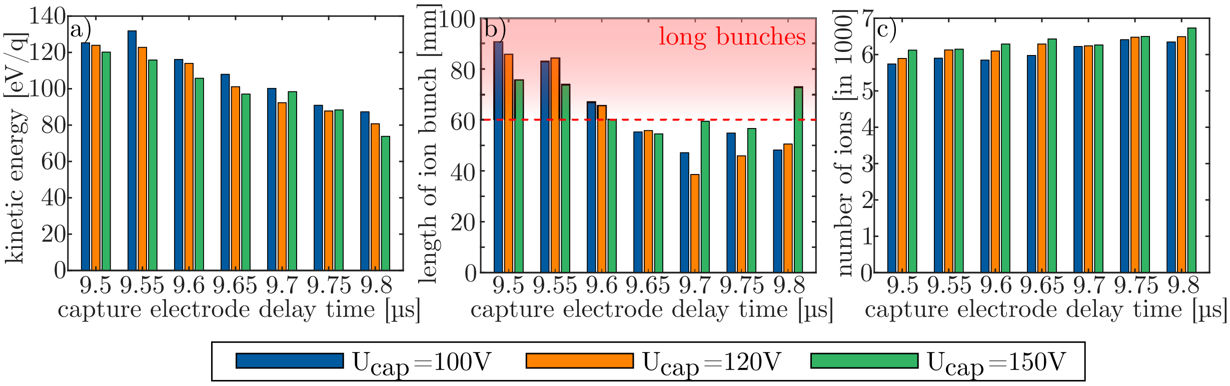

Figure 6.3.: Influence of the capture electrode potential and switching time on the bunch properties. The later the electrode is switched the lower is the kinetic energy. But the shortest bunches are measured at 9.70 µs and 9.75 µs.

To investigate the influence of the capture electrode voltage and the timing of the switching in detail, we have scanned the time in steps of 500 ns and the voltage from 100 V to 150 V. The voltages and switching point of the pulsed drift tube were ±400 V and $t_{PDT} = 7.32\,\mu s$, respectively. Figures 6.3a and 6.3b show the dependence of the bunch length and the kinetic energy. While the kinetic energy decreases monotonically with increasing point in time when the electrode was switched, the bunch length has a minimum at $t_{cei} = 9.70\,\mu s$ and increases again, when the electrode is switched later. It is recommended to keep the bunch length below 60 mm, because this is double the length of the plateau of the potential of the endcap electrode. The number of ions after deceleration does not vary significantly for different parameters in contrast to bunch length and ion energy. That is why it is no decision criterium for the capture parameter selection.

6.1.2. Ion capture and ion trapping

The ion trapping takes place between the endcap electrodes. In our case to store the ions between the endcap electrodes, we perform an in-trap deceleration of the ion bunch with subsequent ion capture. The ions are decelerated und compressed by use of the procedure described in the subsection before. Both endcaps are set to a voltage U_0 and the capture electrode on the laser side to $U_{cel} \approx 2.5 \cdot U_0$ (figure 6.1d). The ions pass the potential hills of the endcaps barely. At the time $t_{ec,delay}$, when the ions are located in the potential plateau of the endcap electrode, we switch the potential fast towards zero (figure 6.1d). The decelated ions proceed flying towards the capture electrode on the laser side and are reflected. Due to the reduced kinetic energy, the ions do not overcome the barrier of the endcap electrode on the ion side anymore. After a time $t_{ec,down}$ the voltage of the endcap electrode on the laser side is switched back to the trapping voltage (figure 6.1e). The ions now are stored between both endcap electrodes which both are set to a potential U_0. In the end, the voltage at the capture electrodes is set to zero (figure 6.1f). Here, the crucial parameters are the trapping voltage U_0 and the switching times $t_{ec,delay}$ and $t_{ec,down}$.

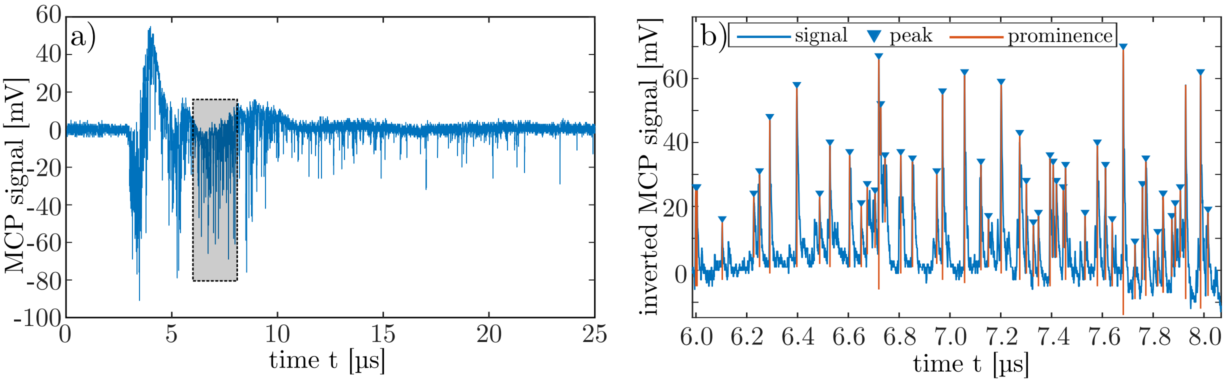

Figure 6.4.: Deducing the relative number of ions from acquired MCP signal. The peaks are found with the MatLab 'findpeak' function. The number of ions is assumed to be the sum of the peaks' prominences.

To test this ion-capture procedure in the first place, we have captured ions according to the sequence described above, have stored them for several hundreds of milliseconds, and have ejected them towards the time-sensitive MCP detector by switching the endcap electrode on the laser side fast down to zero. A typical ion signal of the emitted ions is depicted in figure 6.4. The ions' times of flight are widely spread over about 100 µs. This is caused by the limited acceleration by the trap in the moment of ion release. To estimate the relative number of ions we have counted the number of peaks with a MatLab embedded peak-search function only taking peaks into account with a prominence of at least 14 mV.

To verify the effectiveness of the ion-capture procedure and to optimise the trapping parameters, we have scanned a wide range of three different parameters with decelerated and re-bunched Ar^{13+} ions from our ion source:

- endcap voltage U_{ec}: 45 V to 70 V
- endcap delay time $t_{ec,delay}$: 11 µs to 15 µs
- endcap downtime $t_{ec,down}$: 0.5 µs to 4.0 µs.

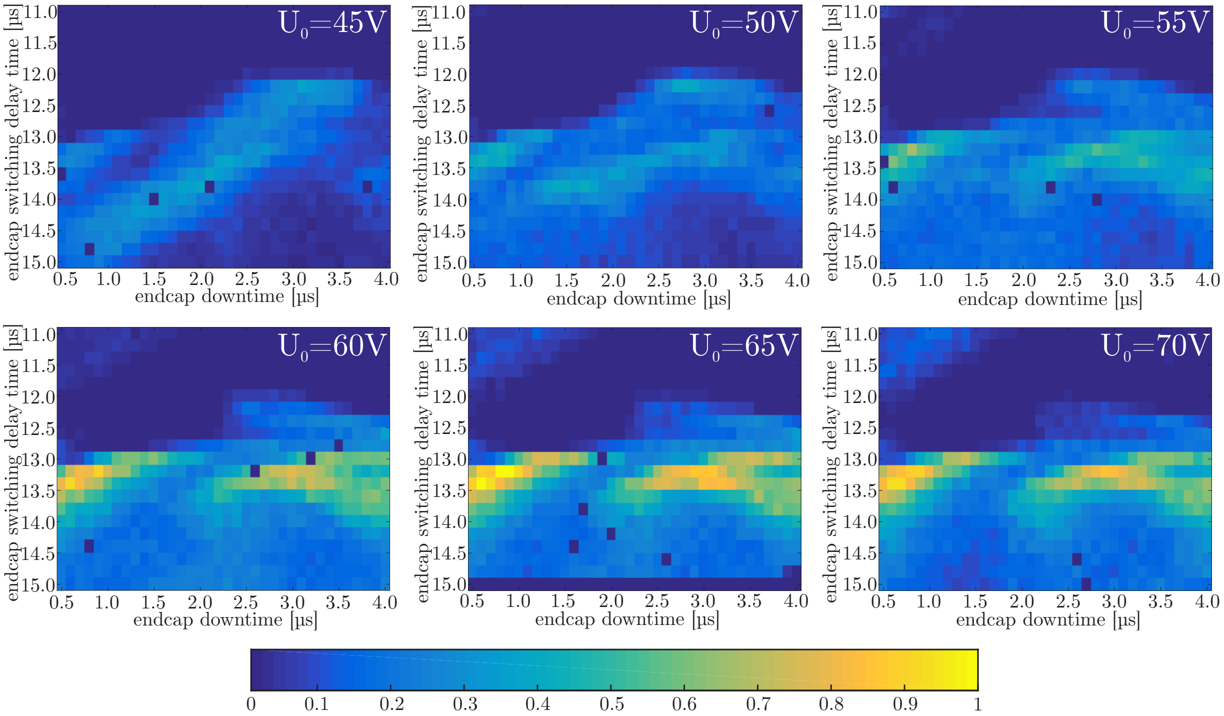

Figure 6.5.: Number of captured ions. The color code represents only a relative number of ions normalised to the overall maximum. The determination of an absolute number of ions was not possible up to this time.

The decelerated and captured ion bunches have had a kinetic energy of about 90 eV and the bunch length has been below the detection limit of 50 mm. The relative number of captured ions is shown in figure 6.5. The values are normalised to the maximum of all measurements. Most ions have been captured for trap potentials between 60 V and 70 V, delay times between 13 µs and 13.5 µs and a downtime between 0.8 µs and 1.0 µs. The occurences between 2.0 µs and 3.5 µs can be interpreted as ions which oscillate once between the endcap and the capture electrode before being captured. So the timing of the endcap electrode is sensitive in the 100 ns regime. This measurement has proven clearly the functionality of the introduced capture procedure. For other ion species individual deceleration and capture parameters have to be found. The determination of the absolute ion number needs further investigation and will be performed in future calibration measurements.

6.2. Characterising the ion content of the trap

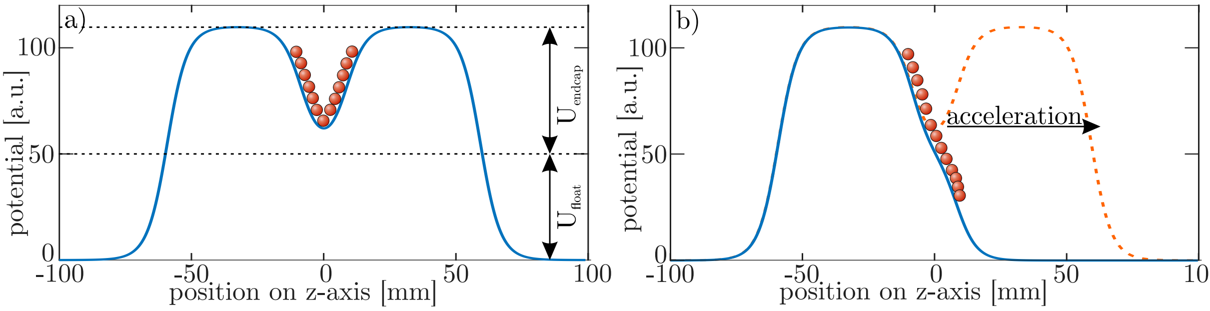

Figure 6.6.: Illustration of the ion acceleration for a trap potential of 60 V and an offset of 50 V. a) The ions are stored in the trap. The voltages of the electrodes have a common offset to increase the potential energy of the ions. b) One endcap electrode is switched to ground and all ions are accelerated towards the MCP.

We want to characterise the ion ensemble inside the ion trap more in detail with regard to the ion species. The ions are separated in the time of flight due to their individual charge-to-mass ratios, when accelerated by a sufficiently high electric field towards the MCP. To this end, we have increased the potential of all trapping electrodes (endcaps and ring) in parallel as depicted in figure 6.6a. This is done by the application of a voltage U_{float} to the floating ground input of the high-voltage power supply 'HV-400'. The simultaneous increase of all potentials does not affect the stored ions as there is no change of the electric field. To characterise the ions, the endcap electrode again is switched fast to ground. Now, the ions see a high potential gradient and are hence accelerated all towards the MCP as illustrated in figure 6.6b. As the MCP itself is held on a potential of $-2100\,\mathrm{V}$, the ions are accelerated further there.

To find the dependence of the time of flight of the ions on the charge-to-mass ratio, I use the simple assumption of a z-propagation only, neglecting the influence of the inhomogeneous magnetic field. In this case I can use the ansatz for the time of flight:

$$t_{tof} = \int_{t_0}^{t_{end}} \mathrm{d}t = \int_{z_0}^{z_{end}} \frac{1}{v(z)} \mathrm{d}z. \tag{6.1}$$

Using the conservation of energy law

$$E_{pot}(z_0) + E_{kin,0} = E_{pot}(z(t)) + \frac{1}{2} \cdot mv(z)^2 \tag{6.2}$$

assuming an initial kinetic energy per charge $q \cdot \tilde{E}_{kin} = E_{kin,0}$ and a time-independent potential $E_{pot} = q \cdot U(z)$ which only depends on the z-coordinate , the time of flight t_{tof} is

$$t_{tof} = \sqrt{\frac{m}{q}} \int_{z_0}^{z_{end}} \frac{1}{\sqrt{2\left(U(z_0) - U(z) + \tilde{E}_{kin,0}\right)}} \mathrm{d}z. \tag{6.3}$$

In the case of low kinetic energies, the integral depends only on the geometry and the applied voltages at the electrodes and the MCP. Consequently, referring to equation 6.3 the time of flight is linear with the square root of the mass-to-charge ratio and the ions of a particular species will arrange in a peak. The higher the mean kinetic energy of the released ions is, the higher is the spread of the time of flight. The time of flight of an individual ion depends on its current phase at the moment of ion release. Consequently, a high mean kinetic energy of the ions causes a high standard deviation of the time of flight. In addition also the mean time-of flight is reduced with high kinetic energy.

6.2.1. Identification of ion species

Table 6.1.: Measured times of flight of different ions with their corresponding mass and charge. The ion species is deduced from the mass-to-charge ratio.

peak	time of flight [µs]	ion charge [e]	ion mass [u]	formula	ion name
1	3.55	1	1	H^+	atomic hydrogen
2	5.00	1	2	$H_2{}^+$	molecular hydrogen
3	6.10	1	3	$H_3{}^+$	protonised hydrogen
4	8.45	2	12	C^{2+}	carbon
5	12.00	1	12	C^+	carbon
6	13.44	1	14	N^+	nitrogen
7	14.30	1	16	O^+	oxygen
8	14.73	1	17	OH^+	hydroxide
9	15.10	1	18	H_2O^+	water
10	15.44	1	19	H_3O^+	hydronium
11	18.68	1	28	CO^+	carbon monoxide
12	19.63	1	31	HNO^+	nitroxyl

The ion species stored inside the trap evolve over time as there are recombination mechanisms with the residual gas. The recombination rate and the reaction results depend on the gas

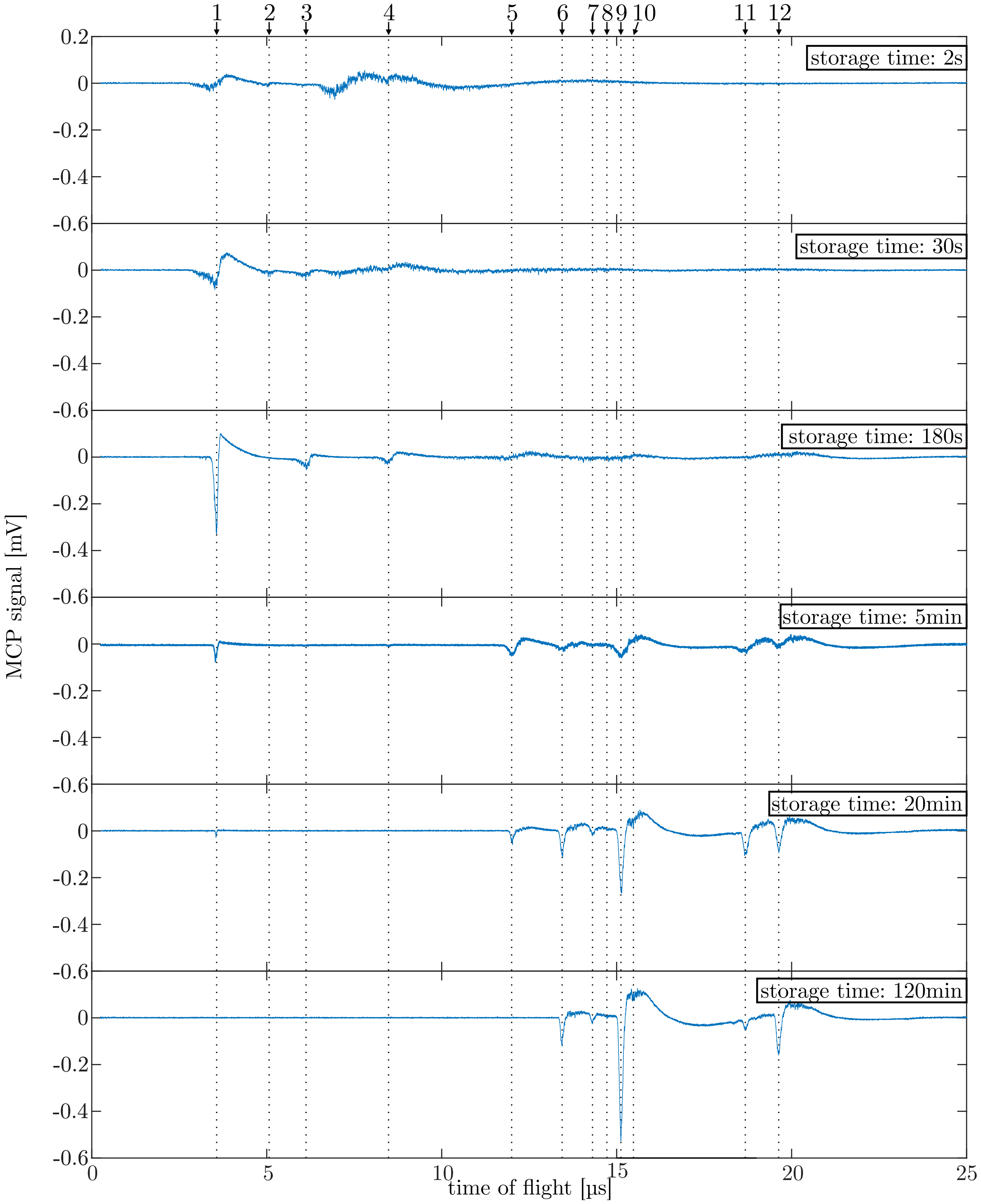

Figure 6.7.: Time-of-flight spectra of ejected ions after different storage times up to 2 h. The captured C^{2+} ions evolve over time and react with the residual gas particles.

composition and the pressure of the residual gas. In turn one can deduce the background pressure from the ion lifetime. To determine the evolution of the trap content and deduce properties of our storage environment, we have captured and stored C^{2+}-ions as described in section 6.1.2. The ions have been captured with an endcap voltage of 45 V. Using this endcap voltage and a floating ground potential of $U_{float} = 50\,\mathrm{V}$, the ion-trap content has been ejected after different storage times of up to two hours. Figure 6.7 shows time-of-flight spectra for six different storage times: 2 s, 30 s, 3 min, 5 min, 20 min, and 120 min.
The ion compositions emitted from the trap after a certain storage time differ from each other. Initially, no well-pronounced ion peak is visible. The ions are widely spread in time and appear as little peaks hardly distinguishable from backgound noise. After a storage time of 30 s a well-pronounced peak appears at 3.55 µs which evolves further with increasing storage time. After 3 min the ion peak of C^{2+} is visible clearly at a time of flight of about 8.2 µs. The evolution of both peaks over time is explainable by ion cooling. As no cooling is applied actively, this is probably caused by buffer-gas cooling. After a storage time of 5 min, peaks with a higher time of flight can be observed which belong to singly charged particles created from the residual gas due to recombination effects with the initially captured ions. Increasing the storage time further, the captured carbon ions have reacted or are lost by recombination completely and cannot be observed in the time-of-flight spectrum.
From the times of flight of the ejected ions, the ion or molecule species can be deduced. In table 6.1 the peaks are summarised and the corresponding charge state and ion mass in terms of elementary charge and elementary mass unit are given.

To verify the ion species I plotted the time of flight as a function of $\sqrt{\hat{m}/\hat{q}}$ of the deduced ion species. In figure 6.8 the carbon ions (C^{2+} and C^{+}) are represented by the blue hexagons while the ions from the residual gas and the reaction results are represented by the black dots. Following equation 6.3 one can expect a straight line through all points, when the initial kinetic energy is sufficiently low. I assume the kinetic energy of residual gas ions to be of the order of the room temperature equivalent and hence about 10 meV. This is much smaller than the initial potential energy of 50 eV/q controlled by the floating ground potential and can be neglected. In contrast, the carbon ions of both charge states have a significant energy remaining from the dynamic capture process. That is why only the black dots are taken into account for the fit procedure. The linear fit through the black dots matches well with the measurement data and hence the validity of the peak nomination in table 6.1 can be confirmed. Though the recombination rate of the initial C^{2+} ions is high and consequently the storage time is quite poor, it gives us the opportunity to detect a

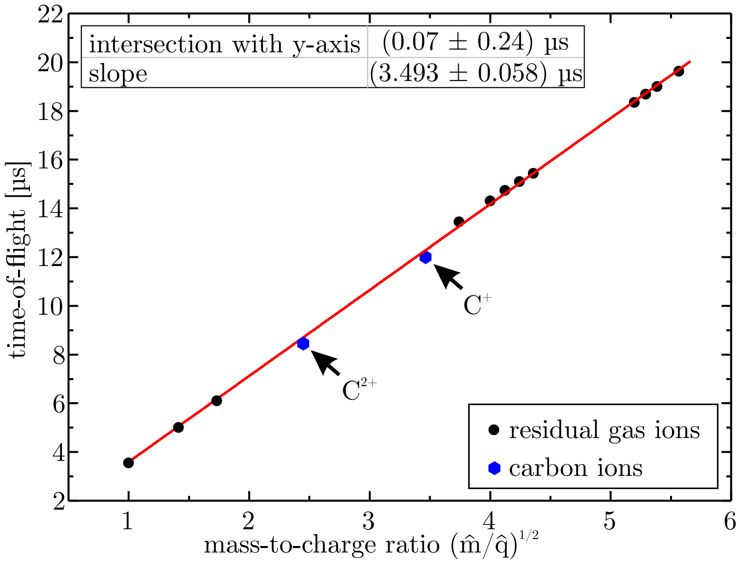

Figure 6.8.: Linear plot of the time of flight over the square root of the mass-to-charge ratio according to equation 6.3. Only the black dots are taken into account for fitting. The blue hexagons are the C^{2+} and C^{+} ions. Their times of flight are slightly smaller than expected by the plot due to initial kinetic energy.

variety of ion species to gauge the destructive ion-identification procedure.

Another question to be discussed is the reasonability of the ion nomination for a certain mass-to-charge ratio. The ion species in table 6.1 are deduced from the found charge-to-mass ratio and the typical composition of the residual gas. I assume here, that stored C^{2+} ions as well as residual gases such as H_2, H_2O, and N_2 are present. In the case of doubly charged carbon ions it is highly probable that they interact with the residual gas via charge exchange creating singly charged carbon and singly charged atomic or molecular ions, such as H^+, N^+, O^+, and H_2O^+. These ions we can observe clearly in the time-of-flight spectrum. In contrast, singly charged ions perform chemical reactions with the residual gas, creating singly charged molecular ions, such as ${H_3}^+$, CO^+, and HNO^+. The corresponding chemical reactions with their reaction rate are summarised in table A.1 in section A.3. Take as an example the reaction ${H_2}^+ + H_2 \longrightarrow {H_3}^+$. Assuming hydrogen as dominant residual gas at a temperature of 300 K and a pressure of 1×10^{-9} mbar, the rate for this reaction is about $0.1\,\mathrm{s}^{-1}$. If there exist a few hydrogen-molecule ions from charge exchange with stored C^{2+} ions, the creation rate of ${H_3}^+$ ions is of $1\,\mathrm{s}^{-1}$ which reacts itself with the residual gas. The creation and annihilation times of molecular ions of the order of seconds to minutes is hence reasonable.

In summary, also the nominated ions are reasonable and for future measurements using identical trapping parameters, the mass-to-charge ratio of ions can be determined from the time of flight following the relation:

$$(\hat{m}/\hat{q}) = \left(\frac{3.493\,\mu\mathrm{s}}{t_{tof}}\right)^2 . \tag{6.4}$$

Here, $\hat{m}$ and $\hat{q}$ are the integer multiples of the elementary mass unit and the elementary charge, respectively.

6.2.2. Destructive ion detection and ion lifetime

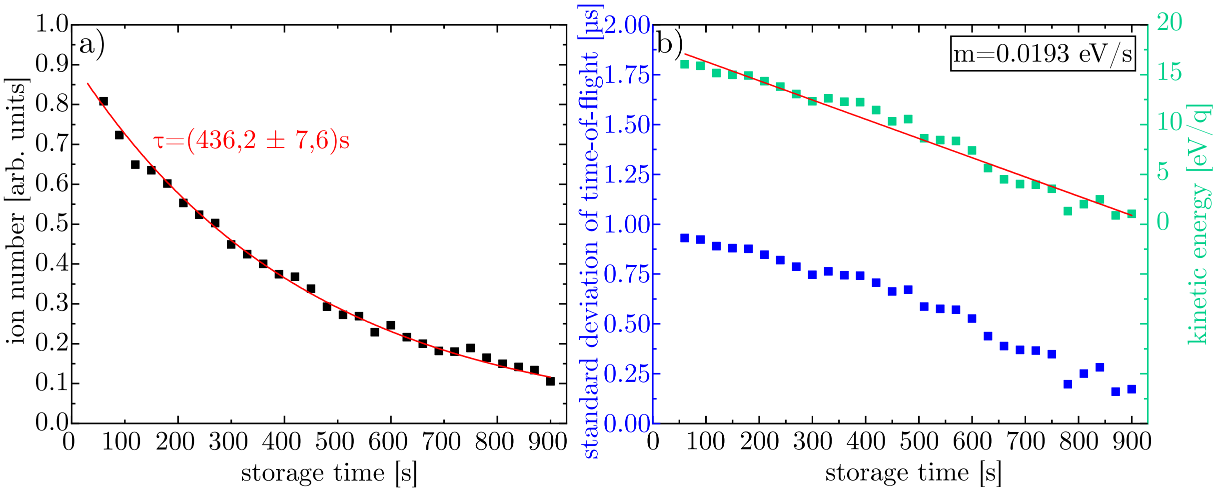

Figure 6.9.: a)Temporal evolution of the number of stored C^{2+}ions. The number was deduced from the time-of-flight signals of ejected ions after a certain storage time. b)Evolution of the temporal standard deviation of the C^{2+} ions' time of flight and the kinetic energy deduced therefrom.

The poor storage time caused by a background pressure above 1×10^{-9} mbar has been improved by an order of magnitude by the application of another vacuum pump. In this configuration, the storage time has been increased to several minutes. This has opened up the possibility to use the evolution of the C^{2+} peak to estimate the ion loss and the ion energy.

The ions have been extracted at a floating ground potential of 50 V and a trap voltage of 45 V and detected by a MCP detector. To determine the number of ions I use the MatLab embedded 'findpeak' function considering only peaks with a minimum peak prominence of 16 mV (see figure 6.4). The ion peaks are characterised with their time of flight (tof), their width (σ) and prominence (p). The width σ considers multiple ions hitting the MCP at a similar time. This pile-up of ion signals will cause a broadening of the ion peak. To have a relative value for the ion number I have taken the area below all peaks assumed a Gaussian shape. The ion number N can then be represented by the empirical relation

$$N \propto \sum_{i}^{\text{peaks}} p_i \cdot \sqrt{\sigma_i}. \tag{6.5}$$

The relative ion number is plotted in figure 6.9a. The absolute number could not be determined reliably by now and needs further measurements and fine calibration. Nevertheless, the determination of the relative ion number opens up the possibility to estimate the background pressure inside the trap from the decay time constant. Using equation 3.56 and assuming hydrogen to be the dominant residual gas, from the decay time constant of 436 s in figure 6.9 a background pressure of

$$p_{ionloss} = 2.1 \times 10^{-10}\,\text{mbar} \tag{6.6}$$

is determined. The assumption of hydrogen to be the dominant background gas is reasonable as the hydrogen peak is always present in the time-of-flight spectrum. The ionisation energy of hydrogen was taken from [78] and is 13.6 eV.

The ion energy can be deduced from the standard deviation σ using equation 6.3. For mean kinetic energies of 10 eV/q and beyond the ions are distributed over about ±10 mm in axial direction. In the moment of ion release they are distributed in this range which results both in an increase and decrease of the time of flight, depending on the current phase. Hence the peaks' standard deviation is increased. The time-of-flight spread for a certain initial kinetic energy has been calculated using equation 6.3 assuming different initial ion phases, and so the measured standard deviation of the time of flight could be transfered to a corresponding ion energy. Figure 6.9b shows the standard deviation of the time of flight and the corresponding mean kinetic energy. The data could be approximated by a straight with a slope of $(0.0193 \pm 0.0006)\,\text{eV}\,\text{s}^{-1}$ which corresponds to a cooling time of roughly 600 s, when the energy is decreased to $^1/_\text{e}$ of the initial value. Assuming again hydrogen as residual gas with a mobility of $\text{M}=12\,\text{cm}^2\,\text{V}^{-1}\,\text{s}^{-1}$ (see table 3.1), the background pressure can be determined with equation 3.54 to be:

$$p_{ionloss} = 2.5 \times 10^{-10}\,\text{mbar}. \tag{6.7}$$

The background pressures determined with both methods are comparable with each other. The determined background pressure is still high and causes a lot of ion loss especially for highly charged ions. In further updates of the setup, the vacuum has to be improved.

6.2.3. Non-destructive detection and ion cooling

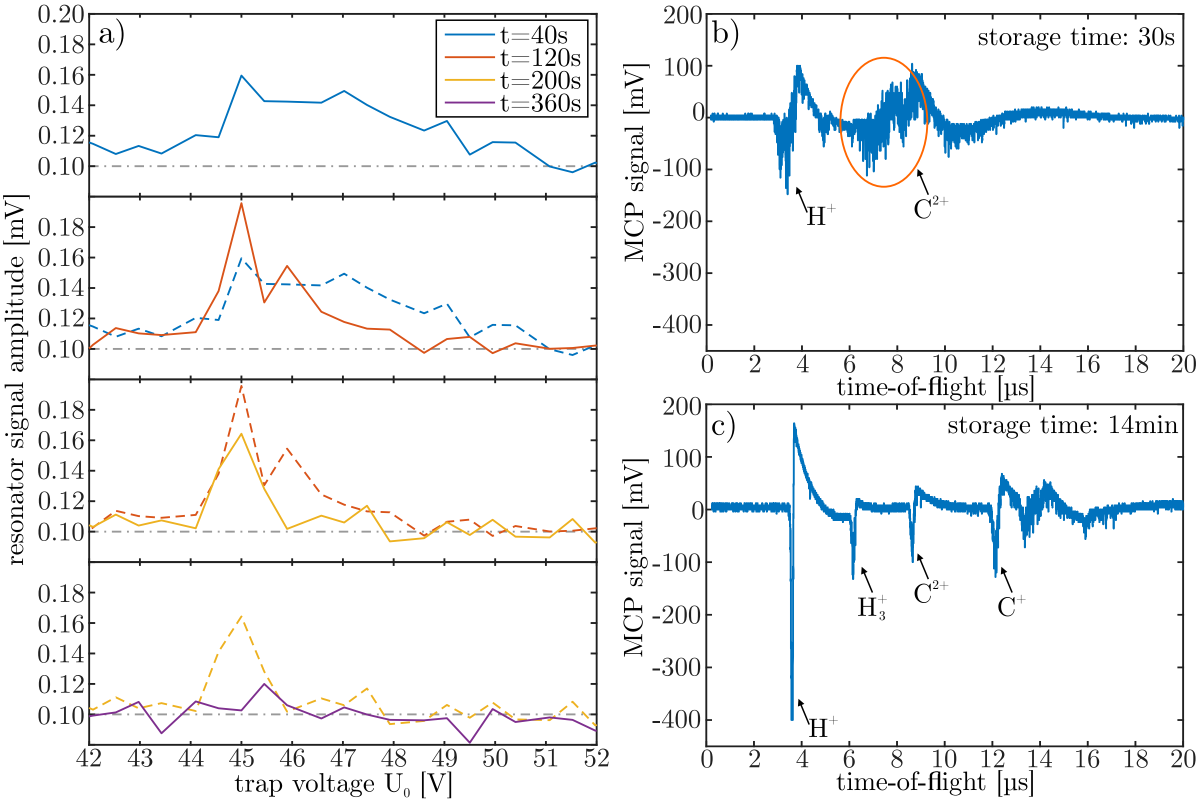

Figure 6.10.: a)Temporal evolution of the ion signal on the axial resonator. The dashed curves represent the graph of the respective previous ramp. The initially wide signal narrows over time and vanishes after approximately 6 minutes. b) Time-of-flight signal after a storage time of 30 seconds. The broad peak (highlighted) indicates high-energetic ions. c)Time-of-flight signal after a storage time of 14 min. The peak at 8.6 µs proves still stored C^{2+} ions. The small temporal spread indicates low-energetic ions.

The functionality of the non-destructive ion detection was also tested with C^{2+} ions. At this charge state we had the fortunate condition that the optimum endcap voltage for ion capture of 45 V offers an axial frequency of 416 kHz which can be covered by our resonant circuit. Also, the recombination rate with the residual gas has been small here which has allowed the run of several voltage ramps.

The signal has been acquired with a spectrum analyser Keysight N9000B CXA operated in the so-called zero span mode. The resonance frequency and the centre frequency were both set to 416 kHz. The resolution bandwidth has been set to 100 Hz which allows voltage steps of 0.5 V without losing relevant data.

After ion capture, we have scanned the trap voltage from 35 V to 55 V in steps of 0.5 V, first with increasing voltage and with decreasing voltage afterwards. The acquisition of a single direction took roughly 80 s. Figure 6.10a shows the magnitude of the ion signal depending on the applied trap voltage. The blue line in the upper graph shows the first single ramp after the ion capture. The maximum signal was detected at a voltage of 45 V which is reached after roughly 40 s. Increasing the trap voltage further, an ion signal can still be detected up to a trap voltage of 50 V. For later voltage ramps, the signal height for voltages above the nominal resonant voltage of 45 V decreases while there is no signal detectable below 45 V at any time. The occurance of signals at higher voltage can be explained by a reduction of the axial frequency of ions due to high energy. This assumption is confirmed by the wide spread ions in figure 6.10b, where the time-of-flight signal of extracted ions after a storage time of 30 s is shown. To further verify the assumption of high energetic ions, I have simulated the ion motion numerically along the z-axis in one dimension using the electric field introduced in section 5.4.1. I have assumed C^{2+} ions with different energies and have used the MatLab embedded function 'ode45' to solve the equations of motion for different trap voltages. The detailed description of the simulation will be explained later in section 7.1.2. From the ion motion the ion frequency can be obtained using a simple Fast Fourier transformation (FFT). Figure 6.11 shows the resonant voltage which has to be applied in order to bring an ion with a certain axial energy in resonance. Obviously, ions with an energy of roughly 12 eV/q are detected at a voltage of 50 V which is realistic for dynamically captured ions. The calculation also shows that up to an energy of 5 eV/q there is no change of the resonant voltage within the resonator's FWHM and the resonant voltage is not lower than 44.8 V at any time.

After a storage time of 120 s (orange line) the voltage spread is reduced significantly and the signal height at the nominal resonant frequency is increased which indicates cooling of the ions. After 200 s (yellow line) only at 45 V a significant signal can be observed. After roughly 6 min storage time the ion signal on the resonator has vanished completely and cannot be distinguished from the noise background anymore (purple line). The remaining ions were ejected after a storage time of 14 min. The peak at a time of flight of 8.2 µs corresponds to C^{2+}-ions. Consequently, the vanishing resonator signal is not a sign of lost ions but the induced signal has been too low to be detected due to their small kinetic energy.

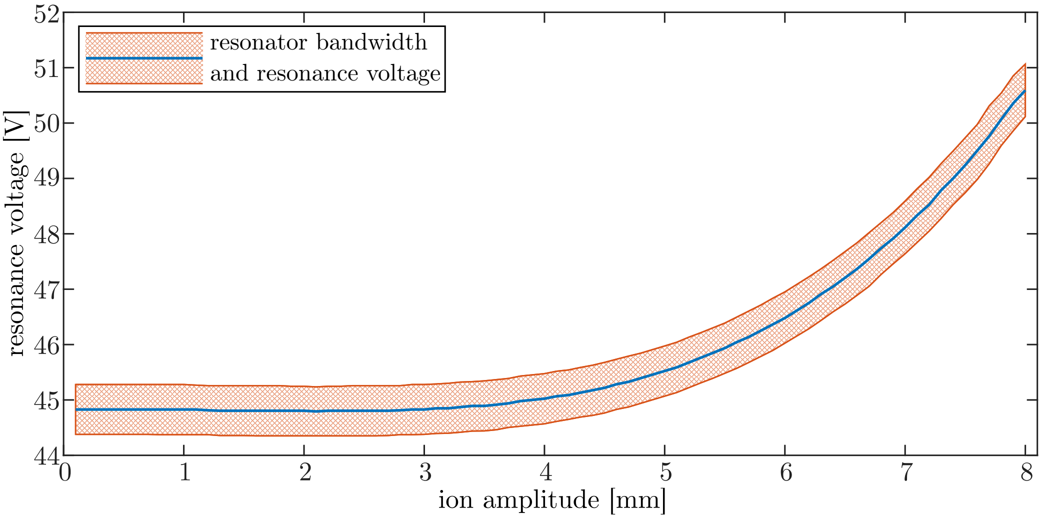

Figure 6.11.: Dependence of the resonance voltage of stored C^{2+} ions on the ion ocillation amplitude. The resonator's resonance frequency was assumed to be 416 kHz and the qualitity Q=100.

The voltage level of the purple resonator signal can be assumed to be the noise level of the whole axial detection system including resonator and amplifiers. The ion signal induced by the stored ions depends on the ion number and on the phase of the individual ions with respect to each other as well as on the ion energy. The amplitude of the induced signal is calculated as descibed in section 5.4.2. Assuming 100 stored ions with correlated phase, the ion energy is about 100 meV.

From the very first non-destructive ion measurements one can deduce two main results:

1. The present cooling mechanisms are capable of cooling the stored ions down to the milli-electronvolt regime. Unfortunately this takes about 5 min and is hence quite inefficient.

2. The dominant cooling mechanism is buffer-gas cooling. The storage time is hence reduced.

3. The non-destructive detection is currently limited to a high number of particles with an energy in the upper milli-electronvolt regime or a singly charged ion with an energy of 1 eV/q.

7. Resistive and active-feedback cooling: Simulation of cooling efficiencies

To form a rigid ion cloud, the ions have to be cooled down to a low kinetic energy in the lower meV - regime. The dynamically captured ions have kinetic energies of about 15 eV/q as found in the last chapter. The handling of ions with such high energy is not straight forward and common cooling techniques may not provide sufficiently short cooling times. In this chapter I will present the prospective cooling efficiency of resistive cooling with high-energetic ions and will introduce a modified version of active-feedback cooling which is designed especially to pre-cool high-energetic ions and I will present simulation results to estimate the cooling efficiency.

7.1. Resistive cooling

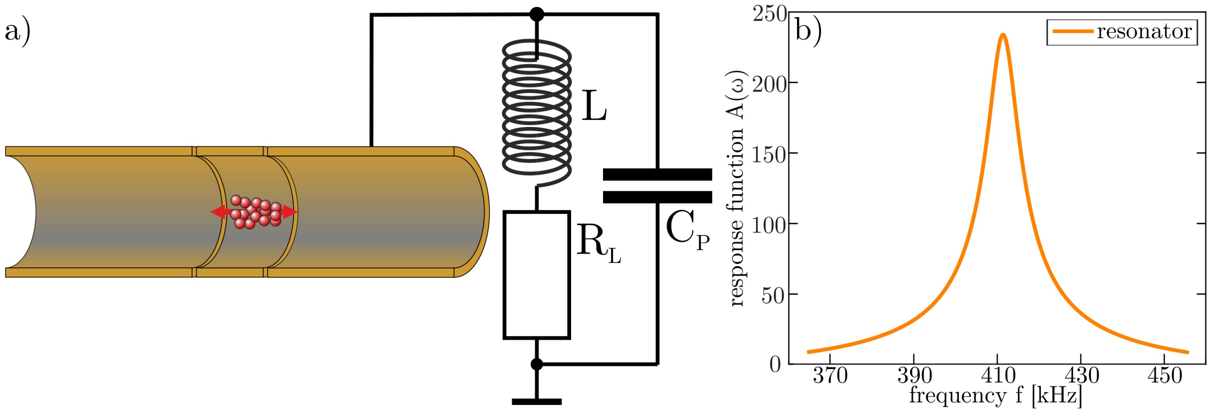

Figure 7.1.: a) Scheme of resistive cooling. The current induced to the electrode drives a resonant circuit with an inductance L, an Ohmic resistor R_L and a capacitance C_P. b) Exemplary resonator response function with its characteristic properties.

Resistive ion cooling is an established technique to cool ions and ion ensembles to low temperatures [53]. The stored ions induce a mirror charge Q_{ind} in a trap electrode. The subsequent current drives a resonant circuit connected to the pick-up electrode as depicted in figure 7.1. The resonant circuit consists of a coil with inductance L and an Ohmic resistance R_L. The parasitic capacitance C_P is the sum of all capacitive contributions, such as the resonator housing, cabling, and the pick-up electrode itself. Assuming a single particle with charge q and an initial total energy $\mathrm{E_{ion}}$ oscillating in z-direction, the induced current can be expressed as:

$$\begin{aligned} I(t) =& \frac{\mathrm{d}Q}{\mathrm{d}t} \\ I(t) =& -q \cdot \frac{\mathrm{d}\Gamma}{\mathrm{d}z}\frac{\mathrm{d}z}{\mathrm{d}t} = -\frac{q}{D}\frac{\mathrm{d}z}{\mathrm{d}t} \end{aligned} \tag{7.1}$$

The term $\left[\frac{\mathrm{d}\Gamma}{\mathrm{d}z}\right]^{-1}$ is the effective electrode distance D introduced in section 3.6.1. Now, for the resonant circuit a set of two differential equations can be set up:

$$\frac{\mathrm{d}U_c}{\mathrm{d}t} = \frac{1}{C}\left(I(t) - I_L(t)\right) \tag{7.2}$$

$$\frac{\mathrm{d}I_L}{\mathrm{d}t} = \frac{1}{L}\left(U_C(t) - I_L(T) \cdot R_L\right). \tag{7.3}$$

Combining both equations one gets:

$$0 = \frac{\mathrm{d}^2 I}{\mathrm{d}t^2} + \beta\frac{\mathrm{d}I}{\mathrm{d}t} + \omega_0^2(I - I(t)) \tag{7.4}$$

with

$$\omega_0^2 = \frac{1}{LC} \quad \text{and} \quad \beta = \frac{R}{L}, \tag{7.5}$$

where ω_0 ist the resonant frequency and β the damping coefficient. The characteristic property of a resonant circuit is the quality Q which is calculated with

$$Q = \frac{\omega_0}{\Delta\omega}, \tag{7.6}$$

where $\Delta\omega$ ist the bandwidth. For a parallel circuit as depicted in figure 7.1 it is

$$Q = \frac{1}{R}\sqrt{\frac{L}{C}} = \frac{\omega_0}{\beta}. \tag{7.7}$$

Comparing equations 7.6 and 7.7 the damping term β is equal to the bandwidth of the resonator. The response of a given resonant circuit depends on the frequency of the driving signal. Expressing therefore the current I_L as a complex function

$$I_L(t) = A(\omega)e^{i(\omega t+\phi)} \tag{7.8}$$

a single-frequency driving current $I(t) = B \cdot \sin(\omega t)$ causes a spectral amplitude inside the resonator of:

$$A(\omega) = \frac{B \cdot \omega_0^2}{\sqrt{(\omega_0^2 - w^2)^2 + \beta^2\omega^2}}. \tag{7.9}$$

In case the ion is in resonance with the resonator, the cooling time is determined by equation 3.47. Otherwise the cooling time is increased according to the quotient $A(\omega_0)/A(\omega)$. [50]
The theoretical description of resisitve cooling of highly charged ions inside Penning traps has been done in detail for single ions as well as for ion ensembles [50]. In experiments with ensembles of C^{5+} and Ar^{13+} cooling times of a few hundreds of milliseconds [53] and 3.5 s [79] have been achieved. At both experiments, the conditions were convenient to provide fast ion cooling with a high quality factor of the resonator, low energy spread of the ions and comparably small anharmonicities. At HILITE we have unfavourable conditions, namely:

- kinetic energies of about 15 eV/q with high energy spread
- high anharmonicity of the trap
- low Q-factor of approximately 100-150.

As described above, cooling is most efficient when the ions are in resonance with the resonant circuit. Due to the mentioned circumstances inside the HILITE Penning trap, the ion frequency spectrum will be much broader than the FWHM of the resonator and only a small portion of the stored ions can be cooled at one time directly.
In this chapter, I will have a detailed look at the prospective ion-cooling performance of HILITE with ions having an initially high kinetic energy. I will use the methods described in [50] and will modify them when necessary. I will apply the calculated electric fields of the HILITE trap electrodes and will give experimental advise resulting from my calculations.

7.1.1. The computational model

Typically, the z-motion of a stored ion is described by a sinusoidal function with a characteristic frequency ω_z. In the case of small anharmonicities and low ion energies this

description still holds true with a modified axial frequency [33]. In the HILITE Penning trap these conditions are not fulfilled. That is why I apply a full numerical calculation of the axial frequency and the cooling time. To retain a reasonable computation time, I assume a pure axial motion and will neglect ion-ion-interaction. As the ion-ion separation with high energies is high, this assumption is reasonable and is explained later.
The ion with a charge-to-mass ratio of q/m is assumed to be stored with an endcap voltage of U_0. $\tilde{E}_z$ is the normalized electric field for a trap potential of 1 V. The cooling force is caused by the z-component of the electric field of the split endcap electrode $U_{ec}(t) \cdot \tilde{E}_{ec,z}$. U_{ec} is the voltage of the resonant circuit and its evolution is described by the differential equations 7.2 and 7.3. $\tilde{E}_{ec,z}(z(t))$ is again the z-component of the normalised electric field of the split endcap electrode for a voltage of 1 V. Using these parameters one can set up the equation of motion for the z-component.

$$\ddot{z}(t) = \frac{q}{m} \cdot \left(U_0 \tilde{E}_z(z(t)) + U_{ec}(t) \tilde{E}_{ec,z}(z(t)) \right) \tag{7.10}$$

The resonant circuit is driven by the induced mirror charges of the stored particles with velocity $\mathrm{v_z}$ into the split-endcap electrode. Refering to equation 3.43 the magnitude of the induced current is calculated by

$$I_{ind}(t) = \frac{\mathrm{d}Q(t)}{\mathrm{d}t} = -q \cdot v_z(t) \frac{\mathrm{d}\Gamma_{ec}}{\mathrm{d}z}.$$

As the magnitude of the spatial derivative of the geometry function is equal to the normalized electric field of the electrode $\tilde{E}_{ec,z}(z(t))$, the induced current is

$$I_{ind}(t) = -q \cdot v_z(t) \tilde{E}_{ec,z}(z(t)). \tag{7.11}$$

Combining equations 7.10, 7.14, and 7.15 and converting them into a set of differential equations of the first order one gets:

$$\begin{aligned}
\dot{v}_z(t) =& \frac{q}{m} \cdot \left(U_0 \tilde{E}_z(z(t)) + U_{ec}(t) \tilde{E}_{ec,z}(z(t)) \right) && (7.12)\\
\dot{z}(t) =& v_z(t) && (7.13)\\
\dot{U}_c =& \frac{1}{C} \left(-q \cdot v_z(t) \tilde{E}_{ec,z}(z(t)) - I_L(t) \right) && (7.14)\\
\dot{I}_L =& \frac{1}{L} \left(U_C(t) - I_L(t) \cdot R_L \right). && (7.15)
\end{aligned}$$

7.1.2. Ion frequency

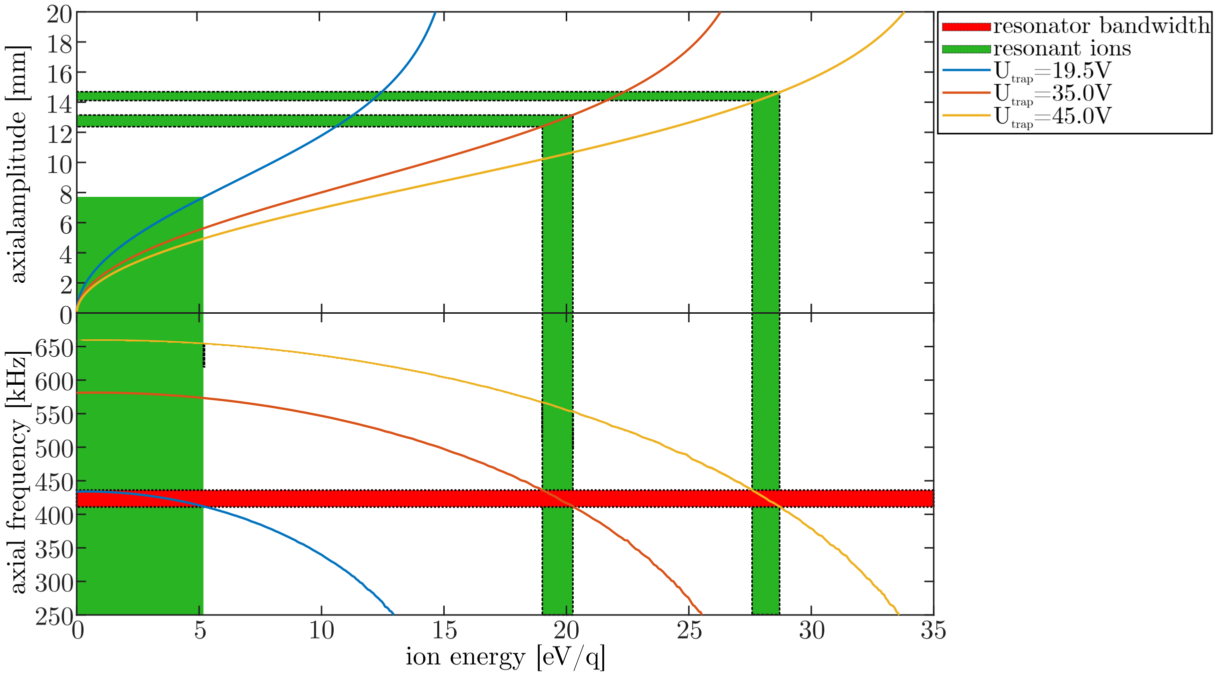

Figure 7.2.: Dependence of the ion frequency of C^{5+} ions on the ion energy. The red region marks frequencies inside the resonator's FWHM. The green regions mark the amplitudes and energies which are in resonance at certain trap voltages.

The efficiency of resistive cooling is highly dependent on the ion frequency which is itself strongly dependent on the ion kinetic energy due to the high trap anharmonicity. To deduce the ions' actual axial frequency I have calculated the motion along the z-axis neglecting any cooling contributions, evaluating only the first two differential equations 7.12 and 7.13 setting U_{ec}=0.

The equations of motion are evaluated with a MatLab embedded solver for ordinary differential equations (ode45). As ion species I have chosen C^{5+}. I have calculated the ion motion for a time of 10 ms with different amplitudes. The ions have been assumed to be initially at rest. From the ion motion (z(t)) I have calculated the frequency distribution using a FFT. Especially for high energetic ions, higher harmonic frequencies occur, but their amplitude is still well below the amplitude of the fundamental.

The oscillation frequency with respect to the ion energy and the corresponding ion amplitude at different ion energies are shown in figure 7.2. I added the frequency band that is covered by our axial resonator in order to visualise the overlap of the resonator with the frequencies of the ions. I assume a resonant circuit tuned to a resonance frequency of 433.9 kHz. The

Q-factor and the damping β here are 101 and 26.0 kHz, respectively. Ions with an energy up to 5 eV/q are in resonance with our resonator and can be detected and cooled. To detect ions with higher energy the trapping voltage has to be increased. The range of ion energies covered at higher voltages is about 0.2 eV/q. In consequence, about 1% of the prospected energy range of the ions is covered and hence only a few ions are cooled.

7.1.3. Resistive cooling using a voltage ramp

To adress all ions of the ensemble it is necessary to scan the trap voltage. This brings all the ions temporarily in resonance. From figure 7.2 one can deduce that the frequency of ions increases with decreasing energy. Obviously, if resistive cooling is applied to a high-energetic ion, it will move out of the resonance. This can be compensated by a subsequent decrease of the voltage. In the following I will describe, how it is possible to cool ions of all energies resistively using a voltage ramp.

I performed a calculation for C^{5+} using equations 7.12 to 7.15 for ions with different initial amplitudes which oscillate independently from each other. For a trap voltage of 35 V, where the capture efficiency is best, the frequency width of the ions with an energy range between 0 eV/q and 25 eV/q is about 200 kHz, while the FWHM of the resonator is only 26 kHz. In order to address all ions with the resonator, the trap voltage has to be tuned.

To speed up the calculation I have assumed an ion bunch with a particle number $N_{part} = 1000$ which has no spatial extend and no inner forces. This increases the cooling force by a factor of 1000 and thus decreasing the decay time constant of the ions also by a factor of 1000 (refer to equation 3.49). For the present configuration, the cooling time constant is of the order of 4 ms and still much higher than one oscillation period, wherefore equations 3.47 and 3.49 are still applicable. As resonator parameters I have used a resonance frequency and a damping constant of $\omega_0 = 433.9$ kHz and $\beta = 26$ kHz, respectively. I calculated the evolution of the particles for a time of 1 s. In the beginning the trap voltage is 35 V and is increased up to 45 V and then decreased to 19.2 V. The actual time dependence of the voltage ramp is depicted in figure 7.3 in the lower graphs.

The calculation results are shown in figures 7.3a and 7.3b, where the first one shows the energy evolution and the latter the amplitude evolution. Increasing the trap voltage does also cause an increase of the ion energy. As the average energy gain per oscillation period of the ions is less than the increase of the trap potential, the amplitudes of the ions decrease. The solid lines represent calculations including ion cooling while the dashed lines are calculated without ion cooling as reference. Here the energy reduction is only due to the

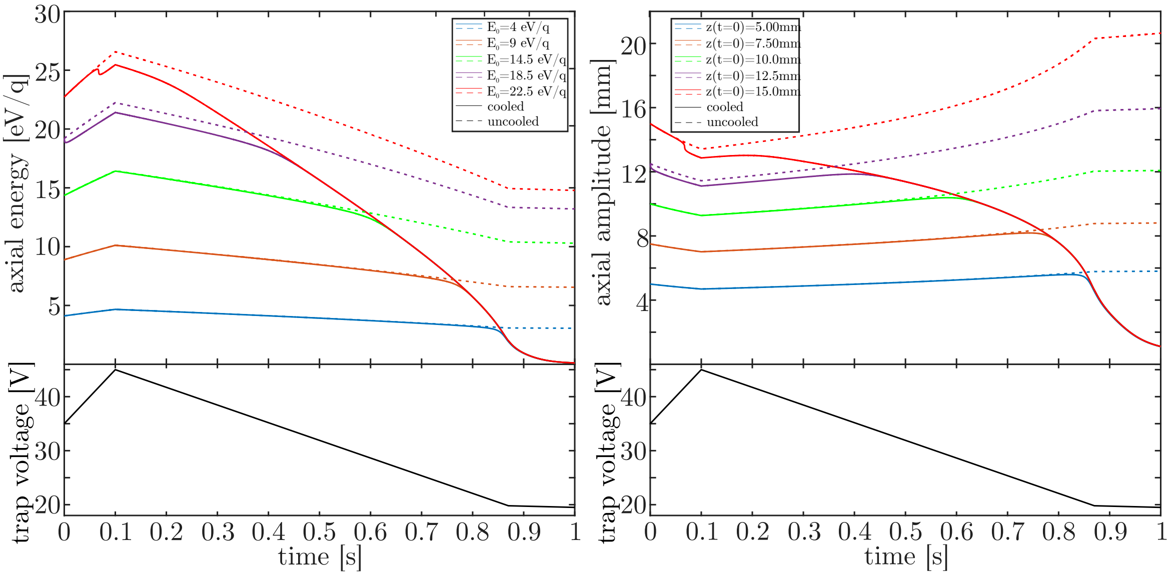

Figure 7.3.: Resistive cooling of stored ions with with different initial energies. The trap potential is tuned during the cooling process and the evolution of the particle energy (a) and the particle amplitude (b) is plotted. The dashed line shows the evolution without cooling and the solid line including cooling.

decrease of the trap potential.

Exemplarily, the graphs show ions with initial amplitudes and energies of 5 mm (4 eV/q), 7.5 mm (9 eV/q), 10 mm (14.5 eV/q), 12.5 mm (18.5 eV/q) and 15 mm (22.5 eV/q). Comparing all graphs amoung each other, the cooling starts at different trapping potentials. Ions with an initial energy of 4 eV/q (blue) are cooled, when the trapping voltage is lower than 20 V. There is no cooling before. Decreasing the voltage further keeps them still in resonance and the cooling proceeds. Ions with an initial energy of 22.5 eV/q (red) are cooled right in the beginning, but go then out of resonance, when the voltage is increased. When the voltage is about 40 V again when decreasing the trap voltage, cooling proceeds. Ions with energies inbetween are cooled for trap potentials between 45 V and 20 V. The cooled ions increase the oscillation frequency and are in resonance again at lower trap voltages. So, due to the slow reduction of the voltage, the ions are held in resonance and cooled persistently. While the decreasing voltage ramp is driven, all ions are addressed by the resonator and hence cooled at different times. When all ions have an amplitude of 5 mm and an energy of 4 eV/q or below they have an axial frequency inside the FWHM of the resonator and are cooled simultaneously.

From this calculation one can deduce, that driving a voltage ramp is an applicable option to cool ions of all energies down to low energies. The resulting cooling time for the ions in the assumed configuration with 1000 correlated ions is about 1 s. In reality, one might have to consider complete uncorrelated ions. In this case the cooling time is 1000 s, so roughly a quarter of an hour.

7.2. Active-feedback cooling

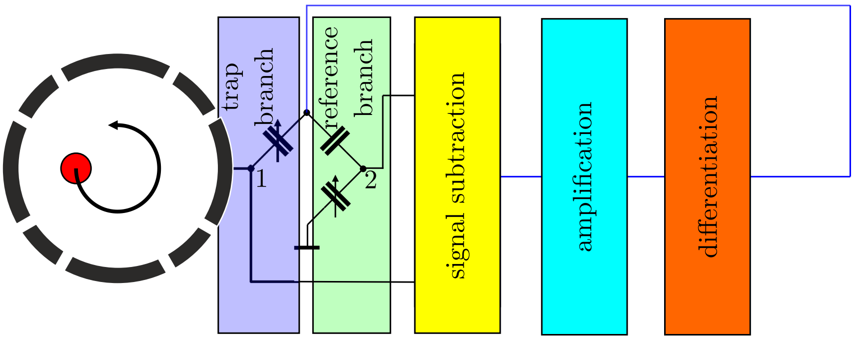

Figure 7.4.: Basic concept of active-feedback cooling. The pick-up signal and the excitation signal are subtracted from each other. The difference signal is amplified and differentiated with respect to time and fed back to the ring electrode.

Active-feedback cooling was discussed in particular for single particles as well as for single anti-matter particles [57, 80]. There, the stored particles are cooled to temperatures well below the limit of resistive cooling which is the temperature of the cooling circuit as well as the temperature associated with the electronic noise. In our case, we will use this technique to perform a wideband cooling of an ion ensemble with an arbitrary axial energy distribution. After ion capture, the ions have axial energies of several tens of electronvolts and a high energy spread. As discussed in section 7.1.3, resistive cooling has a significantly reduced efficiency in such ion ensembles. That is why we apply an adapted version of active-feedback cooling. The scheme in figure 7.4 summarises the single steps of the method The basic idea is to pick-up the signal of the oscillating ions with subsequent application of the same but amplified and phase-shifted signal back to the same electrode. In our experimental setup, we use only a single segment of the ring electrode. This allows an immidiate application of the cooling signal to the ion which has induced the signal. On the other hand, using a ring electrode segment also the cooling of the radial motion is attainable.

Obviously, applying the feedback signal back to the pick-up electrode causes a strong crosstalk between ion signal and the cooling signal itself. To overcome this issue, I have designed and built an electronic device which filters the induced ion signal out of the superimposed feedback signal using a Wheatstone bridge [81] consisting of four capacitors, where one of them is the trap electrode itself. Both tappings in figure 7.4 are subtracted from each other leaving only the induced ion signal. The resulting signal is amplified, differentiated, and fed back to the trap electrode.

The electronic realisation of the active-feedback cooling is done using two distinct electric circuits - a cryogenic part and a room-temperature part. In this section, I will describe the electronic circuits, characterise the realised electronic devices and give simulation results to estimate the efficiency of the procedure.

7.2.1. The cryogenic cooling board

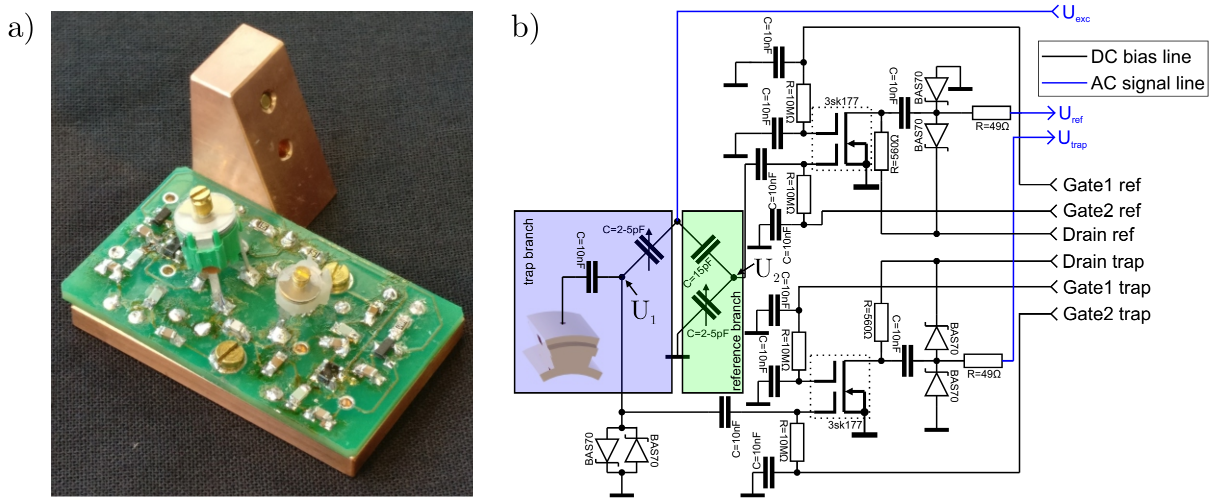

Figure 7.5.: a)Photo of the cryogenic filter board connected to a copper holder. The two tunable capacitors are placed in the centre of the board. b)The electric circuit of the cryogenic cooling board. The blue and the green boxes contain the two branches of the Wheatstone bridge.

The heart of the cooling mechanism is placed on the cryogenic filter board - *the capacitive Wheatstone bridge* [81].

The Wheatstone bridge consists of four capacitors C_{trap1}, C_{trap2}, C_{ref1}, and C_{ref2} where C_{trap2} is the ring-electrode segment itself. This Wheatstone bridge can be recognised as two independent branches of a pair of capacitors connected in series. The so-called *trap branch* highlighted by the blue box consists of a tunable capacitor and the trap electrode and the so-called *reference branch* highlighted in green consists of a tunable capacitor and a fixed one. In an ideally balanced Wheatstone bridge the condition

$$\frac{C_{trap1}}{C_{trap2}} = \frac{C_{ref1}}{C_{ref2}} \tag{7.16}$$

is fulfilled and the nodes '1' and '2' are always on the same potential independent from the applied excitation signal U_{exc}. The signal caused by the ions' motion U_{ion} is only induced to the trap branch and is the only remaining signal after subtraction. The induced voltage of N ions with the same charge q and position $\vec{r_i}$ is:

$$U_{ion}(t) = \frac{q}{C_{trap2} + C_{gate}} \sum_{i}^{N} \Gamma_{ring}(\vec{\mathbf{r}}_i(t)). \tag{7.17}$$

$\Gamma_{ring}(\vec{\mathbf{r}}_i(t))$ is the geometry function of the ring-electrode segment given in section 5.4.2. The capacitance $C_{gate} = 1\,\text{pF}$ of the gate-source transition inside the transistor is in parallel to the electrode and added, while the high-capacitance coupling capacitor in series can be neglected. Now, the voltage at node '1' is the superposition of the excitation voltage and the induced voltage, while the voltage at node '2' is only connected with the excitation voltage. The voltages U_1 and U_2 are:

$$U_1 = \frac{C_{trap1} + C_{trap2}}{C_{trap2}} \cdot U_{exc} + U_{ion} \tag{7.18}$$

$$U_2 = \frac{C_{ref1} + C_{ref2}}{C_{ref2}} \cdot U_{exc}. \tag{7.19}$$

As the capacities of the Wheatstone bridge are typically between 5 pF and 15 pF, the connection of any capacitive load, such as cables, influences its performance. To reduce the capacitive load of the Wheatstone bridge, I use a MESFET (metal–semiconductor field-effect transistor)-based electrical circuit in each branch. The MESFET is a '3sk177' which is a GaAs dual-gate transistor with two gates G1 and G2. The signals U_1 and U_2 drive the respective input G1 (gate1) of the transistors. The bias voltages of the gates of both transistors and their drain ports are tuned individually and independently. Varying those six voltages, the working point and hence the amplification properties can be influenced. In this way, the amplitude and quality of the output signals U_{trap} and U_{ref} can be set.

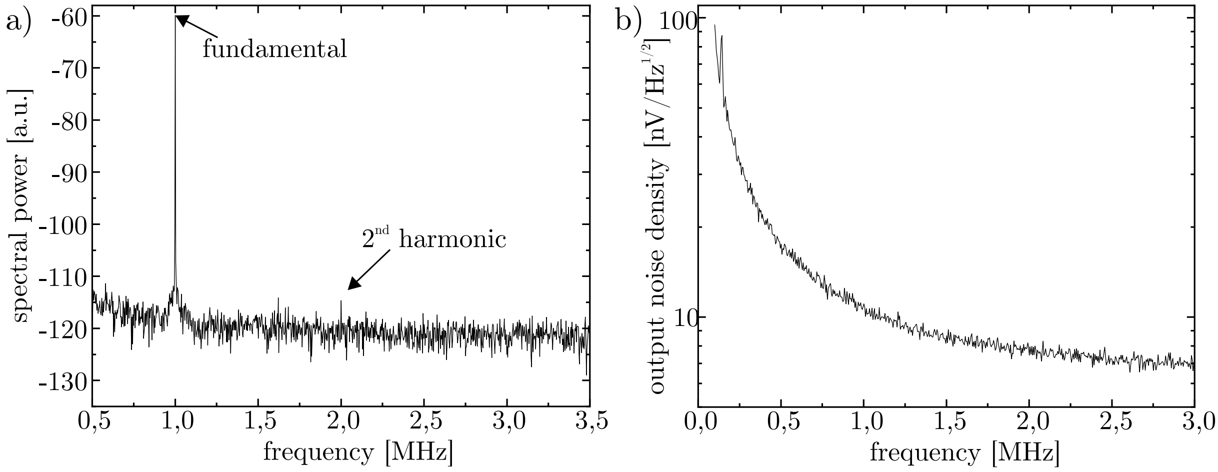

Figure 7.6.: a) Spectrum of the output signal of the trap branch. The missing higher order peaks indicate that the output signal is a pure sine as the input. b) Output noise density of the trap branch.

The purpose followed here is the almost exact transmission of an induced signal through the transistor circuit. To test this signal transition behaviour, we have applied a sinusoidal signal with a frequency of 1 MHz to the excitation input and have monitored the spectral power on the spectrum analyser. Figure 7.6a shows the acquired spectrum for the trap branch. If there would have been any distortion of the signal, we had monitored the appearance of higher harmonics. Since in our case only the fundamental is present, the signal can be assumed to be undistorted.

The other aspect is the noise which competes with the output signal. Figure 7.6b shows the output noise density of the trap branch. Currently, it is high compared to commercial available amplifier systems and has to be reduced in the further development.

7.2.2. The differential board

Inside the trap chamber close to the trap electrode the two signals U_{trap} and U_{ref} are generated. Afterwards they are guided out of the vacuum through the electrical feedthrough flange. The feedback signal is generated from these two signals. To this end, I have designed and built the so-called *differential board*. On this board the further steps 'subtraction', 'differentiation' and 'amplification' are embedded. Additionally, a low-pass filter is applied to reduce high-frequency contributions above 5 MHz.

The signals U_{trap} and U_{ref} are connected to the differential amplifier 'AD8132' which amplifies the signals at the inputs IN1 and IN2 and the difference of the amplified input

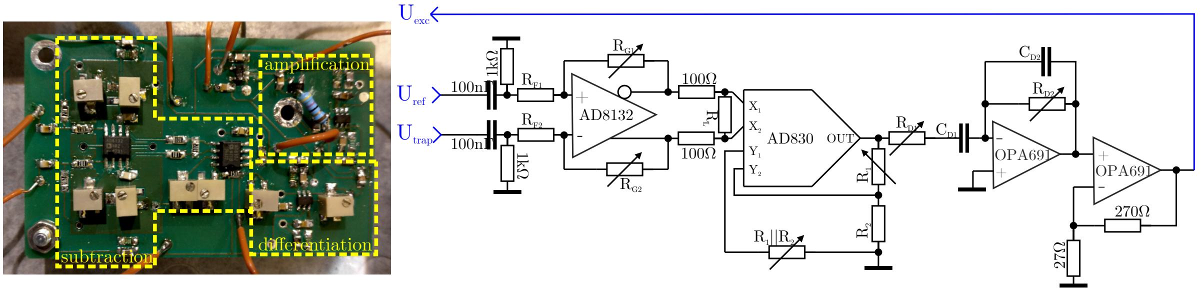

Figure 7.7.: a)Photo of the differential cooling board and b)the electrical circuit of the differential board.

signals is gained at OUT1 and OUT2, where OUT2 is the negated signal of OUT1. The amplification factor of both inputs can be set individually tuning the resistors $R_{G1,2}$ and $R_{F1,2}$, respectively. This amplifier has a two-ended output and the voltage between OUT1 and OUT2 is:

$$OUT1 - OUT2 = 2 \cdot \left(U_{ref} \cdot \frac{R_{G1}}{R_{G1} + R_{F1}} - U_{trap} \cdot \frac{R_{G2}}{R_{G2} + R_{F2}} \right) \tag{7.20}$$

The resistors R_{F1} and R_{F2} have a value of $500\,\Omega$. The resistors R_{G1} and R_{G2} are realised by a pair of potentiometers connected in series with the maximum values of $2\,\mathrm{k}\Omega$ and $50\,\Omega$ for coarse and fine tuning of the amplification. Tuning the amplification of the channels, an amplitude difference in the cryogenic board can be compensated.

The two-ended output signal is converted to a single-ended output signal by a ’AD830’ - integrated circuit with adjustable gain. The voltage over the resistor $\mathrm{R_L}$=$200\,\Omega$ is coupled to the inputs X1 and X2. The output OUT is coupled back with three resistors to the inputs Y1 and Y2, in order to control the gain of the ’AD830’. The output voltage at the ’AD830’ is

$$OUT = (OUT1 - OUT2) \cdot \left(1 + \frac{R_1}{R_2} \right) \tag{7.21}$$

and can hence be tuned by the potentiometers $\mathrm{R_1}$ and $\mathrm{R_2}$.

Afterwards, this single-ended output signal is differentiated by an operational amplifier ’OPA691’, operated as differentiator [81]. In this configuration shown in figure 7.7, the amplification is determined by the resistors $\mathrm{R_{D1}}$ and $\mathrm{R_{D2}}$ as well as the capacitors $\mathrm{C_{D1}}$ and $\mathrm{C_{D2}}$. The electric circuit here is designed as a band pass with the lower limit $\mathrm{f_{low}}$ and upper limit $\mathrm{f_{high}}$ defined by:

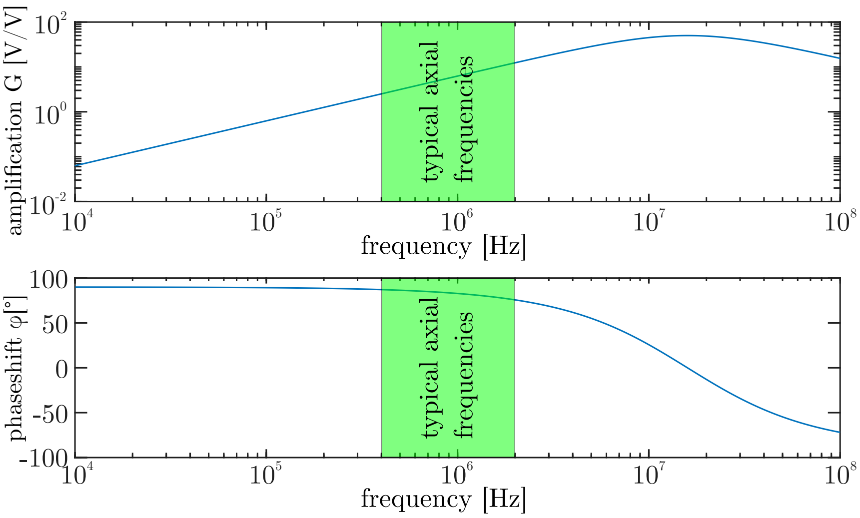

Figure 7.8.: Frequency-dependent amplification (upper graph) and phase (lower graph) of an operational amplifier operated as differentiator. In the region of typical frequencies between 1 MHz and 2 MHz the amplification is almost linear with the frequency and the phaseshift is only slightly below 90°.

$$f_{low} = \frac{1}{2\pi R_1 C_1} \tag{7.22}$$

$$f_{high} = \frac{1}{2\pi R_2 C_2}. \tag{7.23}$$

The amplification of this configuration is [81]

$$G(f) = \frac{R_{D2}}{R_{D1}} \left[\sqrt{\left(1 + \left(\frac{f}{f_{high}}\right)^2\right) \cdot \left(1 + \left(\frac{f_{low}}{f}\right)^2\right)} \right]^{-1} \tag{7.24}$$

with a phase shift:

$$\varphi(f) = \arctan\left(\frac{f_{low}}{f}\right) - \arctan\left(\frac{f}{f_{high}}\right). \tag{7.25}$$

Figure 7.8 shows the frequency-dependent gain and phase shift of an operational amplifier operated as differentiator. In our application, we run the amplifier far below the lower limit at frequencies below $f_{low}/10$, where the phase shift is close to 90° which corresponds to the first derivative of the input signal. Limiting the amplification above a certain bandwidth reduces the noise which otherwise would affect the ions' motion. Choosing the bandwidth

too low causes a phase shift lower than 90° which reduces the cooling efficiency.
The upper and the lower limit and the amplification is adjusted according to the oscillation frequencies of the stored ions by tuning the resistance of the potentiometers R_{D1} and R_{D2}. Here, I assume limit frequencies of 8 MHz and 20 MHz.
The last amplification stage is realised by an 'OPA691' operational amplifier with a fixed amplification of 11 determined by the resistors R_{A1} and R_{A2}. The signal now is fed back to the signal input of the cryogenic filter board to cool the stored ions inside the trap.

7.2.3. Characterisation of the full electronics

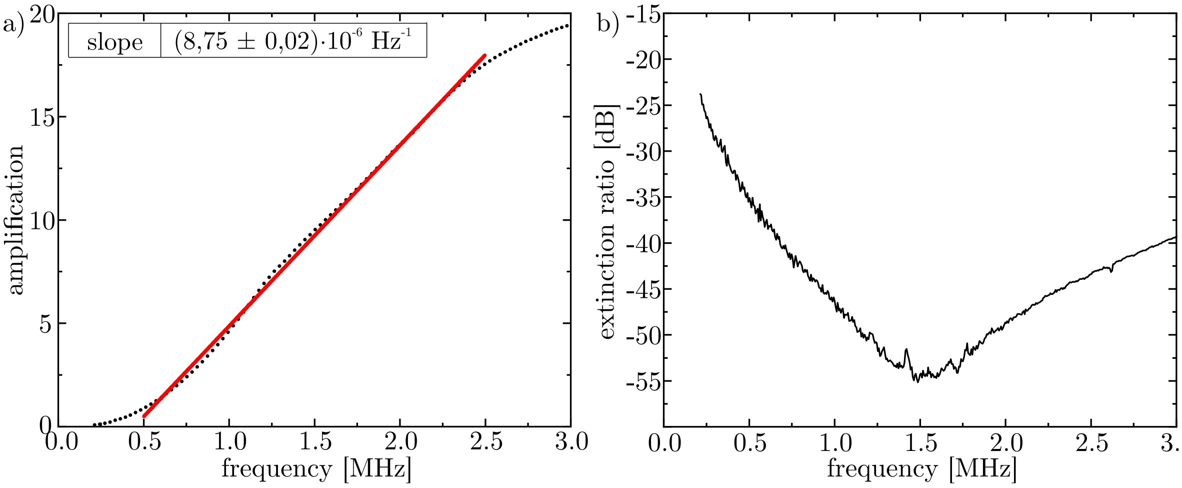

Figure 7.9.: a) Frequency dependence of the amplification of the full cooling electronics. The amplification rises linearly with the frequency between 750 kHz and 2.25 MHz. b) Extinction ratio of the cooling electronics. Between 1.2 MHz and 1.8 MHz the extinction ratio is better than −50 dB which is about 1:316.

The main purpose of the active-feedback electric circuit is the extinction of the exciting signal and the phase shift by 90°. The phase shift of 90° is accomplished by the design of the active low-pass filter. To test the frequency dependence of the circuit, I have connected only the trap input to the tracking generator of a spectrum analyser and have recorded the amplified spectrum. The reference input has been set to ground. Figure 7.9a shows the dependence of the amplification with respect to the frequency. The amplification rises linearly with the frequency between 750 kHz and 2.25 MHz as expected which indicates that the circuit acts as an active differentiator (see figure 7.8).
To reduce the crosstalk between the excitation signal and the pick-up signal the extinction

ratio has to be as low as possible. We have connected the excitation input of the cryogenic cooling board with the tracking generator of the frequency analyser and have monitored the difference signal. Then we have tuned the overall electronics to achieve the lowest possible crosstalk. In the current configuration, we have achieved an extinction ratio af less than $-50\,\mathrm{dB}$ between $1.2\,\mathrm{MHz}$ and $1.8\,\mathrm{MHz}$ and $-55\,\mathrm{dB}$ at $1.5\,\mathrm{MHz}$. Since the ions pass the ring electrode twice per oscillation periode, the frequency of the induced signal is twice the axial frequency. So simultaneous cooling of ions with axial frequencies between $600\,\mathrm{kHz}$ and $900\,\mathrm{kHz}$ is most efficient.

7.2.4. Simulation of the active-feedback cooling

The approach of active-feedback cooling using the electronics described before is highly ambitious and is investigated here theoretically.

The active-feedback cooling technique is applied to a ring-electrode segment which covers an azimuthal extent of 60°. The ions inside the trap induce their charge into this very electrode and the induced voltage will follow the ion motion. The geometry function Γ_{AFC} is shown in figure 5.10 and the induced voltage of a single species ion ensemble with arbitrarily distributed ions is then

$$U_{ion} = -\frac{1}{C_{ring}} \sum_{i}^{ions} \Gamma_{ion}(\vec{r}_i) \cdot q. \tag{7.26}$$

To reduce the computation time to a resonable degree, the calculation is only performed in the z-direction neglecting direct ion-ion-interaction. The reduction to pure axial motion is acceptable, as the electronics anyway filter the high frequency contributions by design. The interaction time needed by the ions to thermalise can be estimated by the Spitzer self-collision time τ_S [53] following

$$\tau_S \approx (4\pi\varepsilon_0)^2 \, \frac{3\sqrt{m}(E\cdot e)^{\frac{3}{2}}}{4\sqrt{\pi}nq^4 \ln\Lambda} \quad \text{with} \quad \ln\Lambda = 23 - \ln\left(\frac{2nq^6}{e^6E^3}\right)^{\frac{1}{2}}. \tag{7.27}$$

Assuming 2000 C^{5+} particles distributed $20\,\mathrm{mm}$ along the axial direction and within a radius of $2.5\,\mathrm{mm}$, one has a particle density n of $5.1\,\mathrm{mm}^{-3}$. The mean ion energy E is given in eV and is assumed to be $75\,\mathrm{eV}$ ($15\,\mathrm{eV/q}$). In this configuration, the corresponding self-collision time is about $12\,\mathrm{min}$. As the cooling mechanism is only calculated for an application time of $30\,\mathrm{s}$, the neglection of ion-ion-interaction is reasonable.

During the active-ion cooling process, the ions are stored inside the trapping potential of the endcap electrodes which are set to a voltage U_{trap}. The cooling force is caused by the excitation signal U_{exc} applied to the ring electrode segment. The equations of motion now are:

$$\dot{v}_z(t) = \frac{q}{m} \cdot \Big(U_0 \tilde{E}_z(z(t)) + U_{exc}(t) \tilde{E}_{z,ring}(z(t))\Big) \tag{7.28}$$

$$\dot{z}(t) = v_z. \tag{7.29}$$

Here $\tilde{E}_z$ and $\tilde{E}_{z,ring}$ are the normalised electric fields containing the spatial information, while the applied voltages scale the magnitude of the electric fields. Per design, the excitation voltage is the first derivative with respect to time of the pick-up signal multiplied by an amplification factor k:

$$U_{exc} = -k \cdot \frac{\mathrm{d}U_{ion}}{\mathrm{d}t} = k \cdot q \cdot \frac{1}{C_{ring}} \sum_{i}^{ions} \left.\frac{\mathrm{d}\Gamma_{ring}}{\mathrm{d}z}\right|_{z=z_i} \cdot v_{z,i}(t). \tag{7.30}$$

According to figure 5.10, the geomety function is highest for ion amplitudes around 10 mm and will converge to zero, when the ions are confined in the trap centre and hence the cooling efficiency will be decreased.

The evolution of the ion motion is calculated using the Adam-Bashford method [82]. This is a multistep iterative calculation technique. I use the latest five steps to calculate the next iteration step. The initial five steps are calculated using the Runge-Kutta method of 6th order [82]. The iteration follows the relation

$$y_{i+1} = y_i + \frac{\Delta t}{1440} \cdot (4277 \cdot f_i - 7923 \cdot f_{i-1} + 9982 \cdot f_{i-2} - 7298 \cdot f_{i-3} + 2877 \cdot f_{i-4} - 475 \cdot f_{i-5}) \tag{7.31}$$

where

$$y_i = \begin{pmatrix} z_i \\ v_{z,i} \end{pmatrix} \quad \text{and} \quad f_i = \begin{pmatrix} v_{z,i} \\ \dot{v}_{z,i} \end{pmatrix}. \tag{7.32}$$

In order to take the crosstalk between excitation and pick-up into account, the expression for the excitation voltage defined by equation 7.30 has to be modified. The ion signal calculated for the i-th iteration step is superimposed by a certain fraction χ of the excitation signal. The crosstalk has to be multiplied by the gain and differentiated with respect to time. The modified feedback voltage is now:

$$U_{exc} = k \cdot \frac{\mathrm{d}U_{ion}}{\mathrm{d}t} + k \cdot \chi \frac{\mathrm{d}U_{exc}}{\mathrm{d}t}. \tag{7.33}$$

In the discrete formulation the feedback voltage of the i-th iteration step is:

$$U_{exc,i} = k \cdot \frac{\mathrm{d}U_{ion}}{\mathrm{d}t} + k \cdot \chi \frac{U_{exc,i} - U_{exc,i-1}}{\Delta t}. \tag{7.34}$$

Resolving this equation with respect to the exciting voltage for the i-th iteration step, one gets:

$$U_{exc,i} = \frac{k \cdot \chi}{k \cdot \chi + \Delta t} \cdot U_{exc,i-1} - \left(\frac{\Delta t \cdot k}{k \cdot \chi + \Delta t}\right) \cdot \frac{\mathrm{d}U_{ion}}{\mathrm{d}t}. \tag{7.35}$$

Simulation parameters

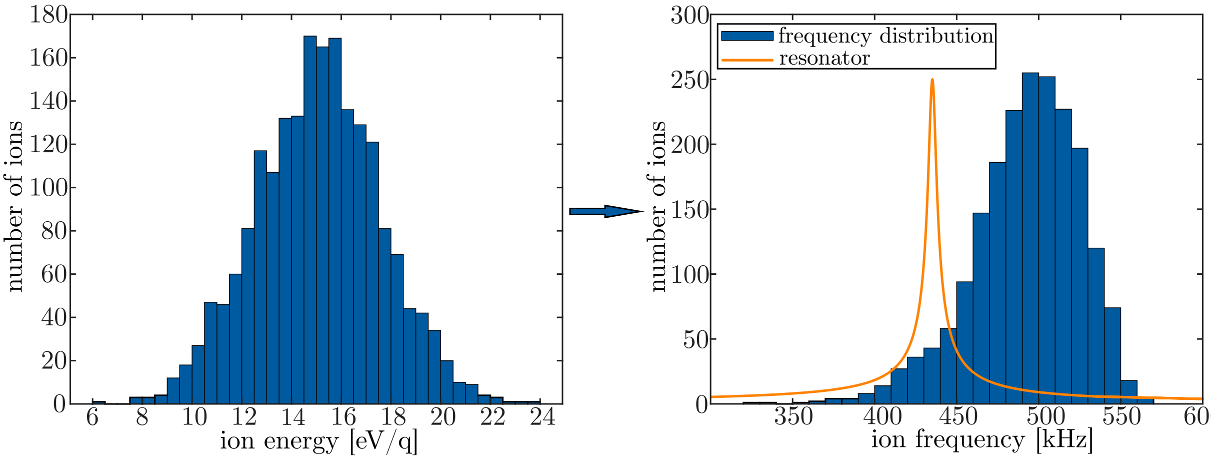

Figure 7.10.: Initial ion parameters for the calculation of the active-feedback cooling. The energy spread of the ions in the left picture is translated into a frequency distribution depicted on the right hand side. The orange curve depicts the characteristic curve of a resonator with a quality Q=100.

The ions under investigation here are 2000 C^{5+} ions. They are assumed to have an initial kinetic-energy distribution with a mean energy of 15 eV/q and a standard deviation of 2.5 eV/q. Figure 7.10 shows the initial energy distribution and the corresponding axial frequencies. The frequency spread initially is roughly 200 kHz which is $8 \cdot \beta$ and hence all ions cannot be covered by the resonator at once. The initial position is distributed uniformly along the z-axis in the intervall of [-2 mm,+2 mm] and all ions are moving in the +z - direction, assuming a slightly stretched bunch of ions. The capture potential U_0 is 35 V, because this voltage was found to have the best ion capture results, and the amplification factor k is 10^{-4}. The frequencies of the ions are between 400 kHz and 550 kHz and the frequency of the feedback signal is twice the ion oscillation frequency. That is why I set the crosstalk factor $\chi = 0.005$, according to figure 7.9. For comparision I also calculated the cooling efficiency for $\chi = 5 \cdot 10^{-4}$, and $\chi = 0$ for no crosstalk.

Simulation results

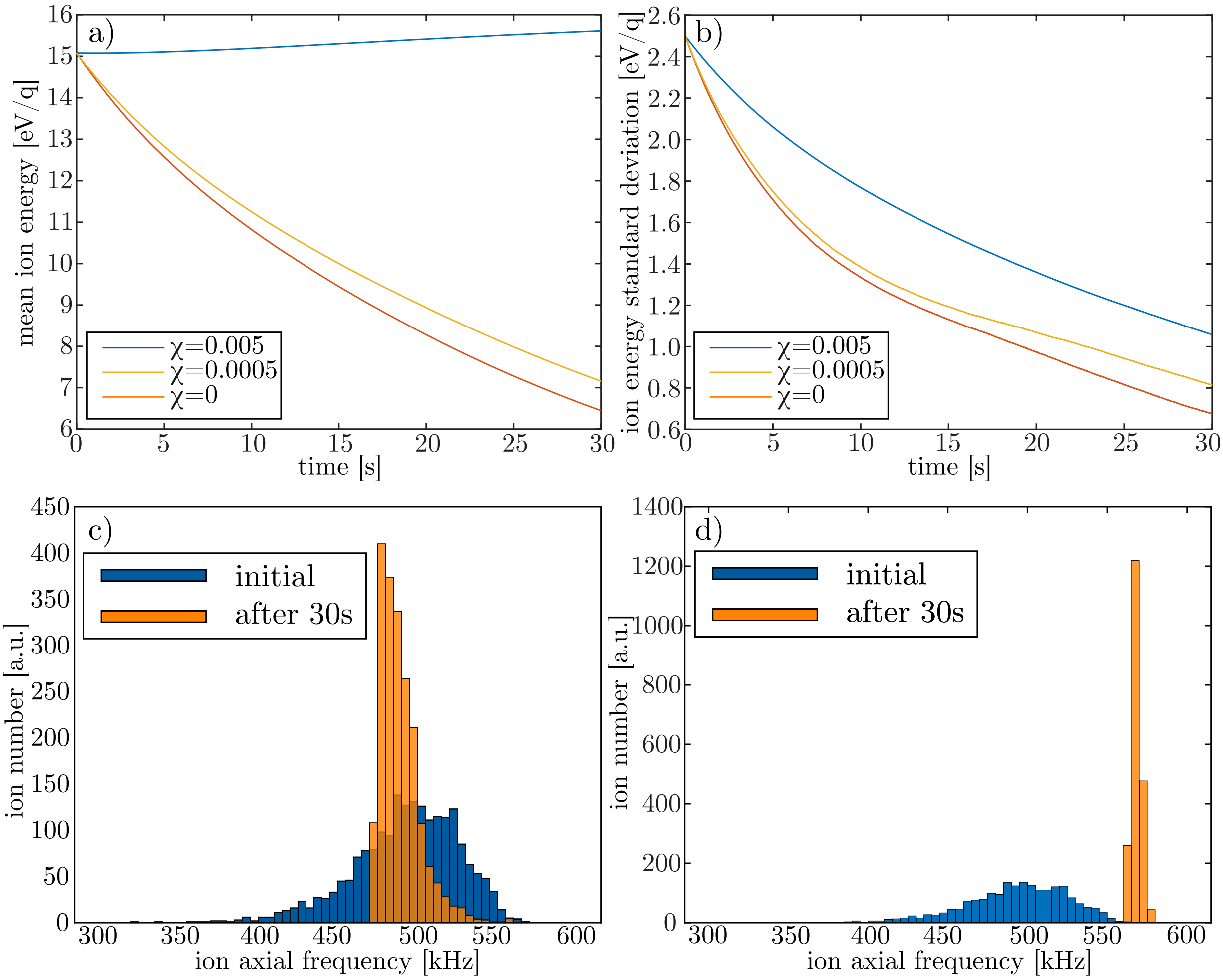

Figure 7.11.: The effect of active-feedback cooling. a) Evolution of the mean energy, b) evolution of the standard deviation of the ions' energy. Distribution of the axial ion frequency with a crosstalk of c) $\chi = 0.005$ and d) $\chi = 0$.

Figure 7.11a shows the evolution of the mean energy of the ions. For no crosstalk ($\chi = 0$), the mean kinetic energy decreases from initial 75 eV (15 eV/q) down to rougly 32 eV within 30 s. In contrast, for the crosstalk of the current electronics the calculation predicts the energy to be increased even slightly within the 30 s. Although this seems to be not satisfactory, a decent look at the axial frequencies of the stored ions in figure 7.11d shows that the frequency spread of the ions is reduced by a factor of two. Also the standard deviation of the axial energy is reduced by a factor of two. For sure, this effect is even stronger with no crosstalk, but this significant reduction of the frequency and energy spread is very promising for subsequent application of resistive cooling even with the current performance.

Active-feedback cooling as a precooling mechanism

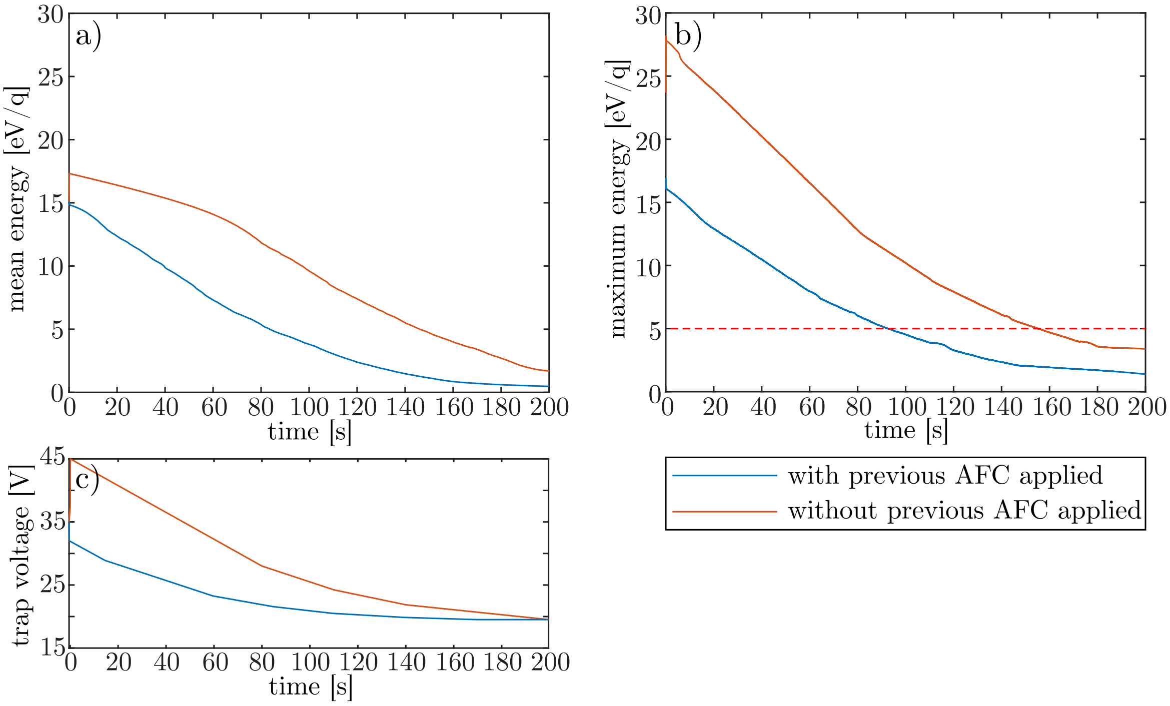

Figure 7.12.: Comparision of the energy evolution of precooled ions (blue curves) with not precooled ions (orange curves). a)Mean energy, b) energy of the ion with maximum energy. The red dashed line marks the energy, where all ions are in resonance with the resonator and c) the applied trap voltage.

To confirm the possible application of active-feedback cooling as precooling mechanism, I have simulated the energy evolution for ions which experienced active-feedback cooling before and compared the simulation results with ions which were not precooled. As initial conditions I have used in the case of precooled ions the state after 30 s active-feedback cooling with a crosstalk parameter $\chi = 0.005$ from the section before. In the case of no precooling I used the same initial conditions as for the active-feedback cooling shown in figure 7.10. For both calculations I have applied a decreasing voltage ramp to address all ions in the ensemble to be cooled. Refering to figure 7.11c precooled ions have a smaller energy and hence frequency spread. That is why, the voltage ramp of precooled ions starts at 32 V and for ions without precooling the voltage ramp starts at 45 V. The actual shape of the voltage ramp can be found in figure 7.12c.

The initial increase of the voltage in the case of no previous active-feedback cooling causes an increase of the mean ion energy as well as an increase of the maximum kinetic energy shown in figures 7.12a and 7.12b, respectively. So this case has a disadvantageous start. Although the energy loss is faster with these high energetic ions, in the precooled case (blue line) it takes about 90 s for all ions to have an energy of less than 5 eV/q, while in the not precooled case it takes about 150 s. When all ions have an energy below 5 eV/q, they are all inside the FWHM of the resonator and can be cooled simultaneously. In the precooled case the mean energy is below 1 eV/q after 3 min.

So, even under consideration of 30 s additional cooling time in the precooled case, the application of active-feedback cooling as precooling mechanism is useful for high-energetic ions but the final cooling to energies in the sub-meV regime is done with resistive cooling. In the calculated example, the predicted cooling time is of the order of minutes and hence the cycle time for laser experiments with well-prepared ion clouds is long. Compared with other steps, such as ion breeding and ion capture, the ion cooling is the most time consuming part. The calculation shows promising results for the wideband active-feedback cooling to reduce the cooling time significantly. To further decrease the cycle time, which would allow more laser-interaction events, the further decrease of the cooling time is necessary. Reducing for example the crosstalk by an order of magnitude would reduce the mean ion energy down to 7 eV/q within 30 s. Also the energy spread would be reduced faster. As the strength of ion-ion-interaction is much higher with low-energetic ions, it cannot be neglected anymore, when the ion energy is below 5 eV/q. Here, the experimental approach is more promising and will be be part of the next update of the HILITE Penning trap.

8. Conclusion and Outlook

The investigation of atomic ions with high-intensity laser light opens up the chance to infer inner-shell electron dynamics and gives access to novel research areas in the field of light-matter interaction. To be able to benchmark theories that describe the photo-ionisation of ions, the precise measurement of absolute cross sections is of fundamental importance. To this end, well-defined ion targets have to be prepared. This refers to ion-target composition (with single-species ion targets as a favourable option), to the ion-target localisation and shape, and to the ion number density.

In this thesis, the HILITE Penning trap setup has been presented. It is designed to dynamically capture ions from external sources such as electron-beam ion sources for the production of highly charged ions. The captured ions are stored inside the trap and have to be cooled down to energies in the meV regime. To determine the trap content before and after the ion-laser interaction, destructive and non-destructive measurement techniques have been applied. To achieve a compact ion cloud, the setup facilitates special compression techniques to be applied the cooled ions.

During the course of this thesis, the presented setup has been designed, built, and the commissioning has been performed up to a substantial degree. We have developed a deceleration and ion-capture sequence which allows dynamic capture and confinement of ion bunches produced in an external ion source. The absolute particle number within individual ion bunches, the ion kinetic energy, and the bunch length have been measured by use of a single-pass non-destructive charge counter that has been developed, built and characterised in detail. The ions can be decelerated to kinetic energies of less than 100 eV/q and axially compressed to bunch lengths of less than 50 mm. The minimum measurable number of Ar^{13+} ions has been found to be approximately 490 in the current single-pass configuration. The decelerated ions have been successfully captured and confined in the trap for storage times up to minutes. We have detected the stored ions destructively and non-destructively with an MCP detector and a resonant detection circuit, respectively.

From the time of flight of the ions ejected from the ion trap, we have deduced the ion composition inside the trap and its evolution over time. We have measured the decay time constant of the ion number. The determination of the absolute ion number needs a detailed investigation and calibration and will be performed in upcoming measurements.

From the evolution of the ion signal in absence of electronic cooling we have estimated the energy of the ions to be about 15 eV/q upon capture and to reduce within 15 min to about 1 eV/q. In this situation, the dominant cooling mechanism is buffer-gas cooling. From both the ion-number decay time constant and the cooling time constant, we have determined a residual gas pressure of about 2×10^{-10} mbar.
We have also detected the ions with the axial resonator and corroborated the initial ion energy to be about 15 eV/q. From the characterising measurements, we estimate to be able to detect a single ion with the axial resonant circuit if it has an axial energy of at least 1 eV/q. At the moment, a new generation of cryogenic axial amplifiers with reduced noise level and increased amplification is being developed and the non-destructive detection circuit will be equipped with such device in future in order to detect ions with lower energy. A very challenging issue is the ion cooling inside the Penning trap. To achieve a well-defined ion cloud, we need to reduce the ions' mean kinetic energy to the sub-meV regime. This will be achieved by resistive cooling and active-feedback cooling. I have investigated the prospective cooling efficiency of resistive cooling in the trap. I have found the axial frequency to be reduced by a factor of two with high energetic ions, mainly due to the comparably high trap anharmonicity. To reduce the initially high kinetic energy and hence frequency spread, I have investigated the use of a wide-band active-ion cooling technique in order to decrease the cooling time. Here, the signal is picked-up by an electrode, phase shifted, amplified, and fed back to the very same electrode. In order to reduce the crosstalk between pick-up signal and excitation signal I have designed, built and tested a special electronic circuit to filter the excitation signal keeping only the induced ion signal. At the moment, the extinction ratio is about -55dB (1:562). I have performed simulations which have shown a significant reduction of the frequency spread allowing shorter resistive cooling times. A reduction of the crosstalk increases the pre-cool efficiency even further and will be improved in future.
Knowledge of the momentum of electrons emitted during laser ionisation allows a profound study of the ionisation process regarding effects like above-threshold ionisation or non-sequential double ionisation which would be new with initially charged target ions and high-intensity and / or high photon-energy lasers. To this end, we will equip the trap with a temporally and spatially sensitive micro-channel plate and deduce the electron momentum from the time of flight and the point of electron impact in future.

A. Appendix

A.1. Magnetic stray field

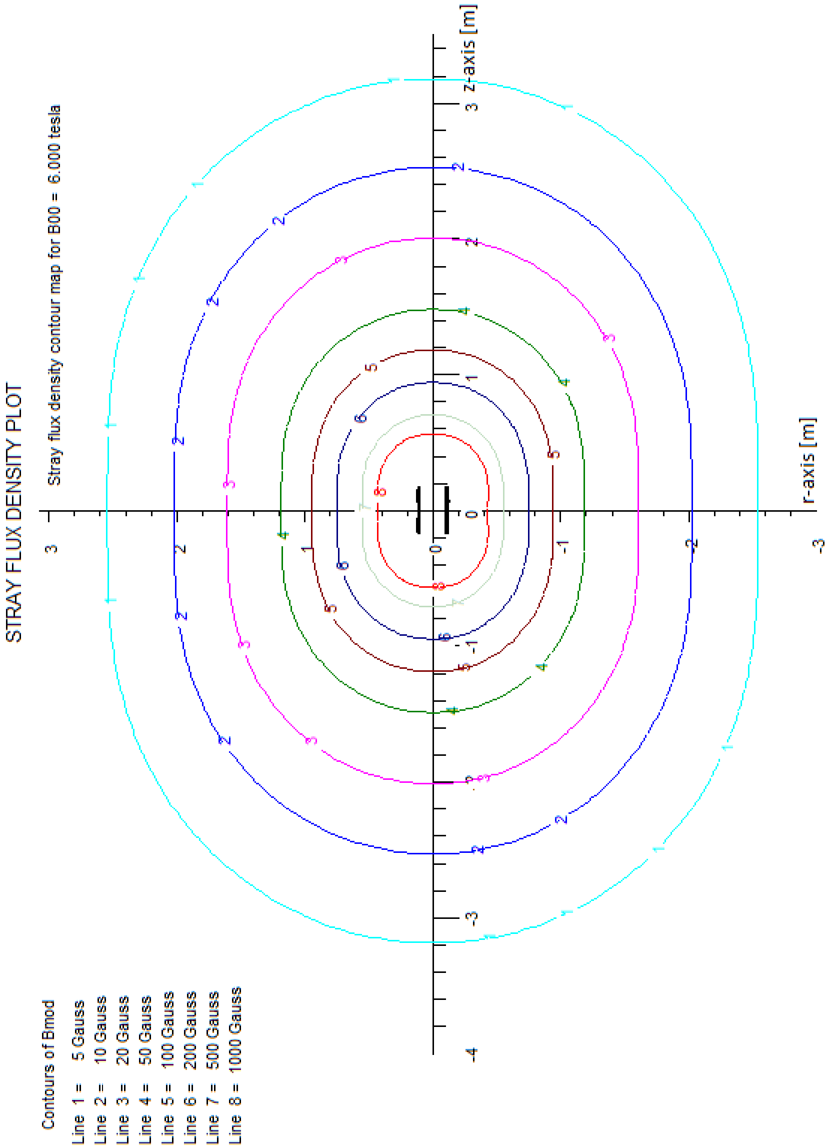

Figure A.1.: The magnetic stray field of the HILITE magnet supported by the constructor OXFORD industries.

A.2. Wiring diagrams of the trap

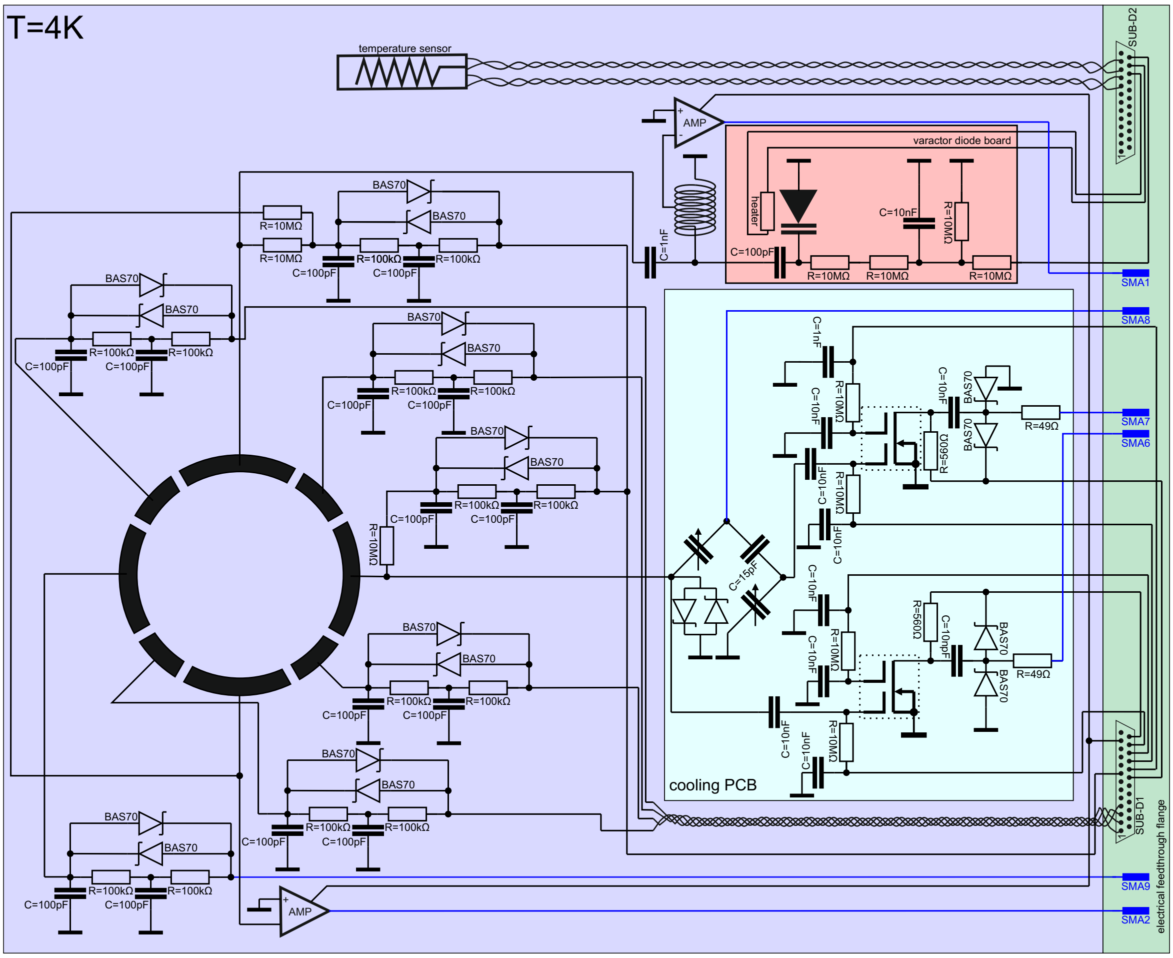

Figure A.2.: Wiring of the ring electrode and the applied detection systems. Here, the blue wires are coaxial cables.

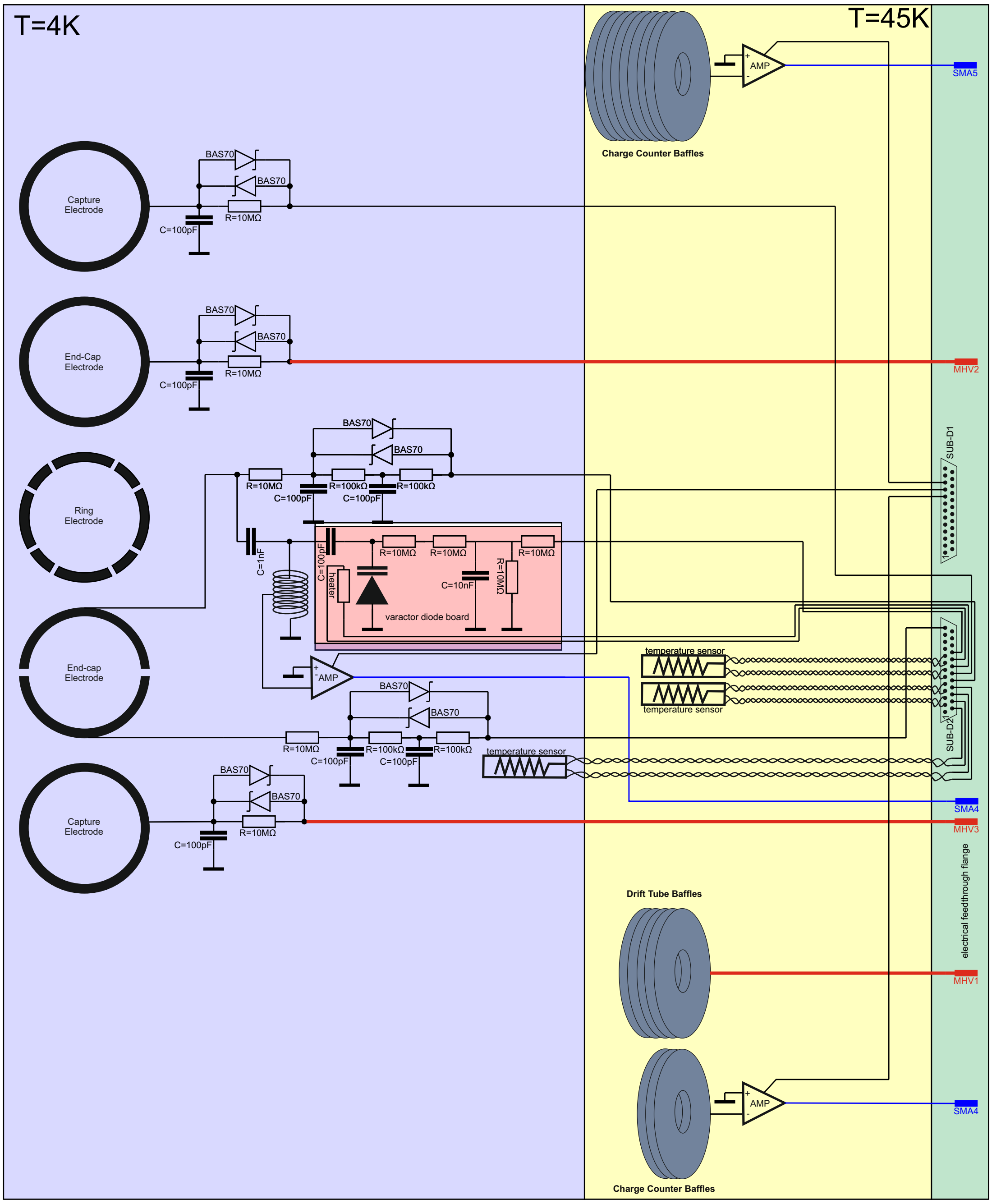

Figure A.3.: Wiring of all electrodes and detection systems except ring-electrode segment. Here, the blue wires are coaxial cables. The red ones are pure copper-cables with low resistance to enable fast switching of the respective electrodes.

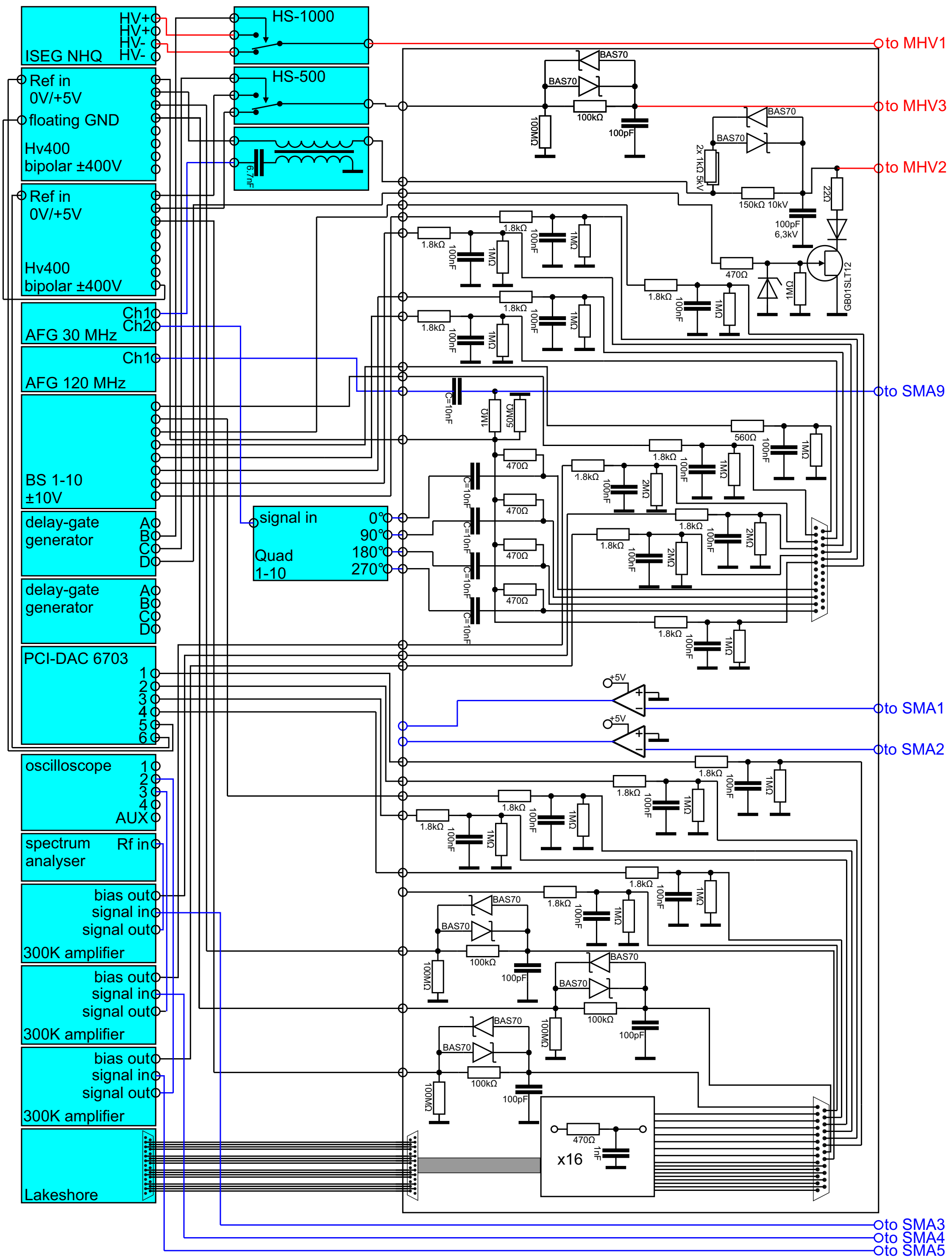

Figure A.4.: Wiring inside the room-temperature filter box and the connection of the external devices.

A.3. Reaction rate coefficients

Table A.1.: Typical reaction paths of singly charged ions with neutral particles at low kinetic energies.

reaction	rate constant [$\mathrm{cm^3\,s^{-1}}$]	reference
$C^+ + H_2O \longrightarrow CHO^+ + H$	2.5×10^{-9}	[83]
$C^+ + O_2 \longrightarrow CO^+ + O$	1.22×10^{-9}	[84]
$C^+ + CO_2 \longrightarrow CO^+ + CO$	1.1×10^{-9}	[84]
$CO^+ + H_2 \longrightarrow CHO^+ + H$	1.8×10^{-9}	[83]
${H_2}^+ + H_2 \longrightarrow {H_3}^+ + H$	2.9×10^{-9}	[85]
${H_3}^+ + NO \longrightarrow HNO^+ + H_2$	1.4×10^{-9}	[83]
${H_3}^+ + H_{20} \longrightarrow H_3O^+ + H_2$	4.3×10^{-9}	[83]
$O^+ + N_2 \longrightarrow NO^+ + N$	1.2×10^{-12}	[83]
$N^+ + O_2 \longrightarrow NO^+ + O$	6.1×10^{-10}	[83]
$H_2O^+ + H_2 \longrightarrow H_3O^+ + H$	1.4×10^{-9}	[83]

Background-free measurement of multi-photon absorption and transition-isolated excitations in simple ionic systems

G. Brenner[1], S. Ringleb[3], N. Stallkamp[2,3], S. Duesterer[1], M. Ruiz-Lopez[1], J.Hofbrucker[2,3,4], M. Kiffer[3], G.G. Paulus[3,4], Th. Stöhlker[2,3,4], K. Tiedtke[1], M. Vogel[2], and A. Volotka[2,4]

[1] Deutsches Elektronen-Synchrotron DESY, 22607 Hamburg, Germany
[2] GSI Helmholtzzentrum für Schwerionenforschung, 64291 Darmstadt, Germany
[3] Friedrich-Schiller-Universität Jena, 07743 Jena, Germany
[4] Helmholtz-Institut Jena, 07743 Jena, Germany

We intend to prepare and use a well-defined single-species ion cloud of hydrogen-like carbon (C^{5+}) inside a Penning trap setup to perform background-free measurements of ionisation cross sections as a function of photon energies and laser intensities.

State of research and purpose of the experiment

Using free-electron lasers (FELs), nonlinear processes have been investigated mainly in neutral atoms, e.g. the two-photon ionisation of the K-shell electron in Ge, Cu, and Zr atoms [K. Tamasaku et al., Nat. Photon. **8**, 313 (2014); J. Szlachetko et al., Sci. Rep. **6**, 33292 (2016); S. Ghimire et al., Phys. Rev. A **94**, 043418 (2016)] or two-photon absorption in Ge and Cu atoms [K. Tamasaku et al., Nat. Photon. **8**, 313 (2014); K. Tamasaku et al., PRL **121**, 083901 (2018)]. However, the experimental investigation of non-linear processes with neutral atoms is connected with the problems of sample damage and strong-background effects due to one-photon processes with outer electrons. Therefore, it would be of crucial importance to investigate the nonlinear processes with ions. So far, however, there is only one experiment measured the two-photon ionization of Ne^{8+} ions [G. Doumy et al., PRL **106**, 083002 (2011)], the result of which disagrees with theory by several orders of magnitude.

Non-linear multi-photon processes have wildly whirled in the light-matter interaction domain since the invention of the optical laser, and with time's passage they have brought us to a wide range of basic research fields as well as applied technologies. The most prominent technology there is high-harmonic generation (HHG). However, until recently, all studies and applications were connected with non-linear processes from microwave to ultraviolet frequencies. In this case the typical laser intensities of the order of 10^{13} to 10^{15} W/cm^2 correspond to a strong-field regime and the electron dynamics is mainly described by the laser field. With recent developments of free-electron laser sources [W. Ackermann et al., Nature Photonics **1**, 336 (2007), P. Emma et al., Nature Photon. **4**, 641 (2010); T. Ishikawa et al., Nature Photon. **6**, 540 (2012)] the study of non-linear processes in atoms and molecules at extreme ultraviolet and x-ray energies becomes feasible [C. Pellegrini et al., Rev. Mod. Phys. **88**, 015006 (2016)]. From the experimental point of view this will allow us to push the frontier of non-linear optics further into the soft- and hard X-ray region, and, in terms of theory, one enters the regime where electron dynamics is significantly influenced by the atomic field or both atomic as well as laser fields have to be equally accounted for. Here, however, the required theoretical description is not well understood, see e.g. the multi-photon multiple ionization of Xe [A. A. Sorokin et al., Phys. Rev. Lett. **99**, 213002 (2007)].

At this point, we want to investigate the non-linear light-matter interaction processes employing X-ray laser pulses and simple atomic systems, i.e. hydrogen-like ions such as C^{5+}. We plan to measure directly the two-photon absorption or three-photon absorption as a function of the photon energy. In view of the simple system to be used and the clear experimental conditions, our results can be used for a benchmarking of the theory of non-linear interactions in X-ray regime as well as to push further the non-linear spectroscopy at X-ray wavelengths.

To provide a pure single-species ion target, we have designed and built a **Penning trap** setup [M. Vogel et al., NIMB **285**, 65 (2012); S. Ringleb et al., Phys. Scr. T **166**, 014067 (2015)], which allows the localisation, cooling and positioning of a well-defined ion target. This Penning trap is **transportable** and designed to be connected to different laser systems. The trap is equipped with an electron-beam ion source (EBIT) which delivers highly charged ions for storage in the trap.

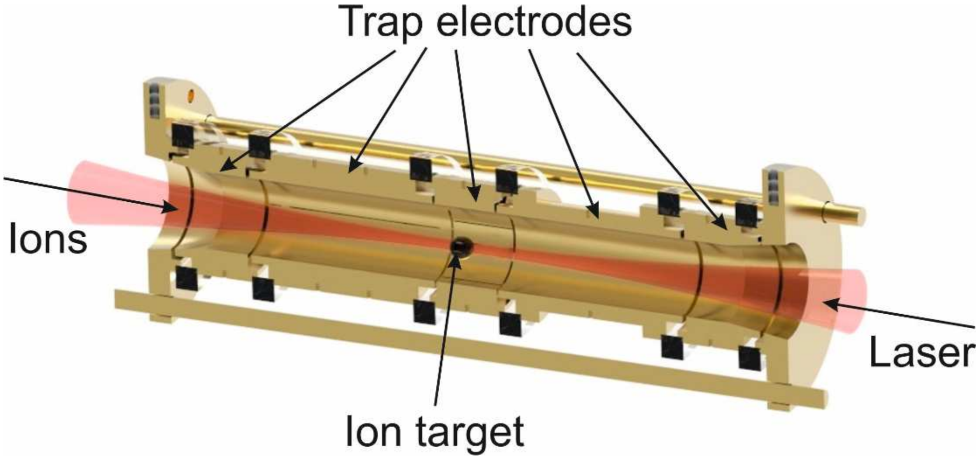

Figure 1: Schematic cut-out of the Penning trap with the ion target stored in the centre and laser light entering from the right.

In the frame of the present proposal, we will pursue two objectives. The first will be to evaluate the general feasibility of laser-ionisation of trapped ions with subsequent detection and further storage of the reaction products. The second is the above-motivated measurement of the energy-dependence of **laser-ionisation cross-sections of highly charged ions**. We want to comprehend predicted resonances and to investigate the question if the theory of TPA still holds true for strongly bound valence electrons. Therefore, we intend to measure also **absolute ionisation cross-sections**.

The Instrument

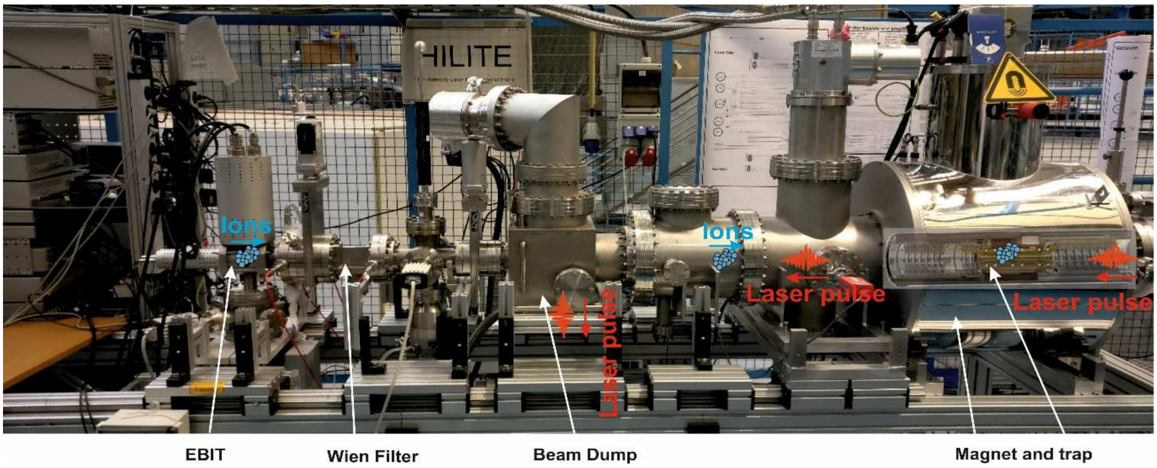

Figure 2: Experimental setup consisting of: EBIT ion source, Wien filter, beam dump, main chamber and magnet with trap (here shown as superimposed CAD-drawing). The setup has an overall length of about 3 meters, can be split up into three parts and is transportable.

The ion source in use (a commercial Dresden EBIT) can produce bunches of highly charged ions up to Xe^{46+}, in this case with a repetition rate of 0.2Hz and 100 ions per bunch. For lighter species such as hydrogen-like carbon (C^{5+}), the number of produced ions goes up to 10^6 at a repetition rate of 5Hz. The extracted ions will be captured dynamically and stored inside the trap. To characterise the reaction educts, we can apply the non-destructive FT-ICR (Fourier-Transfer Ion-Cyclotron Resonance) technique. Single-species ion clouds are facilitated by use of the Wien filter of the ions source, and contaminant ions can be resonantly ejected from the trap by the so-called SWIFT (Stored-Waveform Inverse Fourier Transform) technique [A. Marshall et al., Mass Spectrm. Rev. **17**, 1 (1998)]. To achieve high particle densities, the ions are cooled via resistive cooling. Additionally, the ion cloud can be compressed and shaped by application of the so-called rotating-wall technique [S. Bharadia et al., Appl. Phys. B **107**, 1105 (2012)]. It can further be positioned along the laser propagation axis by about 1 mm with a precision of a few microns. This allows the optimisation of the overlap between laser focus and ion target. The reaction products can be detected non-destructively inside the trap with a precision down to ten particles or destructively even down to a single particle.

K-Shell ionisation of C^{5+}

Hydrogen-like carbon is an easy-to-describe ionic system in theory. Therefore, it is an ideal subject of interest and to compare experimental results with theoretical predictions. The binding energies are still moderate to ionise the K-shell electron with two X-ray photons to achieve pure two-photon absorption. Besides, it can be produced easily with our EBIT and can be compressed to high particle densities, to achieve a count rate beyond ten interactions per second at intensities of 10^{16} W/cm². This high count rate will allow us to probe our target at numerous photon energies and will let us to investigate:

- Two-photon non-sequential ionisation (a)
- Three-photon non-sequential ionisation (b)
- Two-photon 1s-2s excitation with subsequent ionisation (c)
- Interaction probability with photon-energies around the threshold between two regimes
- Photon-energy calibration of the laser in respect to central frequency and energy distribution

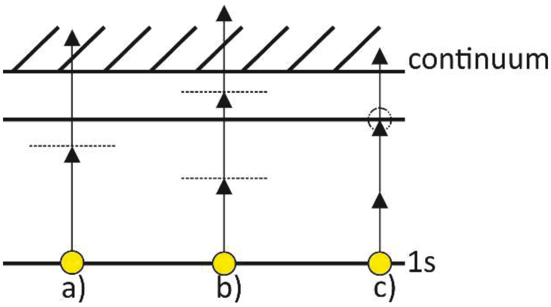

Figure 3: Multi-photon ionisation mechanisms. a) non-sequential two-photon ionisation, b) non-sequential three-photon ionisation, c) non-sequential two-photon excitation with subsequent ionisation (three-photon process).

For photon energies between 248 eV and 300 eV the two-photon non-sequential (both photons are absorbed “at once”) ionization is the dominant process. In the region below 248 eV, absorption of at least three photons is needed to free the electron. Here, extremely prominent resonances can be found, where a certain inner-atomic transition is addressed resulting in a strong increase of the ionisation probability. In particular, at an energy of 183.7 eV we expect to measure two-photon excitation from 1s to 2s with subsequent ionisation by a third photon.

As the transition energies and their respective line widths of hydrogen-like systems are well-predictable by theory, the resonances can be used as a gauge for the spectral distribution of the exciting laser. Measurements and comparing theory of Ne^{9+}-production found a large dependence of the ion yield assuming different spectral shapes of the laser-pulses. The usage of C^{5+}-ions will give us the opportunity to reverse-engineer the spectral properties of the laser. This information can be used for further investigations of energy-dependent ionisation cross-sections.

The ion cloud as laser target

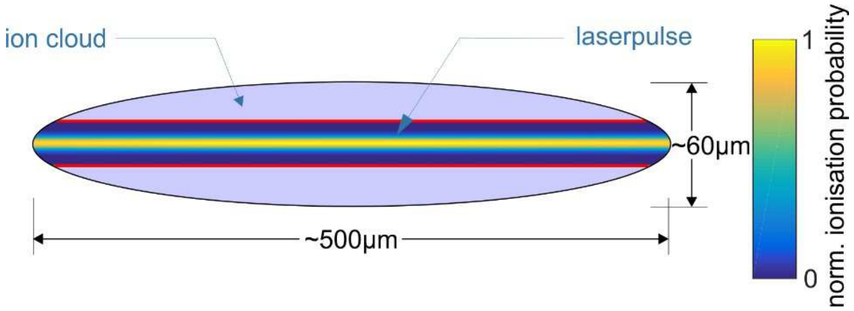

Figure 4: Ionisation probability distribution inside an ion cloud irradiated by a focused laser beam. The measures of the cloud are typical for 1000 low-mass ions at a magnetic field strength of 2.5 T. The ion density will be typically of the order of 10^5 mm^{-3}. Here, a Gaussian-shaped laser beam is assumed.

To achieve a measurement of absolute cross-sections of laser ionisation, one needs to know the laser-focus geometry and the target properties well. Our instrument uses the so-called rotating wall technique, which allows knowledge of the ion density and shape of the ion cloud. An ion cloud of 1000 C^{5+} will assume a spheroidal shape with a length of about 0.5 mm and a diameter of about 60 µm. The laser focus will be inside the ion cloud and will irradiate several hundreds of ions at once, where a certain fraction will be ionised, depending on the cross section. In our case, we benefit from a laser focus with a large Rayleigh length, as the focal diameter inside the ion cloud and therefore the intensity distribution will be very homogeneous.

Prospected ion yield

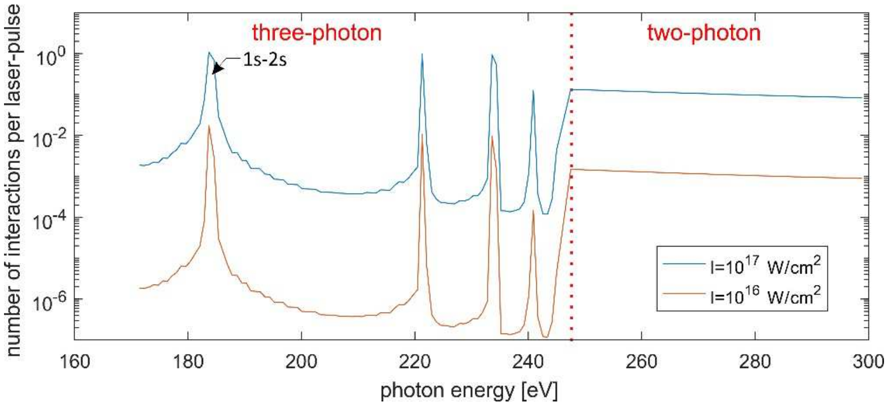

Figure 5: Photon energy dependence of the number of interactions expected for a C^{5+} ion-cloud. For two photon ionisation we expect 10 interaction per second assuming 1000 laser-pulses a second.

As the cross section and therefore the number of interactions per laser-pulse will vary much with photon energy and laser intensity, there are two possible scenarios:

1. For high ion yield per laser shot, a large amount of our educts are ionised and we have to clean the trap after a few shots and setting up another ion cloud, which limits us to about 100 C^{6+} ions per minute.
2. For low ion yield per laser shot, we can store the ion cloud for several minutes and irradiate it persistently with a high repetition rate at constant laser parameters **without changing the properties of our ion target**. Here, we expect to have also up to 100 C^{6+} ions a minute but even down to a single event a minute or less.

For low-intensity experiments a suitable candidate could be lithium-like oxygen (O^{5+}). At intensities from 10^{14} W/cm² to 10^{15} W/cm² only the L-electron is addressed by the laser. So, we also have a single active electron process here. We expect good ion-yields for photon energies between 50 eV and 120 eV even at moderate intensities as shown in figure 6. The two described scenarios as described above are still valid here.

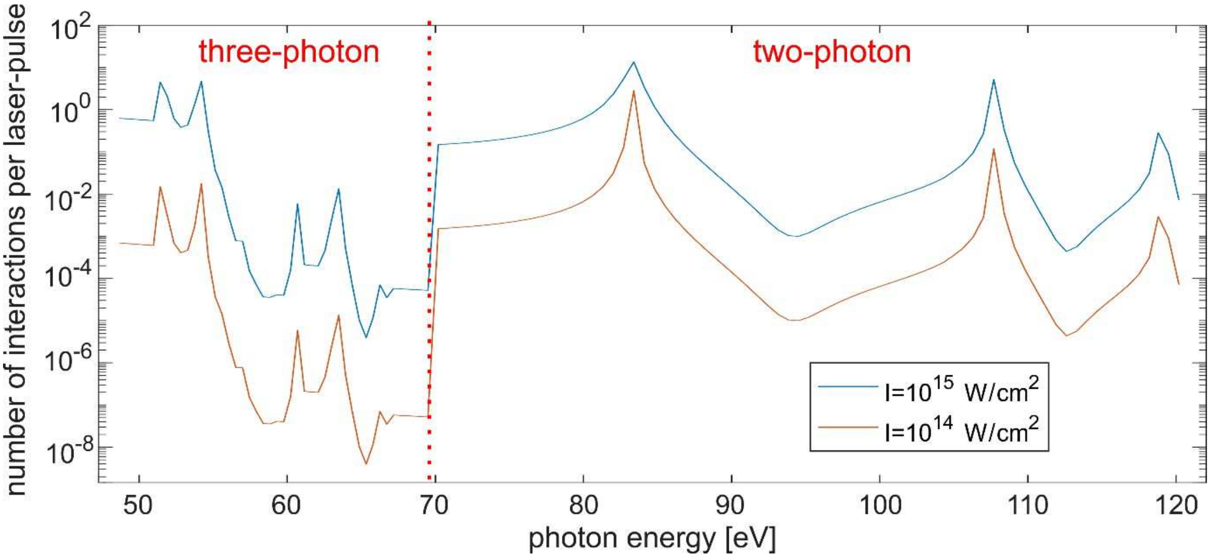

Infrastructural and beam time requirements

The overall infrastructure needed for the setup consist of two high-power connectors (3-phase 400V) and two cooling water lines for the cryo-compressors. In addition, an area of 2x2m around the magnet should stay free due to the magnetic stray field. Our instrument demands ultra-high vacuum with a pressure better than 10^{-9} mbar.

We apply for photon energies between 180 eV and 280 eV with the maximum number of photon bunches that FLASH can deliver, i.e. 500 pulses/macrobunch (5000 pulses/s), with a repetition rate of 1MHz. In order to achieve the high laser intensities we will need a focused beam to a beam-diameter of less than 5 µm FWHM. These requirements make beamline FL24 at FLASH2 with its micro-focus capabilities and the energy scanning option the perfect beamline for the envisioned studies.

We apply for 144 hours (12 shifts) of beamtime within two weeks. In the first 3 days we need any photon energy between 260 and 300 eV with highest possible intensity for adjustment and instrument tests.

Following this, we want to scan the photon energies between 180 eV and 280 eV. In the region of the peaks the step size should be about 0.5eV. Between 250 eV and 280 eV we will need only a step size of 10 eV. For the energies with high count rate, we want to vary the laser-intensity between 10^{15} and 10^{17} W/cm².

Alternatively, we can also perform experiments with laser-intensities between 10^{14} and 10^{15} W/cm² with other ion-targets (e.g. O^{5+} as discussed above). Here, the used photon energies will be between 50 eV and 120 eV.

Bibliography

[1] M. Planck. Über irreversible Strahlungsvorgänge. *Annalen der Physik*, 306(1):69–122, 1900.

[2] A. Einstein. Über einen die Erzeugung und Verwandlung des Lichtes betreffenden heuristischen Gesichtspunkt. *Annalen der Physik*, 322(6):132–148, 1 1905.

[3] M. Göppert-Mayer. Über Elementarakte mit zwei Quantensprüngen. *Annalen der Physik*, 401(3):273–294, 1 1931.

[4] T. H. Maiman. Stimulated Optical Radiation in Ruby. *Nature*, 187:493 – 494, 1960.

[5] W. Kaiser and C. G. B. Garrett. Two-Photon Excitation in CaF_2: Eu^{2+}. *Phys. Rev. Lett.*, 7:229–231, 1961.

[6] J. M. J. Madey. Stimulated Emission of Bremsstrahlung in a Periodic Magnetic Field. *Journal of Applied Physics*, 42(5):1906–1913, 1971.

[7] D. Strickland and G. Mourou. Compression of amplified chirped optical pulses. *Optics Communications*, 55(6):447 – 449, 1985.

[8] S. Augst, D. D. Meyerhofer, D. Strickland, and S. L. Chin. Laser ionization of noble gases by Coulomb-barrier suppression. *J. Opt. Soc. Am. B*, 8(4):858–867, 1991.

[9] K. Yamakawa, Y. Akahane, Y. Fukuda, M. Aoyama, N. Inoue, H. Ueda, and T. Utsumi. Many-Electron Dynamics of a Xe Atom in Strong and Superstrong Laser Fields. *Phys. Rev. Lett.*, 92(12):123001, 2004.

[10] M.V. Ammosov, N.B. Delone, and V.P. Krainov. Tunnel ionization of complex atoms and of atomic ions in an alternating electromagnetic field. *Sov. Phys. JETP*, 64:1191–1194, 1986.

[11] E. A. Chowdhury, C. P. J. Barty, and B. C. Walker. “Nonrelativistic” ionization of the L-shell states in argon by a “relativistic” $10^{19}\mathrm{W/cm^2}$ laser field. *Phys. Rev. A*, 63:042712, 2001.

[12] G. G. Paulus, W. Nicklich, H. Xu, P. Lambropoulos, and H. Walther. Plateau in above threshold ionization spectra. *Phys. Rev. Lett.*, 72(18):2851–2854, 1994.

[13] S. Larochelle, A. Talebpour, and S. L. Chin. Non-sequential multiple ionization of rare gas atoms in a Ti:Sapphire laser field. *J. Phys. B: At. Mol. Opt. Phys.*, 31(6):1201, 1998.

[14] Th. Weber, et al. Sequential and nonsequential contributions to double ionization in strong laser fields. *J. Phys. B: At. Mol. Opt. Phys.*, 33(4):L127, 2000.

[15] M. Kurka, et al. Differential cross sections for non-sequential double ionization of He by 52 eV photons from the Free Electron Laser in Hamburg, FLASH. *New J. Phys.*, 12(7):073035, 2010.

[16] A. L'Huillier and Ph. Balcou. High-order harmonic generation in rare gases with a 1-ps 1053-nm laser. *Phys. Rev. Lett.*, 70:774–777, 1993.

[17] S. Palaniyappan, A. DiChiara, E. Chowdhury, A. Falkowski, G. Ongadi, E. L. Huskins, and B. C. Walker. Ultrastrong Field Ionization of Ne^{n+} $(n \leq 8)$: Rescattering and the Role of the Magnetic Field. *Phys. Rev. Lett.*, 94(24):243003, 2005.

[18] S. Palaniyappan, A. DiChiara, I. Ghebregziabher, E. L. Huskins, A. Falkowski, D. Pajerowski, and B. C. Walker. Multielectron ultrastrong laser field ionization of Ar^{n+}, Kr^{m+} and Xe^{l+} ($n \leq 9$, $m \leq 9$, $l \leq 12$) at intensities from 10 ^{15} W cm $^{-2}$ to 10 ^{18} W cm $^{-2}$. *Journal of Physics B: Atomic, Molecular and Optical Physics*, 39(13):357–369, 2006.

[19] M. Vogel, W. Quint, G. G. Paulus, and Th. Stöhlker. A Penning trap for advanced studies with particles in extreme laser fields. *Nuclear Instruments and Methods in Physics Research Section B: Beam Interactions with Materials and Atoms*, 285:65–71, 2012.

[20] G. Doumy, et al. Nonlinear Atomic Response to Intense Ultrashort X Rays. *Phys. Rev. Lett.*, 106:083002, 2011.

[21] B. Faatz, et al. Flash II: Perspectives and challenges. *Nuclear Instruments and Methods in Physics Research Section A: Accelerators, Spectrometers, Detectors and Associated Equipment*, 635(1, Supplement):2–5, 2011.

[22] J. Feldhaus, M. Krikunova, M. Meyer, Th. Möller, R. Moshammer, A. Rudenko, Th. Tschentscher, and J. Ullrich. AMO science at the FLASH and European XFEL free-electron laser facilities. *Journal of Physics B: Atomic, Molecular and Optical Physics*, 46(16):164002, 2013.

[23] M. Hornung, et al. 54 J pulses with 18 nm bandwidth from a diode-pumped chirped-pulse amplification laser system. *Opt. Lett.*, 41(22):5413–5416, 2016.

[24] V. Bagnoud, et al. Commissioning and early experiments of the PHELIX facility. *Appl. Phys. B*, 100(1):137–150, 2010.

[25] A. Sävert, G. Schäfer, B. Beleites, F. Ronneberger, M.C. Kaluza, M. Zepf, V. Bagnoud, and T. Stöhlker. Current status of the JETi 200 laser system. In *Helmholtz Institute Jena - Annual report*, 2014.

[26] V. Ayvazyan, et al. First operation of a free-electron laser generating GW power radiation at 32 nm wavelength. *The European Physical Journal D - Atomic, Molecular, Optical and Plasma Physics*, 37(2):297–303, 2006.

[27] Charles J. Joachain. *Atoms in intense laser fields.* Cambridge Univ. Press, Cambridge u.a., 2012.

[28] W. Becker, F. Grasbon, R. Kopold, D. B. Milošević, G. G. Paulus, and H. Walther. Above-threshold ionization: From classical features to quantum effects. In B Bederson, H. Walther, B Bederson, and H. Walther *Advances In Atomic, Molecular, and Optical Physics*, volume 48, pages 35–98. Academic Press Inc., San Diego, 2002.

[29] L.W. Keldysh. Ionisation in the field of a strong electromagnetic wave. *Soviet Physics JETP*, 20(5):1307–1314, 1965.

[30] L. S. Brown and G. Gabrielse. Geonium theory: Physics of a single electron or ion in a Penning trap. *Reviews of Modern Physics*, 58(1):233–311, 1986.

[31] Sven Sturm. *The g-factor of the electron bound in 28 Si 13+: The most stringent test of bound-state quantum electrodynamics.* PhD thesis, Johannes Gutenberg-Universität Mainz, 2011.

[32] V. Gomer, H. Strauss, and D. Meschede. A compact Penning trap for light ions. *Applied Physics B*, 60(2):89–94, 1995.

[33] G. Gabrielse and F. C. Mackintosh. Cylindrical Penning traps with orthogonalized anharmonicity compensation. *International Journal of Mass Spectrometry and Ion Processes*, 57(1):1–17, April 1984.

[34] G. Gabrielse, L. Haarsma, and S. L. Rolston. Open-endcap Penning traps for high precision experiments. *International Journal of Mass Spectrometry and Ion Processes*, 88(2–3):319–332, 1989.

[35] G. Gabrielse. Relaxation calculation of the electrostatic properties of compensated Penning traps with hyperbolic electrodes. *Phys. Rev. A*, 27(5):2277–2290, 1983.

[36] Manuel Vogel. *Particle Confinement in Penning Traps.* Springer International Publishing, Switzerland, 2018.

[37] L. Schweikhard and A. G. Marshall. Excitation modes for fourier transform-ion cyclotron resonance mass spectrometry. *J. Am. Soc. Mass. Spectrom*, 4(6):433–452, 1993.

[38] S. Guan and A. G. Marshall. Stored waveform inverse Fourier transform axial excitation/ejection for quadrupole ion trap mass spectrometry. *Anal. Chem.*, 65(9):1288–1294, 1993.

[39] J. B. Jeffries, S. E. Barlow, and G. H. Dunn. Theory of space-charge shift of ion cyclotron resonance frequencies. *International Journal of Mass Spectrometry and Ion Processes*, 54(1–2):169–187, 1983.

[40] Alexander Piel. *Plasma Physics : An Introduction to Laboratory, Space, and Fusion Plasmas.* Graduate Texts in Physics. Springer, Cham, second edition, 2017.

[41] J. H. Malmberg and T. M. O'Neil. Pure Electron Plasma, Liquid, and Crystal. *Phys. Rev. Lett.*, 39:1333–1336, 1977.

[42] Ch. Kittel. *Introduction to solid state physics.* Wiley, Hoboken, NJ, 8. edition, 2005.

[43] S. Bharadia, M. Vogel, D. M. Segal, and R. C. Thompson. Dynamics of laser-cooled Ca+ ions in a Penning trap with a rotating wall. *Appl. Phys. B*, 107(4):1105–1115, 2012.

[44] J. J. Bollinger, D. J. Heinzen, F. L. Moore, Wayne M. Itano, D. J. Wineland, and Daniel H. E. Dubin. Electrostatic modes of ion-trap plasmas. *Phys. Rev. A*, 48(1):525–545, 1993.

[45] Ilja N. Bronštejn, editor. *Taschenbuch der Mathematik.* Deutsch, Thun u.a., 5., überarb. und erw. aufl. edition, 2000.

[46] A. G. Marshall, Christopher L. Hendrickson, and G. S. Jackson. Fourier transform ion cyclotron resonance mass spectrometry: A primer. *Mass Spectrom. Rev.*, 17(1):1–35, 1998.

[47] W. Shockley. Currents to Conductors Induced by a Moving Point Charge. *Journal of Applied Physics*, 9(10):635–636, 1938.

[48] X. Feng, M. Charlton, M. Holzscheiter, R. A. Lewis, and Y. Yamazaki. Tank circuit model applied to particles in a Penning trap. *Journal of Applied Physics*, 79(1):8–13, 1996.

[49] Wolfgang Nolting. *Grundkurs Theoretische Physik 3 : Elektrodynamik.* Springer-Lehrbuch. Springer-Verlag Berlin Heidelberg, Berlin, Heidelberg, 9., aktualisierte aufl. edition, 2011.

[50] Jochen Steinmann. *Modellierung und Simulation der Widerstandskühlung von hochgeladenen Ionen.* PhD thesis, Friedrich-Alexander-Universität Erlangen-Nürnberg, 2016.

[51] W. M. Itano, J. C. Bergquist, J. J. Bollinger, and D. J. Wineland. Cooling methods in ion traps. *Phys. Scr.*, 1995(T59):106, 1995.

[52] D. J. Wineland and H. G. Dehmelt. Principles of the stored ion calorimeter. *Journal of Applied Physics*, 46(2):919–930, 1975.

[53] M. Vogel, H. Häffner, K. Hermanspahn, S. Stahl, J. Steinmann, and W. Quint. Resistive and sympathetic cooling of highly-charged-ion clouds in a Penning trap. *Phys. Rev. A*, 90(4):043412, 2014.

[54] Stefan Stahl. *Aufbau eines Experimentes zur Bestimmung elektronischer g-Faktoren einzelner wasserstoffähnlicher Ionen.* PhD thesis, Johannes Gutenberg-Universität Mainz, 1998.

[55] F. Nolden, K. K Beckert, F. F Caspers, B. B Franczak, B. Franzke, R. Menges, A. Schwinn, and M. Steck. Stochastic cooling at the ESR. *Nuclear Instruments and Methods in Physics Research Section A: Accelerators, Spectrometers, Detectors and Associated Equipment*, 441(1):219 – 222, 2000.

[56] H. Dehmelt, W. Nagourney, and J. Sandberg. Self-excited mono-ion oscillator. *Proceedings of the National Academy of Sciences*, 83(16):5761–5763, 1986.

[57] B. D'Urso, B. Odom, and G. Gabrielse. Feedback Cooling of a One-Electron Oscillator. *Phys. Rev. Lett.*, 90:043001, 2003.

[58] Brian Richard d'Urso. *Cooling and Self-Excitation of a One-Electron Oscillator.* PhD thesis, Harvard University Cambridge, MA, 2001.

[59] N. Beverini, V. Lagomarsino, G. Manuzio, F. Scuri, G. Testera, and G. Torelli. Stochastic cooling in Penning traps. *Phys. Rev. A*, 38:107–114, 1988.

[60] L.A. Viehland and E.A. Mason. Transport Properties of Gaseous Ions over a Wide Energy Range, IV. *Atomic Data and Nuclear Data Tables*, 60(1):37 – 95, 1995.

[61] H.W. Ellis, M.G. Thackston, E.W. McDaniel, and E.A. Mason. Transport properties of gaseous ions over a wide energy range. Part III. *Atomic Data and Nuclear Data Tables*, 31(1):113 – 151, 1984.

[62] H.W. Ellis, R.Y. Pai, E.W. McDaniel, E.A. Mason, and L.A. Viehland. Transport properties of gaseous ions over a wide energy range. *Atomic Data and Nuclear Data Tables*, 17(3):177 – 210, 1976.

[63] A. Niehaus. A classical model for multiple-electron capture in slow collisions of highly charged ions with atoms. *J. Phys. B: At. Mol. Phys.*, 19(18):2925, 1986.

[64] Bahaa E. A. Saleh and Malvin C. Teich. *Fundamentals of photonics.* Wiley series in pure and applied optics. Wiley, New York u.a., 1991.

[65] P. A. Bélanger. Beam propagation and the ABCD ray matrices. *Opt. Lett.*, 16(4):196–198, 1991.

[66] R. Becker, O. Kester, and Th. Stöhlker. Simulation of charge breeding for trapped ions. *Journal of Physics: Conference Series* , 58:443–446, 2007.

[67] Béla Arndt. *Time-of-flight Measurements at HILITE.* Bachelor's thesis, Goethe Universität Frankfurt, 2018.

[68] M.A. Levine, R.E. Marrs, J.R. Henderson, D.A. Knapp, and M.B. Schneider. The Electron Beam Ion Trap: A New Instrument for Atomic Physics Measurements. *Physica Scripta*, T22:157–163, 1988.

[69] Wolfgang Demtröder. *Experimentalphysik 2 : Elektrizität und Optik.* Springer-Lehrbuch. Springer, Berlin, Heidelberg, 7., korrigierte und erweiterte auflage, 2017.

[70] S. Ringleb, M. Vogel, S. Kumar, W. Quint, G.G. Paulus, and Th. Stöhlker. HILITE – Ion Trap for Studies with Intense Laser Pulses. *Journal of Physics: Conference Series*, 635(9):092124, 2015.

[71] http://www.comsol.com.

[72] Ulrich Tietze. *Halbleiter-Schaltungstechnik.* Springer, Berlin ; Heidelberg u.a., 11., völlig neu bearb. und erw. aufl. edition, 1999. Literaturangaben.

[73] H. Schnatz, G. Bollen, P. Dabkiewicz, P. Egelhof, F. Kern, H. Kalinowsky, L. Schweikhard, H. Stolzenberg, and H.-J. Kluge. In-flight capture of ions into a penning trap. *Nuclear Instruments and Methods in Physics Research Section A: Accelerators, Spectrometers, Detectors and Associated Equipment*, 251(1):17 – 20, 1986.

[74] Markus Kiffer. *Selektive Breitbandanregung von Ionen in einer Penningfalle.* Bachelor's thesis, Friedrich-Schiller-Universität Jena, 2016.

[75] Markus Kiffer. *Non-destructive single-pass detection of highly charged ions.* Master's thesis, Friedrich-Schiller-Universität Jena, 2019.

[76] S. Schmidt, T. Murböck, Z. Andelkovic, G. Birkl, W. Nörtershäuser, S. Stahl, and M. Vogel. Non-destructive single-pass low-noise detection of ions in a beamline. *Review of Scientific Instruments*, 86(11):113302, 2015.

[77] M. Kiffer, S. Ringleb, N. Stallkamp, B. Arndt, I. Blinov, S. Kumar, S. Stahl, Th. Stöhlker, and M. Vogel. Single-pass non-destructive electronic detection of charged particles. *Review of Scientific Instruments*, 90(11):113301, 2019.

[78] https://webbook.nist.gov

[79] M. S. Ebrahimi, Z. Guo, M. Vogel, M. Wiesel, G. Birkl, and W. Quint. Resistive cooling of highly charged ions in a Penning trap to a fluidlike state. *Phys. Rev. A*, 98:023423, 2018.

[80] S. L. Rolston and G. Gabrielse. Cooling antiprotons in an ion trap. *Hyperfine Interact*, 44(1-4):233–245, 1988.

[81] Ekbert Hering, editor. *Elektronik für Ingenieure und Naturwissenschaftler*. Springer Vieweg, Berlin, 7., aktualisierte und verbesserte auflage, 2017.

[82] Hans Rudolf Schwarz. *Numerische Mathematik*. Vieweg+Teubner Verlag / Springer Fachmedien Wiesbaden GmbH, Wiesbaden, Wiesbaden, 8., aktualisierte auflage, 2011.

[83] D.L. Albritton. Ion-neutral reaction-rate constants measured in flow reactors through 1977. *Atomic Data and Nuclear Data Tables*, 22(1):1 – 89, 1978.

[84] V. G. Anicich, W. T. Huntress, and J. H. Futrell. Ion cyclotron resonance studies of some reactions of C^+ ions. *Chemical Physics Letters*, 40(2):233 – 236, 1976.

[85] H. Gutbier. Massenspektrometrische Untersuchung der Reaktion $X^+ + H_2 \longrightarrow HX^+ + H$. *Zeitschrift für Naturforschung A*, 12(6):499–507, 1957.

Ehrenwörtliche Erklärung

Ich erkläre hiermit ehrenwörtlich, dass ich die vorliegende Arbeit selbständig, ohne unzulässige Hilfe Dritter und ohne Benutzung anderer als der angegebenen Hilfmittel und Literatur angefertigt habe. Die aus anderen Quellen direkt oder indirekt übernommenen Daten und Konzepte sind unter Angabe der Quelle gekennzeichnet.
Die Arbeit wurde bisher weder im In- noch Ausland in gleicher oder ähnlicher Form einer anderen Prüfungsbehörde vorgelegt.
Die geltende Promotionsordnung der Physikalisch-Astronomischen Fakultät ist mit bekannt.
Ich versichere ehrenwörtlich, dass ich nach bestem Wissen die reine Wahrheit gesagt und nichts verschwiegen habe.

Jena, 05.12.2019 Unterschrift